**Effect of Random Noise and Gaussian Noise Forcing on the Wake of a Circular Cylinder**

by

Venkat Praveen Gambhir

A thesis submitted to the Graduate Faculty of
Auburn University
in partial fulfillment of the
requirements for the Degree of
Master of Science

Auburn, Alabama
May 10, 2015

Keywords: Circular Cylinder, Flow Control, Noise Forcing



Approved by

Anwar Ahmed, Chair, Professor of Aerospace Engineering
Brian S. Thurow, Associate Professor of Aerospace Engineering
Roy Hartfield, Walt and Virginia Woltosz Professor of Aerospace Engineering

Abstract

Flow over a bluff body has been a topic of extensive investigation, due to a variety of engineering problems such as vortex induced vibrations, unsteady forces and noise associated with the periodic flow in the wake. The effect of random and Gaussian noise forcing on the control and suppression of periodic von Kármán vortex shedding in the wake of a circular cylinder was investigated using internal acoustic excitation, at a Reynolds number of 12,000. The von Kármán vortices in the wake superimposed with the small strength vortices ejected from a slit due to forcing, resulted in acceleration of the shear layers, consequent delay in flow separation, shrinkage of the wake, and reduction in drag. Asymmetry in the wake was observed in cases involving single slit forcing, the effect of which was found maximum when the slit angle $\phi$ was in proximity to the flow separation point on the cylinder surface. Random noise forcing resulted in a maximum drag reduction of 47%, whereas Gaussian noise forcing resulted in 36% maximum drag reduction. A hybrid flow control strategy implementing the combination of noise forcing and a trip strip at the forward stagnation point were also investigated. A maximum drag reduction of 24% by random noise forcing and 27% by Gaussian noise forcing was observed in this flow control technique.

Acknowledgments

I would like to thank my advisor, Dr. Anwar Ahmed, for providing all the support and guidance in the development of this thesis. No amount of thanks would ever be sufficient for all the advise and critique you have provided throughout my research and in giving me this wonderful opportunity. I would also like to thank Dr. Brian Thurow and Dr. Roy Hartfield for being a part of my thesis committee. Thank you Mr. Andy Weldon in providing the machined components for my experiment. Thanks to Kyle Waldheim, Kyle Johnson, Johnathan Bolton, Dr. Tim Johnson and Richard North in helping me with the experiment setup. Last, but not the least, I would like to acknowledge my family for all the support, encouragement and emotional support through this journey.

Table of Contents

List of Figures

List of Tables

List of Abbreviations

| | |
|---|---|
| $a$ | random noise amplitude |
| $b$ | half wake width |
| $f_s$ | vortex shedding frequency |
| $u$ | instantaneous velocity |
| $\overline{u}$ | mean velocity |
| $u^{'}$ | perturbation velocity, $u^{'} = \sqrt{\frac{1}{N-1}\sum_1^N (u-\overline{u})^2}$ |
| $x$ | value of random variable |
| $C_d$ | coefficient of drag |
| $C_\mu$ | blowing coefficient, $C_\mu = U_j/U_\infty$ |
| $D$ | diameter of cylinder (characteristic length) |
| $L$ | vortex formation length |
| PSD | Power Spectral Density |
| PDF | Probability Density Function $f(x)$ |
| Re | Reynolds Number, $\frac{\rho U_\infty D}{\mu}$ |
| $St$ | Strouhal Number |
| $Tu$ | Turbulence intensity $Tu = u'/U_\infty$ |
| $U_j$ | jet exit velocity from slit |

| | |
|---|---|
| $U_\infty$ | freestream velocity |
| $W$ | velocity deficit at half wake width |
| $W_0$ | maximum velocity deficit |
| $X, Y$ | coordinate system attached to center of cylinder |
| $\phi$ | angle of slit from forward stagnation point |
| $\sigma$, $s$ | standard deviation of Gaussian noise signal |
| $\theta$ | momentum thickness in the wake, $\theta = \int_{-\infty}^{\infty} \frac{U}{U_\infty}\left(1 - \frac{U}{U_\infty}\right)\, dy$ |

# Chapter 1

# Introduction

## 1.1 Flow over a Bluff Body

Flow over a bluff body has been a topic of extensive investigation, due to its interesting fluid dynamical characteristics and a variety of practical applications. Reduction of drag and management of flow around a circular cylinder has been associated with engineering problems of vortex induced vibrations and flow induced noise. A number of investigations have focused on the mechanics of vortex formation and action of periodic forces on cylinders. Although a circular cylinder has a fairly simple geometry, the flow contains a rich diversity of behavior such as interaction between the separated shear layers in the wake,shedding of vortices and onset of instabilities, response of flow due to presence of perturbation,effect of surface roughness, and their dependence of Reynolds number. The existence of various turbulence scales in the wake and their mutual interaction in terms of energy distribution have been investigated by numerous researchers. Among the research being performed on circular cylinders, the most prominent aspect of flow that has been primarily investigated is the formation of periodic shedding of vortices from both sides of the cylinder, termed as the von Kármán vortex street. Works of Zdravkovich [1], Gerrard [3], Berger and Wille [4], Oertel [5], Williamson [6], and Roshko [7] primarily relate to the qualitative and quantitative understanding of the von Kármán vortex street and its influence on the remainder of the flow downstream. Vortex shedding has been identified as the primary mode of instability and is a unique feature of the bluff body flow, starting off after a Reynolds number of 200 and having a characteristic frequency which is expressed non-dimensionally as the Strouhal

number.

$$St = \frac{f_s \, D}{U_\infty}$$

where $f_s$ is the frequency of vortex shedding, $D$ is the diameter of the cylinder, and $U_\infty$ is the freestream velocity.

During the process of vortex shedding, the flow characteristics mainly depend on the governing parameter which is the Reynolds number of flow. Also, as a consequence, vortex shedding tends to behave similar to that of a nonlinear oscillator. With an increase in Reynolds number, the flow over the circular cylinder begins to bifurcate in a nonlinear fashion to higher levels of periodicity until finally reaching fully turbulent state. The aspect of vortex shedding, especially the frequency at which the vortices are shed is of vital importance to practical applications, since the frequency of vortex shedding may coincide with the natural frequency of vibration of the bluff body, giving rise to large scale fluctuations of fluid forces through the process of resonance, in turn causing structural vibrations and ultimately structural failure of the body as a result.

Zdravkovich [1] described that the boundary layer formed around the cylinder was subjected to a favorable pressure gradient upstream followed by a small region of adverse pressure gradient downstream. This leads to separation of the boundary layer from the cylinder surface, forming what are termed as free shear layers. These free shear layers continued to develop downstream, initially bordering the near wake of the body. After a certain Reynolds number is reached, the free shear layers become unstable via occurrence of Kelvin Helmholtz instability. This results in rolling up of the shear layers to form Helmholtz vortices in the classic von Kármán vortex street configuration. The shear layers from both sides of the cylinder cross the centerline of the wake at a certain distance from the cylinder, termed as the vortex formation length. The vortex formation length may also be defined as the region where the freestream fluid crosses the center of the wake for the first time due to the process of entrainment. These factors provide contribution to the formation of low pressure region

behind the cylinder, giving rise to drag which acts on the cylinder.

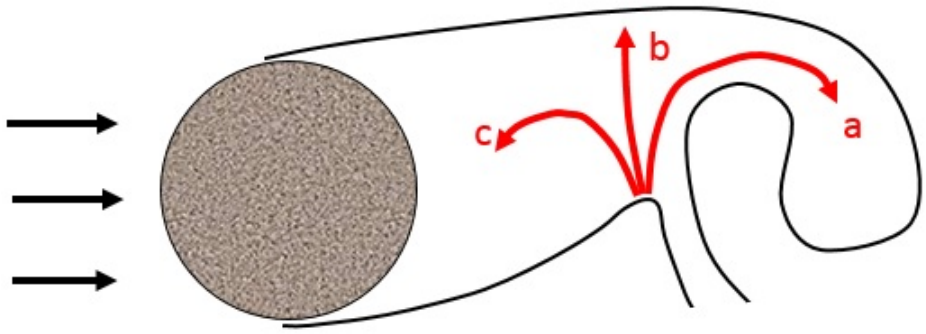


Figure 1.1: Illustration of Shear Layer Entrainment behind a circular cylinder [3]

## 1.2 Regimes of Flow in Circular Cylinder Wake

In his seminal work, Theodore von Kármán analyzed the stability of vortex street configurations and provided theoretical evidence linking vortex street structures and drag of the body. Gerrard [3] indicated that the primary forming vortex draws the shear layer of opposite signed vorticity from the other side of the wake across the wake centerline, eventually negating the supply of vorticity to the growing vortex. At the start of motion of the vortex street, the wake cavity contains a symmetrical pair of equal and opposite recirculating flow regions on either side of the wake centerline. When the vortices are being shed, the wake cavity opens up and instantaneous "alleyways" of fluid penetrate the wake, as shown in Figure 1.1. A generalized phenomenon with increase of Reynolds number is associated with a sequence of fundamental shear flow instabilities take place in the following order:

1. Wake Transition.

2. Shear Layer Transition.

3. Boundary Layer Transition.

A majority of the wake region behind a bluff body till about a Reynolds number of 49 constitutes the primary flow regime which consists of a steady recirculation region of two symmetrical eddies on each side of the wake, illustrated in Figure 1.2. The length of this recirculation grows with increasing Reynolds number [1].

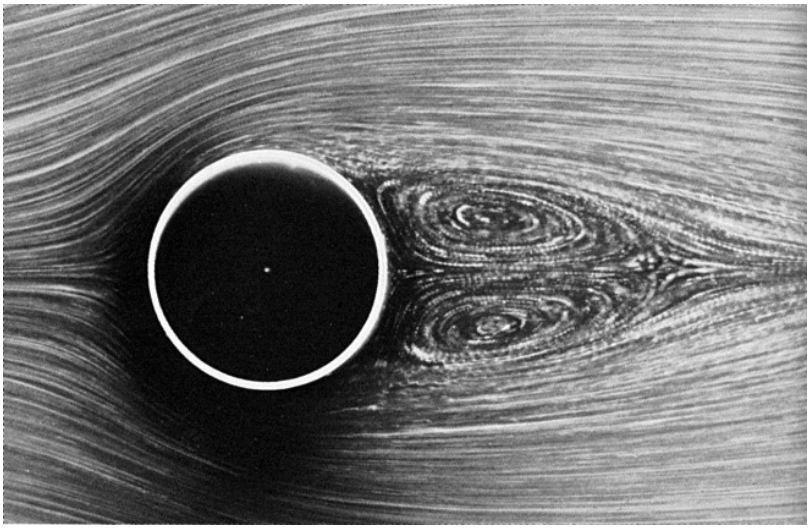

Figure 1.2: Steady Recirculation Region (Re $<$ 49) [2]

As freestream Reynolds number is increased to values ranging between 140 and 200, the recirculation region develops Kelvin-Helmholtz instabilities starting from the downstream end of the recirculation bubble, shown in Figure 1.3, whose strength and magnitude grow with increasing Reynolds number, measured by a monotonic increase in amplitude of maximum wave velocity fluctuations and gradual movement of the formation region upstream toward the cylinder. Also observed is that as Reynolds number increases, the magnification of wake instability results in increase of Reynolds stresses in the near wake region.

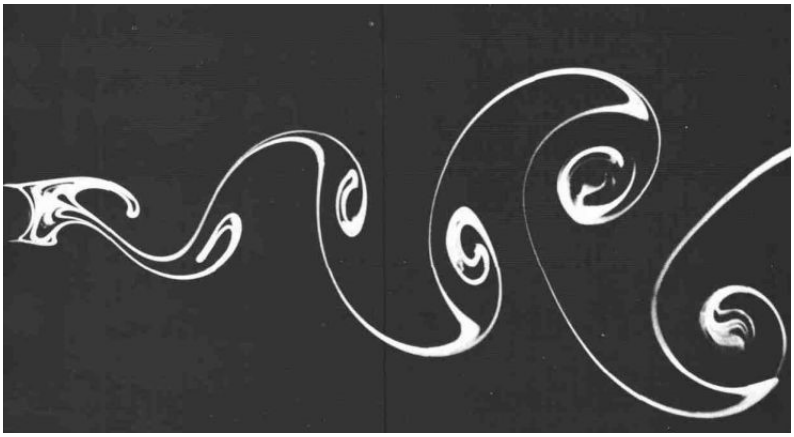

Figure 1.3: Laminar Vortex Shedding (Re $<$ 200) [2]

In the subsequent flow regime ranging from Reynolds numbers of 1,000 to 200,000, a change in Strouhal number is observed with a gradually decreasing trend. This is caused by the developing instabilities of separating shear layers. This flow regime is also accompanied by an increase in drag, while the separation point moves upstream with increasing Reynolds numbers. Bloor [8] pointed out that instability vortices appearing in the shear layers generate wake shedding frequencies and vary with $Re^{3/2}$ , rather than directly with Reynolds number. The Kelvin- Helmholtz instability is primarily two-dimensional in the free shear layers which results in an increase in Reynolds stresses. This regime of flow behind a generic bluff body is termed as the Sub-critical flow regime. An illustration of this flow regime is shown in Figure 1.4.

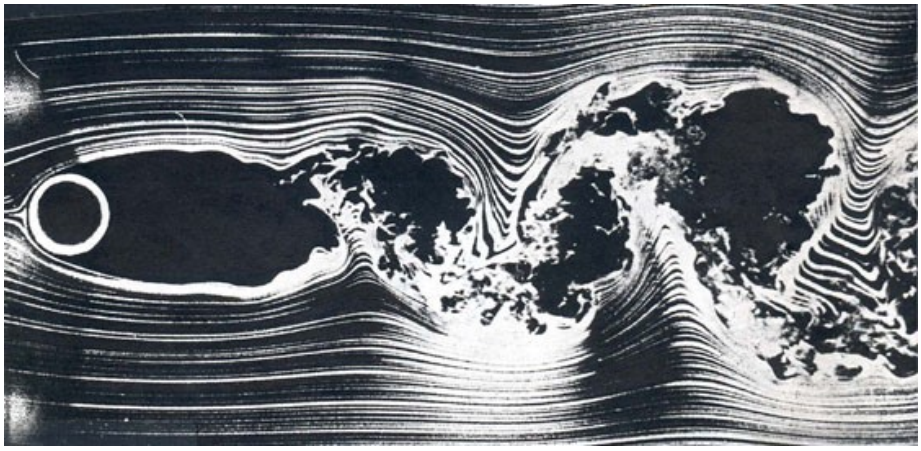

Figure 1.4: Sub-critical Flow Regime (1000$<$ Re $<$ 200,000) [2]

As Reynolds number is gradually increased towards the critical transition flow regime, a drastic increase in drag occurs due to the formation of a separation-reattachment bubble on the leeward side of the wake causing the boundary layer to separate further downstream, resulting in a reduced wake width. Further increase in Reynolds number to the super-critical flow regime results in the formation of two symmetric separation-reattachment bubbles on either side of the body. Considerably higher Reynolds stresses in this regime allow the boundary layer to resist greater adverse pressure gradients. As Reynolds number is increased further than that of the super-critical regime results in the movement of turbulent transition point further upstream, until the boundary layer itself becomes turbulent. At this point, the downstream wake is fully turbulent, and little or no coherent vortices are observed.

### 1.3 Aerodynamic Flow Control

Flow control may be defined as the act of modifying a flow to behave in a manner that it would not under normal conditions. Modification of flow over bluff bodies is achieved by controlling of various parameters in order to achieve desired flow characteristics such as alleviation of vortex induced vibration or wake modification for drag reduction or military applications.

One of the primary uses for employing flow control strategies over a bluff body is to provide control of boundary layer separation. In the aircraft industry, a desired delay in boundary layer separation over wings at high angles of attack is beneficial in the prevention of stall. Also, flow control over the wings allows mitigation of wake turbulence caused by the combination of wingtip vortices and the wake behind aircraft. In the areas of propulsion, especially in gas turbine engines, flow control strategies may be employed on compressor blades in order to minimize the onset of blade or tip stall, which could otherwise prove detrimental to performance characteristics of the engine. In the areas of civil engineering, the implementation of flow control minimizes the strength of vortices shed behind buildings and bridges when subjected to crosswind, thereby decreasing aerodynamic load on the structure,

without compromising on structural integrity. In the motorsport industry, flow control is used to modify the flow so as to provide additional grip to the tires on the road and aid in maneuverability of race cars. Similarly, in commercial ground transport applications, utilization of flow control strategies allows decrease of formation of wake behind semi-trucks and tractor-trailers in order to reduce drag and increase fuel efficiency.

The use of transition to fully turbulent wake may also be employed as a means to control flow behind bluff bodies. A turbulent boundary layer has increased momentum near the wall and is therefore more effective in combating adverse pressure gradient, and delay boundary layer separation. However, the advance or delay of transition into turbulence depends on the area and need of application. The research and investigation of flow control on bluff bodies may be classified into two categories:

1. Passive Flow Control

2. Active Flow Control

## 1.4 Passive Flow Control

Flow control techniques achieved using passive means geometric modifications, and addition of supercritical roughness on the bluff body in order to achieve a modified flow in the wake.

### 1.4.1 Geometric Modifications

Owen and Bearman [9] investigated the reduction of vortex induced vibration by affecting the flow for two configurations of bluff bodies, namely a cylinder having a wavy axis, and a cylinder having hemispherical bumps spaced 45 degrees apart on the cylinder surface. They have observed a drag reduction of upto 47% for the cylinder having a sinuous axis, and about 25% reduction in drag from the presence of hemispherical bumps. In both cases, there was a marked suppression in vortex shedding and a reduction in drag. Experimental work

by Nakamura and Igarashi [10] investigates the modification of flow achieved by addition of circular rings having a certain spanwise spacing along a circular cylinder at various Reynolds numbers. The results obtained from their work suggest the formation of junction vortices due to the presence of circular rings on the cylindrical body, which attribute to the formation of separation bubbles resulting in pressure recovery in the near wake of the cylinder, and thereby resulting in drag reduction of upto 15% at a Reynolds number of 30,000. Research conducted by Liu, Shi and Yu [11] examined the comparison of wake structures between circular and V-shaped grooved cylinders. The presence of grooves on the cylinder caused formation of recirculation zones in the grooves, which aided in decrease of pressure and viscous forces and resulted in a much more stable formation of wake behind the grooved cylinder. Examination of contours of streamwise velocity fluctuation suggested a slower growth of shear layers, and an extension of the recirculation zone in the wake of 18%, thereby giving rise to suppression in vortex shedding. The works of Ahmed and Bays-Muchmore [12], Ahmed et al [13] and Chang [14] involved the investigation of flow characteristics of wavy cylinders subjected to crossflow. The formation of wake behind nodal points of attachment was narrower and had faster velocity recovery rates compared to the saddle points of attachment, giving rise to phase difference in the vortex shedding behind the wavy cylinder, causing destructive interference between the shedding from nodal attachment points and that of saddle points of attachment, and hence resulting in reduction of drag. Roshko [7], Bearman [15], Anderson and Szewczyk [16], Kwon and Choi [18], Ozono [19] and Hwang et al [20] investigated the effect of placing a splitter plate at or near the trailing edge stagnation point of bluff bodies. The presence of a splitter plate forced a delay in the interaction of the top and bottom shear layers, causing extension of the recirculation behind the body and an increase in base pressure, indicating suppression of formation of vortices in the wake. Experiments performed by Randeria [17] investigated the nature of flow behind a curved cylinder consisting of nodal and saddle points using surface flow visualization, Pitot tube and hot wire measurements in the wake. Surface flow visualization indicated formation of spanwise flow from the cylinder's

nodes to its saddles. Foci structures were also observed on the cylinder surface, increasing in strength with increasing azimuthal angle from nodal to saddle position. Water tunnel flow visualization of the curved cylinder indicated the presence of vortical structures other than the von Kármán vortices. Change of azimuth angle from nodal to saddle position resulted deterioration of organized flow. Larger drag at saddle position was observed, which was very different when compared to the right circular cylinder, confirming that a three- dimensional wake exists behind the bent cylinder.

### 1.4.2 Surface Protrusions

Ekmecki and Rockwell [21] investigated the flow by placing a surface disturbance on a circular cylinder, namely a large-scale spanwise wire. It was observed that the placement of the spanwise wire affected only one shear layer, but the consequences of this local disturbance was felt globally over the entire wake. Two critical angles of wire placement were observed from their results. The angular location of the wire between these two critical angles resulted in the interaction of shear layer with the wire, causing shear layer instability, allowed the reattachment of flow due to the formation of a small recirculation region behind the spanwise wire, causing contraction of the time-averaged recirculation region in the wake of the cylinder, and a reduction of vortex shedding, thereby a decrease in drag. Placement of the wire after the second critical angle resulted in the expansion of the recirculation region, intensifying the strength of Kármán vortices.

The implementation of helical strakes has been investigated by many researchers such as Wong and Kokkalis [22], Scruton and Walshe [23], Woodgate and Mabey [24], and by Every, King and Weaver [25]. The interaction of flow with the helical strakes induced vortices having different shedding frequencies than the natural shedding frequency of the cylinder, which helped in breakdown in vortex formation behind the cylinder, increasing the base pressure and hence decreasing drag. The work by Yoon [26] achieved in drag reduction and breakdown of Kármán vortices behind bluff bodies by placing spanwise rectangular tabs of

various heights and widths at specific locations. The tabs caused a phase mismatch in the process of vortex shedding behind the body, breaking down the vortices and enhancing the rate of mixing in the wake.

### 1.5 Active Flow Control

The implementation of active flow control constitutes the addition of energy to the flow of a bluff body. Tokumaru and Domitakis [27] performed experiments with oscillatory cylinders subjected to a high-frequency rotation in order to control formation of the wake. A peak rotation was chosen in such a way that the circumferential velocity of the cylinder surface is comparable to the velocity of flow outside the boundary layer. The greatest control authority was accomplished when the forcing frequency was synchronized with that of vortex shedding. The use of transverse vibrating cylinders by Koopman [28] showed that when the amplitude of vibration of the cylinder, driven at the frequency of vortex shedding was increased, the originally slanted vortex filaments in the non-vibrating case aligned parallel to the cylinder, observing a reduction in lateral spacing between wake vortices. Research by Wood [29] and Bearman [30] incorporated base bleed as a means to suppress Kármán vortex formation. It was observed that with increase of base bleed strength, the strength of vortex formation decreased accordingly. Investigations by Fransson, Koneiczny, and Alfredsson [31] on the flow around porous circular cylinders subjected to continuous suction or blowing, yielded that relatively low suction or blowing rates had a pronounced effect on the wake. Suction and blowing rate was varied as a ratio of freestream velocity. When a suction strength of -2.5 was applied on the flow, the separation line of vortex formation was moved further downstream, resulting in shrinkage of wake and a drag reduction of up to 70% on the cylinder. However, the effect of blowing on the flow proved detrimental to the flow characteristics, resulting in expansion of the wake, thereby increasing drag on the cylinder. Chen, Hu and Li [32] also performed similar investigations, using two suction holes on the cylinder situated at 90 degrees to the oncoming flow, close to the separation point of flow

on the cylinder. This achieved good control over the wake, resulting in reduction of average lift and drag fluctuation on the cylinder model. The influence of suction on the flow is also indicated by the change of the mode of vortex shedding from asymmetrical mode to symmetrical mode.

### 1.6 Application of Acoustics for Flow Control

The research performed by Detemple-Laake and Eckelmann [33] investigated the application of sound waves on the flow over circular cylinders to study the coupling mechanism between forcing and periodic vortex shedding in the wake, for Reynolds numbers ranging between 50 and 250. As many as twelve modes of vortex shedding were observed for various ratios of sound frequency and natural shedding frequency, ranging from 0.5 to 4, and the forcing amplitude. Investigations by Blevins [34] on the effects of vortex shedding by application of a 143.5 dB sound wave at the shedding frequency have shown that the incoherent and irregular spanwise vortices shed downstream of the cylinder shifted the shedding frequency to that of the applied sound frequency and aligned parallel to the cylinder, the signals of which were monitored by four flush film sensors on various spanwise locations on the cylinder.

Hsiao and Shyu [35] investigated the introduction of acoustic waves through a thin slit on the cylinder surface. The results showed that when the acoustic excitation frequency was close to the frequency of shear layer instability, there was a maximum observed reduction in drag, with a consequential reduction in vortex shedding amplitude. Flow visualization showed that the perturbation introduced by acoustic excitation shrunk the size of Kármán vortices, along with reduction in shedding amplitude. Huang [36] has also performed similar research, at Reynolds numbers ranging from 4,000 to 8,000. The introduction of pure tone sound through a slit on the cylinder surface at appropriate sound levels suppressed the formation of Kármán vortices. His work also stated that a relatively weak sound intensity (about 80 dB) was needed to disrupt the formation of vortices in the wake, as compared to

higher levels of acoustic output in previous research. Fujisawa and Takeda [37] performed experimental techniques using Particle Image Velocimetry (PIV) in order to visually quantify the effect of internal acoustic excitation on the wake of a circular cylinder at a Reynolds number of 9000. It was noted from the research that when the acoustic excitation occurred at a slit angle just behind the separation point of flow, a recirculation bubble is formed at the location of excitation which allows for freestream flow to reattach onto the cylinder surface, thereby promoting reduction in wake width, and a drag reduction of up to 30% on the cylinder.

## 1.7 Present Research

The plethora of earlier experiments involving Internal Acoustic Excitation implemented the use of periodic forcing that has either a frequency equal to that of vortex shedding or a harmonic of the vortex shedding frequency. Research by Bhattacharya [39] investigated the three-dimensional effects of periodic forcing on a circular cylinder having two sinusoidal slits located at diametrically opposite locations on the cylinder at Reynolds numbers of 38,000 and 45,000. His work pointed out that a sufficient blowing coefficient required to create a three dimensional disturbance breaks down the vortex formation into smaller eddies. Due to this, the wake was uniformly distributed in the smaller turbulent structures from the primary shedding component. This caused acceleration of the two separating shear layers due to forcing, narrowing the wake and providing a drag reduction of up to 45%. Similar research was performed on two-dimensional aspect of flow control by Moore [40], conducting experiments on a circular cylinder having two straight slits situated diametrically opposite on the cylinder surface at Reynolds numbers of 12,000 and 24,000, investigating on the in-phase and out-of-phase effects of periodic forcing. At a forcing frequency lesser than or equal to the vortex shedding frequency, the strength of vortex shedding showed an increase in magnitude. Sub-harmonic and harmonic forcing frequencies interacted with the shear layers at the top and bottom of the cylinder to initiate an instability by either synchronizing with

the natural shedding frequency for out-of-phase cases, or by adding kinetic energy to the vortex formation in the in-phase cases. An excitation frequency of four times the shedding frequency provided 28% reduction in drag for the in-phase case and a 26% drag reduction for out-of-phase case. Moore also investigated the effect of a Random Noise signal and the effect that Noise had on the vortex shedding phenomenon. The results show that Random Noise forcing was successful in the complete elimination of shedding peak as seen in shear layer spectra, and a narrowing of the wake and a decrease in vorticity concentration from PIV data.

DeMauro, Leong and Amitay [38] performed experiments on a finite span cylinder with internal acoustic excitation, and the effect of acoustic excitation on the two-dimensional Kármán vortices and three-dimensional flow phenomenon associated with the downwash from the free end of the cylinder. The results from their experiments point out that the interaction of the synthetic jet with the near wake led to increased mixing of downwash from the open end, resulting in a narrowed and vectored wake. The downwash redirection led to separation of smaller regions having high vorticity from the location of streamwise vorticity and pushed downward toward the cylinder base. These separated regions had a shedding frequency similar to that found in two-dimensional cylinders, suggesting a reduction of downwash effect.

Naim, Greenblatt, Seifert and Wygnanski [44] investigated on the wake of a circular cylinder at transitional Reynolds numbers. The cylinder model consisted of a single tapered slot which was oriented either upstream or downstream with the freestream flow direction. Their results show that even the passive presence of the slot even when taped over had a pronounced effect on transition and flow separation. Two-dimensional periodic forcing offered greater flexibility compared to passive methods in the alteration of lift and drag on the cylinder. Investigations performed by varying the amplitude of momentum coefficient and orientation of acoustic excitation provided a variety of results. Lower momentum coefficients in the direction opposing that of freestream flow proved more effective than when compared

to that at the same direction as of freestream flow. Higher values of momentum coefficients caused boundary layer separation on the fore-body of the cylinder. Pulse modulated excitation frequency when closer to the vortex shedding frequency exhibited a lock-on phenomenon which increased drag by forming closer to the cylinder. Higher excitation frequencies had an analogous effect as that of pure tone excitation, resulting in delayed separation and drag reduction.

As observed from previous research, active flow control using internal acoustic excitation, at a single forcing frequency at either the the fundamental frequency or at a harmonic of shedding frequency resulted in relying heavily on narrow-band acoustic excitation. The motivation behind the present research was to investigate the effect of broadband acoustic excitation, using random and Gaussian noise as the source. By exerting a broadband excitation, the vortex shedding naturally locks-on to any frequency present in the excitation signal, at an appropriate blowing coefficient. Thus, the wake self-selects the frequencies for attenuation of large structures. The present research also investigates hybrid flow control strategies, by implementing a turbulent transition strip in combination with broadband noise forcing to examine the effect of hybrid flow control over the wake of a circular cylinder.

# Chapter 2

# Experimental Setup

Experiments were conducted in the Auburn University 4ft x 3ft closed circuit, low speed wind tunnel. The contraction ratio from the inlet diffuser to the test section is 5. Wind tunnel speed was monitored electronically and by use of a differential manometer. The freestream turbulence in the test section of the wind tunnel was found to be approximately 0.5%, and also a non-uniformity of approximately 1% in the flow ([39],[40]).

## 2.1 Cylinder Model

Experiments were conducted on hollow cylindrical models made from resin on a three-dimensional printer (Figure 2.1).The cylinder was internally partitioned thus forming two independent cavities with exit slits. Each cavity was separately connected to an acoustic driver pair to exit individually from each slit. The outer diameter of the cylinder model was $D = 1.625$ inches, having a length of $5.53D$, and a thickness of $0.055D$. The length of the straight slits was $4D$, and a width of $0.0015D$. The cylinder model was attached between two wall inserts mounted in the test section. The wall inserts were made of 1 inch thick particle board with the provision of large acrylic windows for facilitating PIV measurements. The wall inserts were held in place using L-brackets bolted to the test section floor and ceiling.

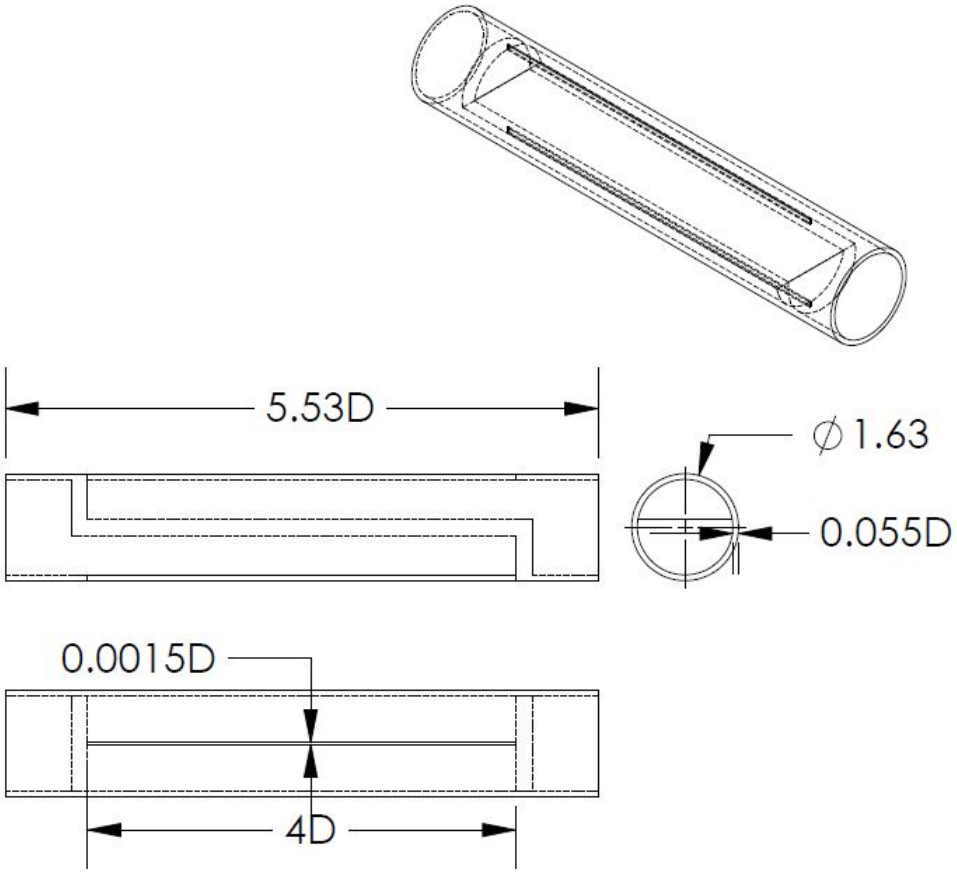


Figure 2.1: Cylinder Model

## 2.2 Acoustic Drivers

Random and Gaussian noise forcing was applied using two pairs of acoustic drivers, consisting of two Infinity Reference 12 inch 1000 watt sub-woofers situated on top of the test section ceiling, and two Infinity Reference 8 inch 860 watt sub-woofers situated in the test section in-line with the cylinder axis. The acoustic drivers were connected to two separate power amplifiers (MBIS SS500 for 12 inch drivers and MB Dynamics SS250VCF for 8 inch drivers respectively). Each of the drivers were housed in an acrylic shroud and housing, providing a circular outlet for noise forcing to travel via copper tubing to the slits in the cylinder model. The required voltage input for acoustic driver excitation was in the range

of 9 volts to 16 volts. Special care was taken to ensure the voice coils of the drivers did not overheat or damage during experiments.

### 2.3 Data Acquisition System

Data acquisition from hot wire and Pitot probes was performed by a National Instruments data acquisition board (NI PCI-6035E), situated in the CPU of a computer. A daughter board (CB-68LP) situated outside the computer, attached to the DAQ board provided means to connect inputs from the hot wire and Pitot probes, and also provided Analog output for Random and Gaussian Noise forcing signals to the acoustic drivers through the power amplifiers, the noise waveforms generated using LabVIEW 12.0. Raw voltage samples from the Pitot probe and hot wire CTA probe were processed in LabVIEW, which provided data for calculating velocity profiles, shear spectra, vortex formation and turbulent quantities in the wake using MATLAB.

### 2.4 Wake Pressure Survey

The Pitot probe was attached to a Validyne DP45-16 differential pressure transducer. A Validyne CD-12 Carrier Demodulator was connected to the pressure transducer which allowed for excitation, amplification and demodulation of transducer voltage. Output from the CD-12 carrier demodulator was connected to the DAQ board via a daughter board. The raw voltage signals of which were acquired in LabVIEW and analyzed using MATLAB.

### 2.5 Constant Temperature Anemometer

Measurement of wake power spectra and other turbulent quantities in the wake of the cylinder model was performed by a Dantec Dynamics 55P11 single wire probe of 5$\mu$m diameter and a length of 1.25mm. The probe was connected to a Dantec Dynamics 54T30 Constant Temperature Anemometer (CTA) module via a BNC cable. Total resistance of

the hot wire system was calculated by addition of the cold resistance of the hot wire, cable resistance and probe holder resistance, which were measured by a digital multimeter. These values were input to an Excel worksheet provided by the manufacturer which provided appropriate dip switch positions located in the CTA module. The overheat ratio of the wire was kept at 0.8, and dip switches adjusted in the CTA module resulting in an operating temperature of 220° C.

The output from the CTA module was connected to the NI PCI 6035-E DAQ board by means of a BNC cable via the daughter board in a differential mode. The raw voltage signals were converted to appropriate velocities using calibration data (see Appendix). This provided computation of wake spectra, perturbation velocity, and vortex formation length.

### 2.6 Pitot Probe and Hot Wire Probe Traverse System

The Pitot and hot wire probes were connected to a streamlined Aluminum support attached to the traverse mechanism situated on top of the wind tunnel test section. The traversing system consisted of an orthogonal arrangement of two threaded rods, situated in aluminum housings and the rotation of which are controlled by two stepper motors. This arrangement was connected to a two-axis Velmex VP9000 traverse controller that was connected to the computer by means of RS-232 serial port. Programs written in LabVIEW provided communication to the Velmex traverse system.

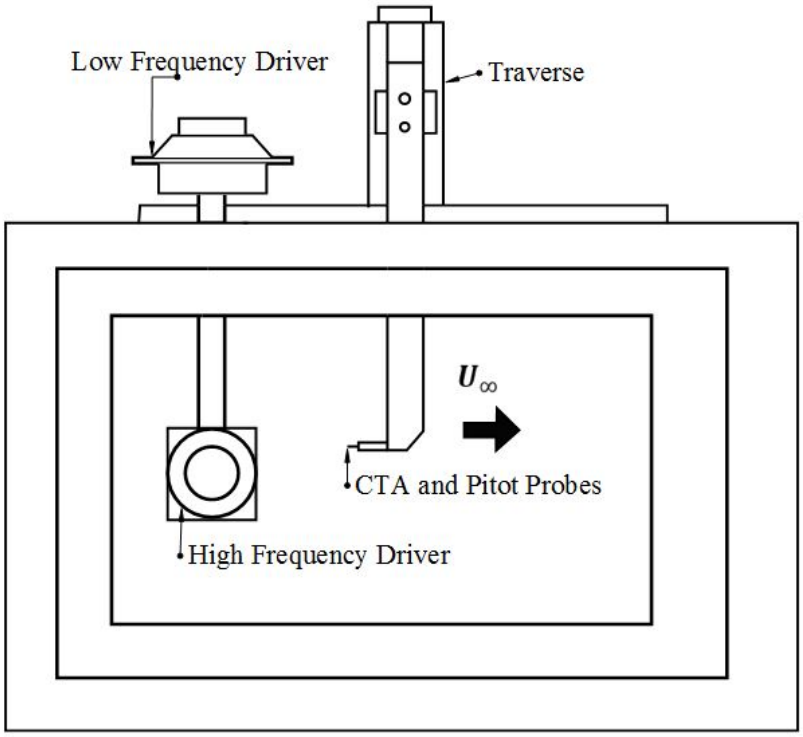


Figure 2.2: Front View of Experiment Setup

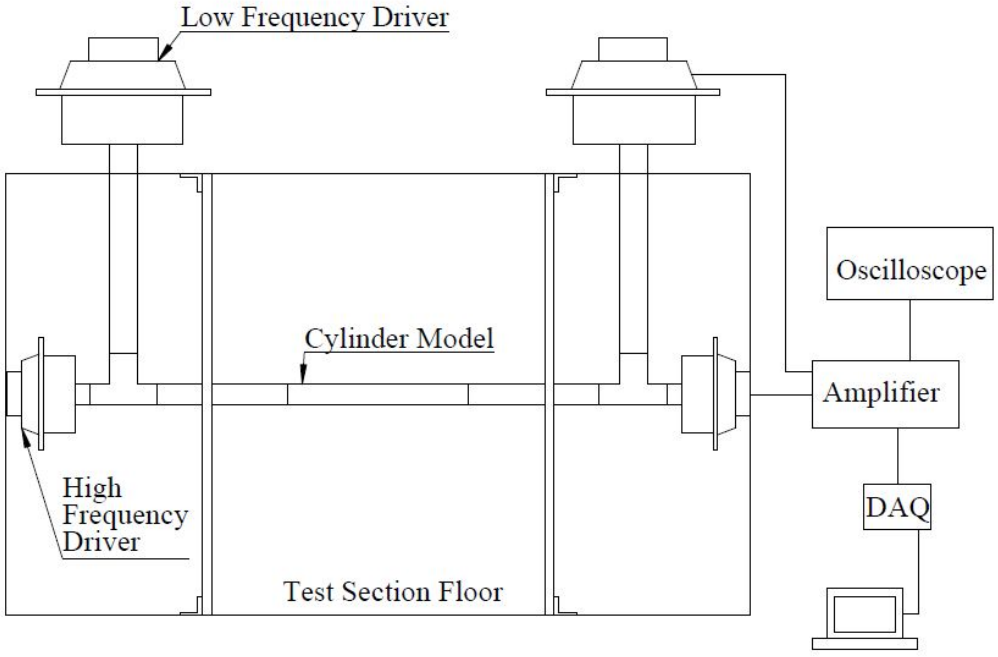


Figure 2.3: Noise Forcing Setup

# Chapter 3

## Results and Discussion

Experiments were conducted at a freestream velocity of 15 ft/s, resulting in a Reynolds number of 12,000 based on the cylinder diameter. To determine the blowing coefficients of noise forcing $C_\mu$ , the hot wire was placed in front of the straight slit oriented at 180° from the forward stagnation point of the cylinder.

For the baseline (no forcing) case, both slits were taped over in order to prevent suction of boundary layer into the slit. For two slit noise forcing, measurements were made with slits oriented at $\phi = \pm$ 90° . For single slit measurements, azimuthal location of single slit was varied manually from $\phi$ =60° to $\phi$ =90° . In the case of cylinder with tripped boundary layer, measurements were made from $\phi$ =90° to $\phi$ =105° .

### 3.1 Mechanism of Noise Forcing

The mechanism of flow control achieved by the action of synthetic jets has been extensively reviewed by Glezer [42]. For a baseline flow (no forcing case), the separation of flow caused large-scale shedding of von Kármán vortices into the wake. These time-periodic vortices strongly affected the evolution of separating shear layer. His paper also indicated that a pronounced interaction between periodic shedding and separated shear layer was observed in the presence of synthetic jet. The coupling between the two flows were termed to produce collective interactions during shear layer roll-up and vortex formation in the wake. Glezer also stated that the interaction of synthetic jet with local cross flow over the surface of a bluff body produced localized concentrations of "trapped" voricity. The formation of such a layer of trapped vorticity within the boundary layer of a circular cylinder displaced the exterior cross flow, leading to delayed separation. The flow curvature also changed due to this

interaction, thereby altering the aerodynamic shape of the body, resulting in either partial or complete suppression of separation. For a single slit synthetic jet actuation, displacement of the cross flow in the vicinity of the jet orifice, and delay of separation were in addition to asymmetry in the flow field, which caused narrowing of the wake. The reduction of wake width was accompanied by suppression of vortex shedding in the near wake of the cylinder.

The Probability Density Function (PDF) of a continuous random variable $x$ is a function describing the likelihood of a random variable to take a given value. The PDF of random or white noise was described by the equation

$$f(x) = \begin{cases} \frac{1}{2a}, & \text{if } -a \leq x \leq a \\ 0, & \text{otherwise} \end{cases}$$

where $a$ was the specified noise amplitude.

The equation which described the PDF of Gaussian noise formed a normal distribution or a Bell curve, given by

$$f(x) = \frac{1}{s\sqrt{2\pi}}\, e^{\frac{-1}{2}\,(\frac{x}{s})^2}$$

where $s$ was the specified standard deviation $\sigma$.

Random and Gaussian noise signals were generated in LabVIEW. The input voltage for both random and Gaussian noise forcing was dictated by the amount of noise amplitude in the case of random noise, and standard deviation in Gaussian noise. Random noise was given a noise amplitude of $a = 1$. The PDF of random noise showed a uniform distribution of the input voltages present in the original signal (Figure A.1). A standard deviation of $\sigma = 0.5$ for Gaussian noise provided the desired blowing coefficient without risking damage to the acoustic drivers. The PDF of Gaussian noise signal showed a normal (Gaussian) distribution of random numbers (Figure A.2). The plots of power spectra of both noise signals (Figures 3.4 and 3.5) show that the spectral content of frequencies for both noise signals were of fairly similar broadband width.

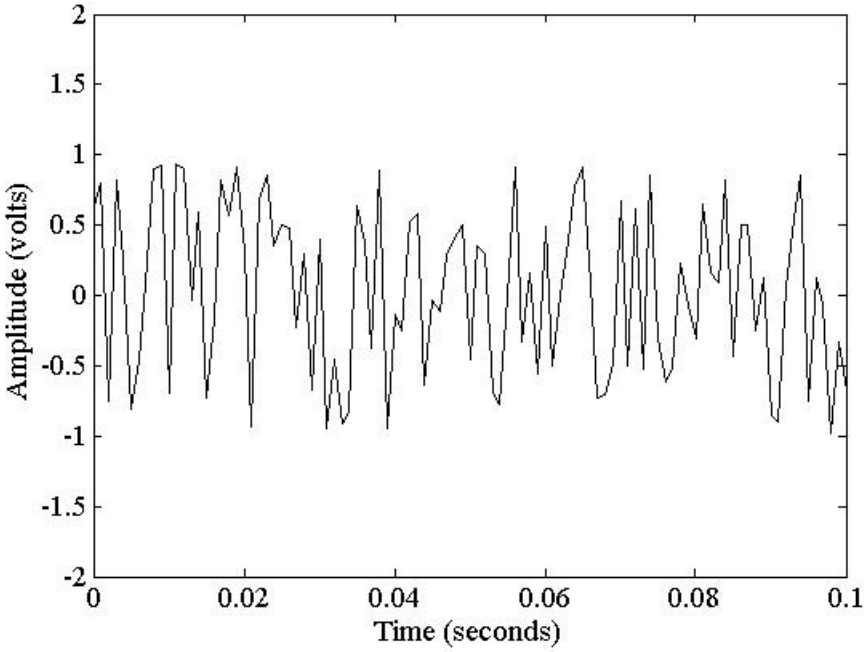


Figure 3.1: Time History of random noise signal

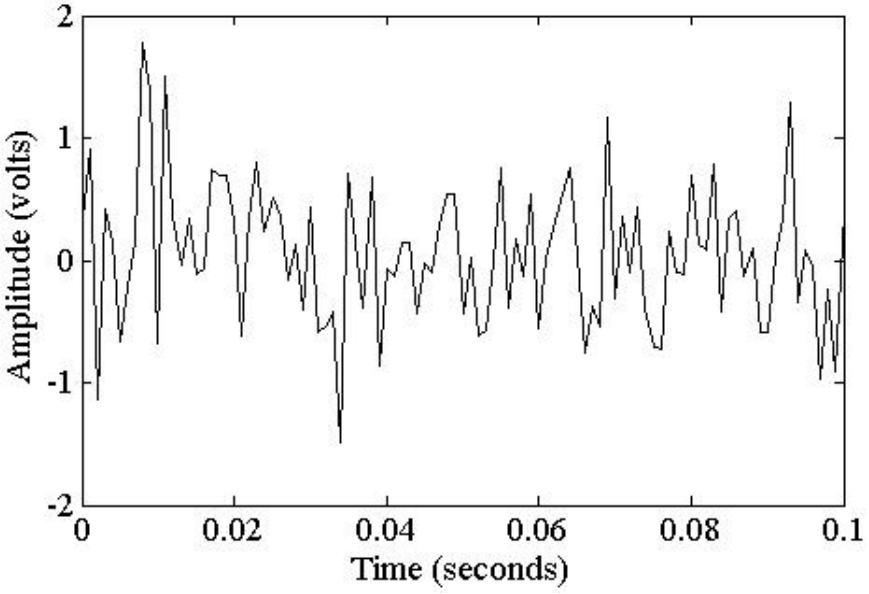


Figure 3.2: Time History of Gaussian noise signal

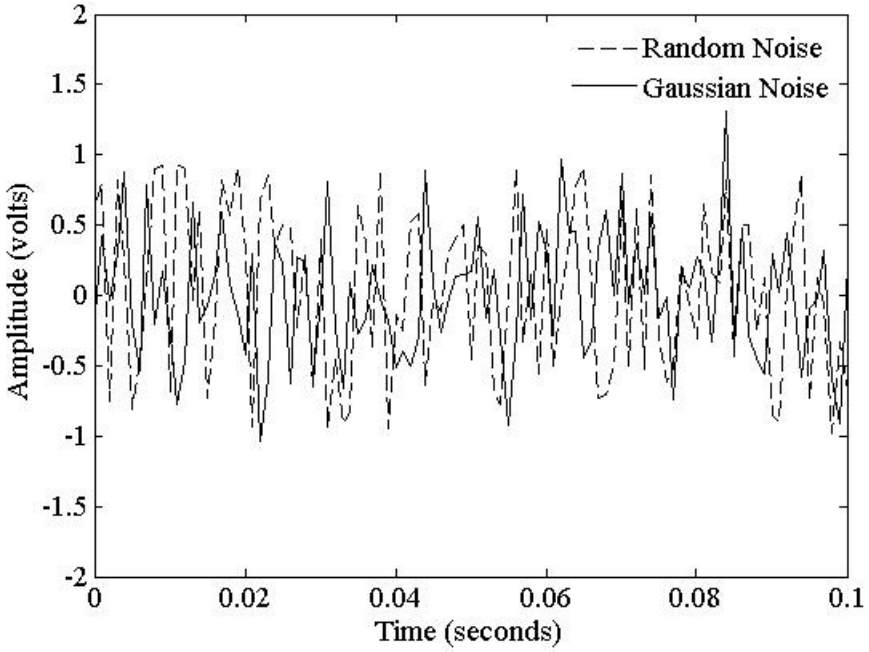


Figure 3.3: Comparison of noise signals

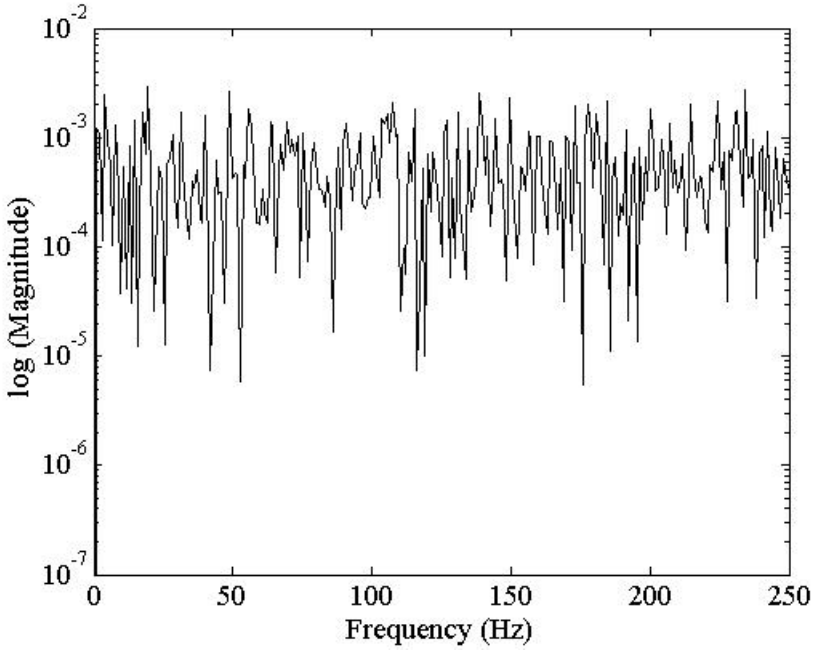


Figure 3.4: Power spectra of random noise signal

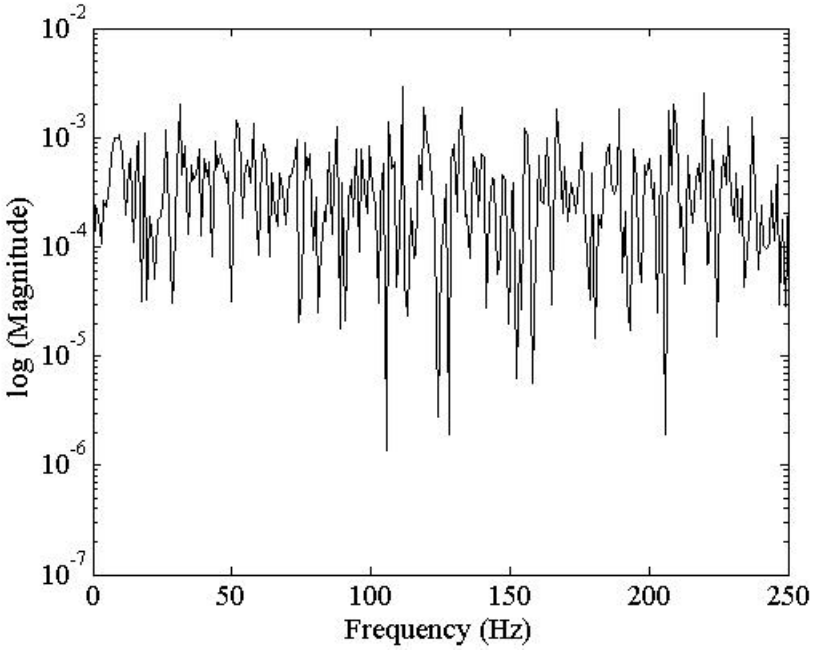


Figure 3.5: Power spectra of Gaussian noise signal

The nature of both random and Gaussian noise forcing was to introduce a synthetic jet consisting of random blowing and suction as a disturbance to the flow over the circular cylinder. Considering the flow in a time-averaged context, re-attachment of the separation bubble caused by the synthetic jet onto the cylinder surface resulted in the displacement of the exterior flow due to the addition of kinetic energy to the separating shear layers. In doing so, noise forcing delayed separation of the boundary layer which resulted in subsequent narrowing of the wake behind the cylinder. Considering the flow at a particular instant of time, the introduction of either random or Gaussian noise resulted in the ejection of smaller - scale vortices having frequencies of the input signal, giving rise to a broadband forcing mechanism as compared to narrowband excitation with periodic forcing, which interacted with the primary instability present in the wake i.e von Kármán vortex street. The interaction of these smaller-scale vortices from noise forcing with the large scale Kármán vortices caused breakdown of the Kármán vortices by allowing the vortex shedding to synchronize or lock - in with the multitude of frequencies present in the jet. This breakdown of the Kármán vortex street resulted in subsequent reduction in drag due to narrowing of the wake [40]. The main focus of this research was to investigate the action of broadband forcing on the dynamics of the wake.

The noise signals shown in Figures 3.1 and 3.2 were affected by the physical behavior of the power amplifiers and physical restrictions of the acoustic drivers. Figures 3.6 and 3.7 show the jet exit time histories acquired by the hot wire. These were used to calculate blowing coefficient $C_\mu$ . From Figures 3.8 and 3.9 it can be seen that the spectra at the jet exit exhibited a slight decay at lower frequencies. This was due to the influence of the physical nature of acoustic drivers combined with that of power amplification. These represent the characteristics of both random and Gaussian noise forcing that affected the formation of von Kármán vortices in the wake.

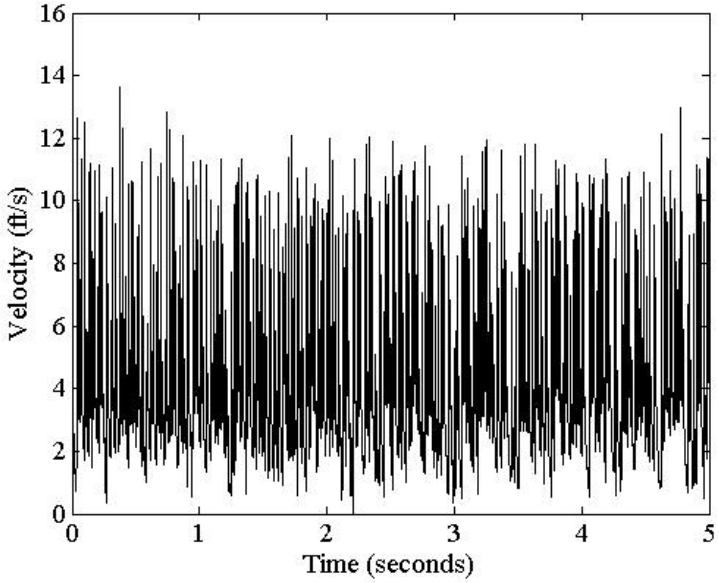


Figure 3.6: Jet exit time history, random noise forcing

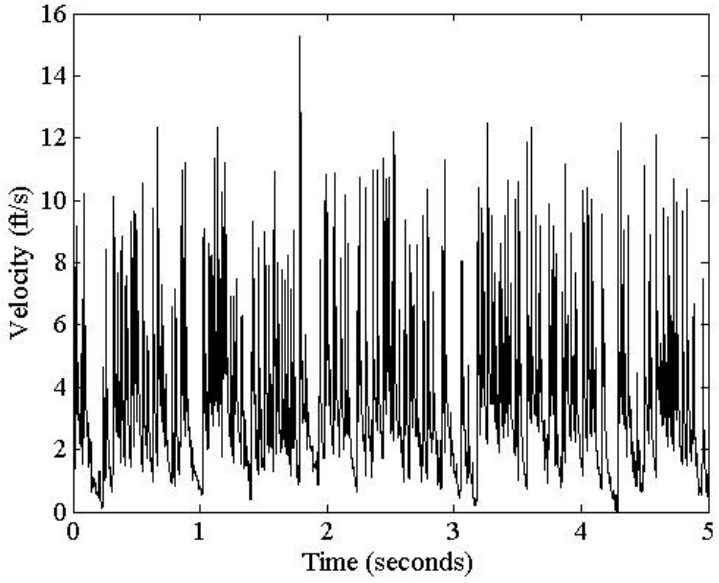


Figure 3.7: Jet exit time history, Gaussian noise forcing

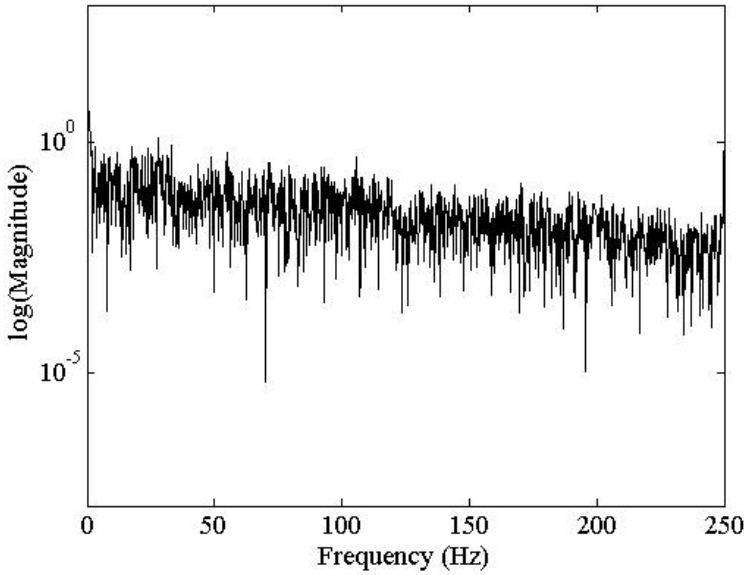


Figure 3.8: Spectra at jet exit, random noise forcing

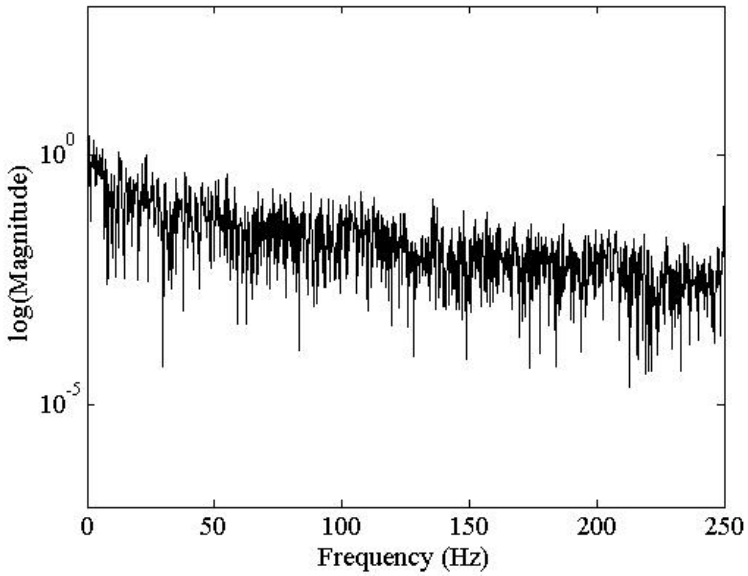


Figure 3.9: Spectra at jet exit, Gaussian noise forcing

Table 3.1: Blowing Coefficients of noise forcing

| Noise forcing type | Blowing Coefficient $C_\mu = U_j/U_\infty$ |
|---|---|
| Random noise forcing | 0.497 |
| Gaussian noise forcing | 0.43 |

### 3.2 Mean Velocity Profiles

Mean velocity profiles were acquired by the Pitot probe traversing through the wake from $\frac{Y}{D} = -4$ to $\frac{Y}{D} = 4$. These profiles illustrated the effect of noise forcing on the mean wake of the cylinder. The velocity profiles were processed in MATLAB to deduce drag coefficients $C_d$ using piece-wise trapezoidal integration across the wake. Tables 3.2 through 3.5 contain drag coefficients for the measured velocity profiles.

In the case of two slit forcing (Fig. 3.10a), a symmetrical reduction of the velocity profile was observed, random noise forcing providing increased efficiency in contraction of the wake compared to Gaussian noise forcing. Synthetic jet actuation from the top and bottom slits affected both the top and bottom shear layers separating from the cylinder surface, causing excitation of the shear layers and resulted in a drag reduction of 25% for random noise forcing and 21% for Gaussian noise forcing.

Single slit forcing cases for the smooth cylinder showed an asymmetrical variation in velocity profile. This was caused by the increased effect of noise forcing felt on the top shear layer, thereby providing increased acceleration of flow along the top surface of the cylinder, as seen from Figures 3.10b to 3.11d. Noise forcing generally showed an increase in effectiveness as the slit angle $\phi$ was increased from $\phi = 60°$to $\phi = 90°$. The results of Fujisawa and Takeda [37] also supported the evidence of increased drag reduction when single synthetic jet actuation along any one surface of a circular cylinder was situated in close proximity to the point of separation of boundary layer on the cylinder surface. The general trend observed for all forcing cases was that random noise provided effective drag reduction compared to Gaussian noise. Random noise forcing provided a drag reduction of 20% at $\phi = 60°$. At $\phi = 90°$, random noise forcing showed a drag reduction of 47%, as calculated from Table 3.2. Gaussian noise forcing provided a drag reduction of 18% at $\phi = 60°$. Maximum drag reduction observed for Gaussian noise forcing was 36% at a slit angle of $\phi = 90°$. As the slit angle was increased, it was observed that the vectoring of the wake was also increased. This also was attributed to the fact that as the noise forcing reached a location in close proximity

to the boundary layer separation point on the cylinder, the effect and acceleration of the top shear layer was increased, causing increased asymmetry in the wake velocity profiles, and hence further reduction in drag.

The effect of placing a turbulent strip at the forward stagnation point of the cylinder was prominent as observed from the velocity profiles in Figure 3.12a. No forcing case for this configuration resulted in an inherent drag reduction of 18% . This is attributed to the increase in skin friction drag caused by the presence of surface roughness. This resulted in addition of energy to the boundary on the cylinder, delaying separation.

Two slit forcing for the case of tripped cylinder showed that the velocity profiles have widened in the near wake of the cylinder. This was due premature flow separation occurring due to the action of noise forcing on both top and bottom shear layers of the cylinder wake. Random noise forcing provided a drag reduction of only 8% , whereas Gaussian noise forcing resulted in a drag reduction of 20% (Fig. 3.12b).

Single slit noise forcing on the top surface for the cylinder fitted with turbulent strip at slit angles ranging from $\phi = 90^\circ$ to $\phi = 105^\circ$ showed remarkably different trends in the values of $C_d$ when compared to those of smooth cylinder cases (Tables 3.4 and 3.5). Gaussian noise forcing proved more effective than random noise forcing for all these cases. Random noise forcing resulted in a drag reduction of upto 24% at slit angles ranging from $\phi = 90^\circ$ to $\phi = 100^\circ$ and a 17% drag reduction at $\phi = 105^\circ$ . Gaussian noise forcing showed a maximum drag reduction of 28% at slit angle $\phi = 100^\circ$ . Drag reduction of 27%, 21%, and 20% were observed for Gaussian noise forcing at slit angles of $\phi = 90^\circ$ , $\phi = 95^\circ$ and $\phi = 105^\circ$ respectively (Figures 3.12c to 3.13b).

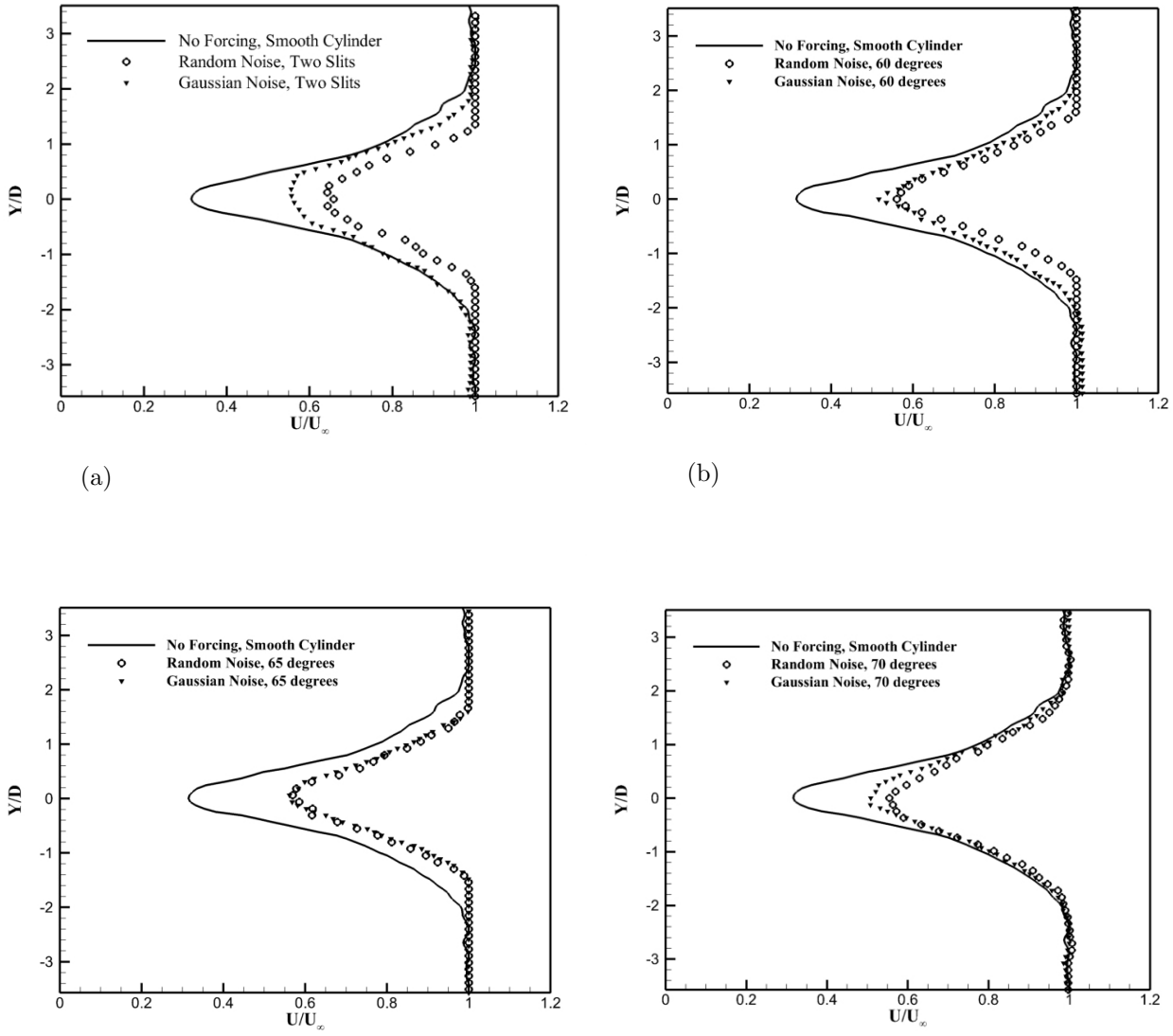


Figure 3.10: Mean velocity profiles, $\frac{x}{D} = 4$, Smooth cylinder: (a) Two slit forcing,(b) Single slit forcing, $\phi = 60°$ (c) Single slit forcing, $\phi = 65°$ , (d) Single slit forcing, $\phi = 70°$

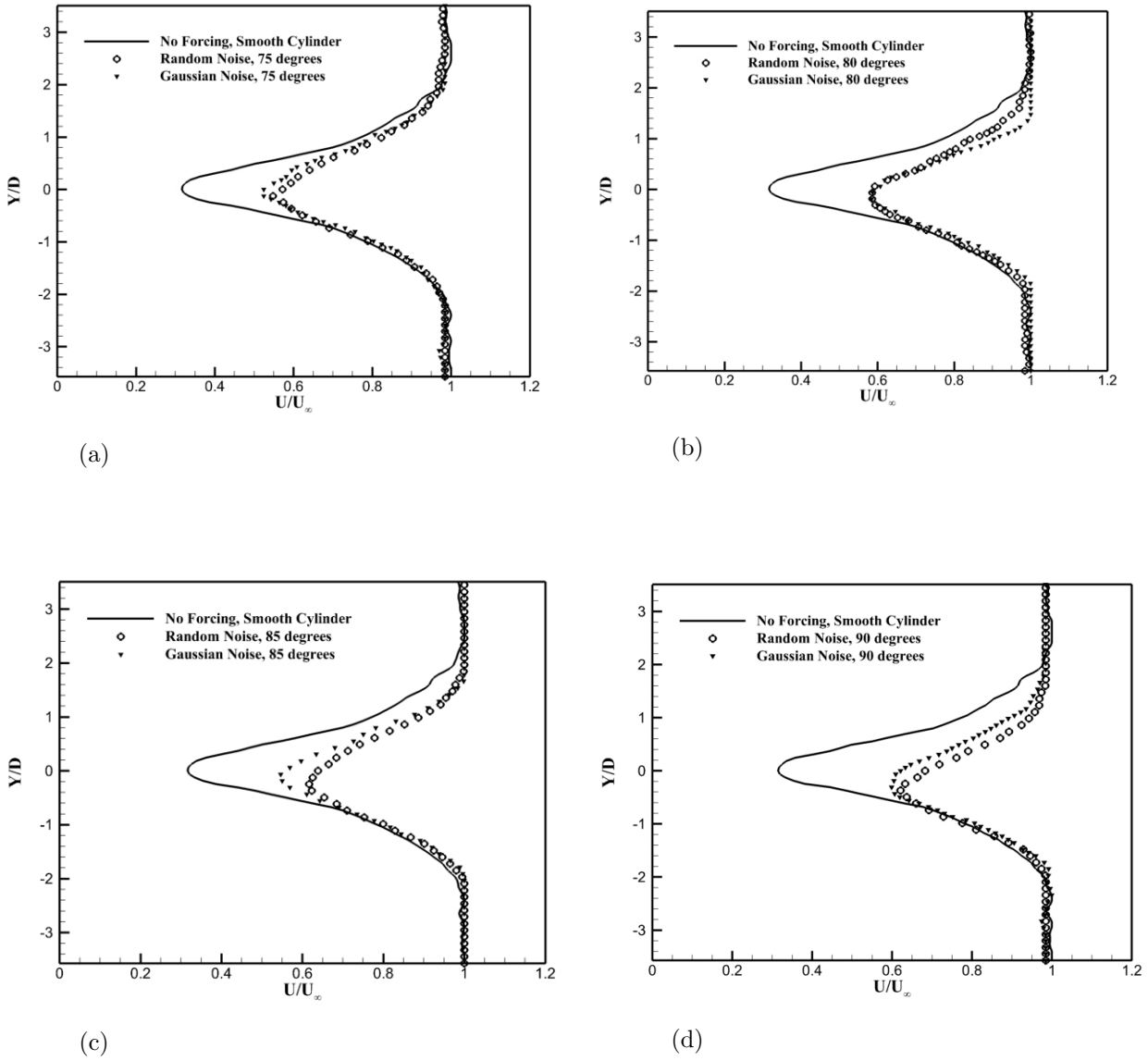


Figure 3.11: Mean velocity profiles, $\frac{X}{D} = 4$. Smooth cylinder: (a) Single slit forcing, $\phi = 75°$ , (b) Single slit forcing, $\phi = 80°$ , (c) Single slit forcing, $\phi = 85°$ , (d) Single slit forcing, $\phi = 90°$

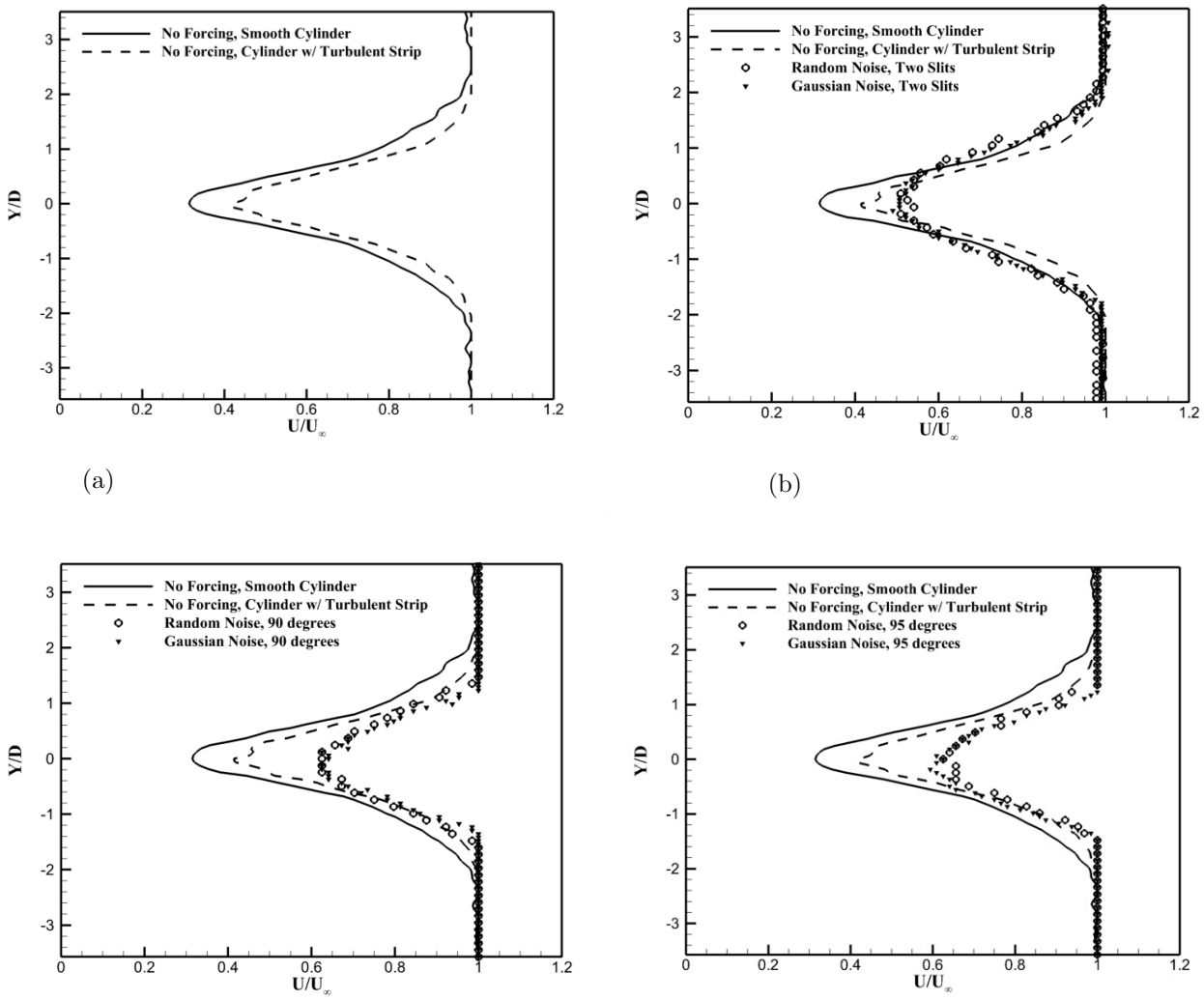


Figure 3.12: Mean velocity profiles, $\frac{X}{D} = 4$. (a) Smooth vs Tripped cylinder, Tripped cylinder: (b)Two slit forcing, (c) Single slit forcing, $\phi = 90°$ , (d) Single slit forcing, $\phi = 95°$

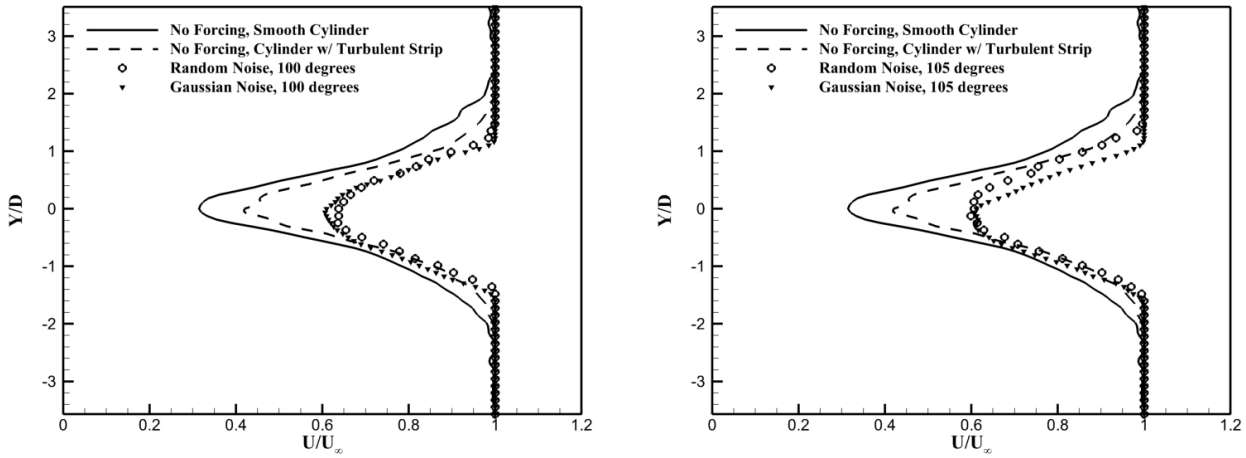


(a) (b)

Figure 3.13: Mean velocity profiles, $\frac{X}{D} = 4$. Tripped cylinder: (a) Single slit forcing, $\phi = 100°$ ,(b) Single slit forcing, $\phi = 105°$

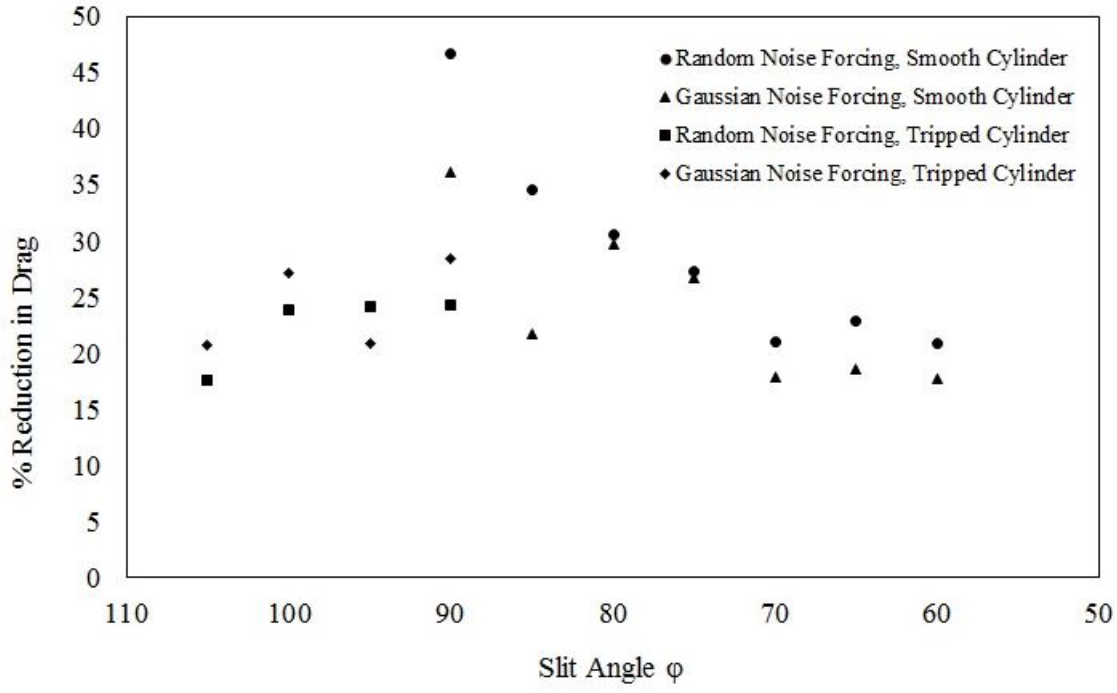


Figure 3.14: Variation in % drag reduction for single slit forcing cases

Table 3.2: Drag coefficients $C_d$, smooth cylinder, random noise forcing

| Re = 12,000 | Downstream location $X/D$ | | | | |
|---|---|---|---|---|---|
| Case | 2 | 4 | 6 | 8 | 10 |
| No forcing | 1.4122 | 1.3811 | 1.3569 | 1.3522 | 1.3687 |
| Two Slits | 1.4033 | 1.2876 | 1.2448 | 1.2440 | 1.2321 |
| $\phi = 60°$ | 1.3914 | 1.2864 | 1.2793 | 1.2542 | 1.2784 |
| $\phi = 65°$ | 1.4102 | 1.2978 | 1.2523 | 1.2236 | 1.2724 |
| $\phi = 70°$ | 1.3632 | 1.3005 | 1.2613 | 1.2946 | 1.2615 |
| $\phi = 75°$ | 1.3411 | 1.2606 | 1.2501 | 1.2713 | 1.2409 |
| $\phi = 80°$ | 1.3405 | 1.2539 | 1.2459 | 1.2416 | 1.2242 |
| $\phi = 85°$ | 1.3189 | 1.2203 | 1.2377 | 1.2319 | 1.2207 |
| $\phi = 90°$ | 1.2732 | 1.1798 | 1.1886 | 1.1788 | 1.1824 |

Table 3.3: Drag coefficients $C_d$, smooth cylinder, Gaussian noise forcing

| Re = 12,000 | Downstream location $X/D$ | | | | |
|---|---|---|---|---|---|
| Case | 2 | 4 | 6 | 8 | 10 |
| No forcing | 1.4122 | 1.3811 | 1.3569 | 1.3522 | 1.3687 |
| Two Slits | 1.4033 | 1.2876 | 1.2448 | 1.2440 | 1.2321 |
| $\phi = 60°$ | 1.3914 | 1.2864 | 1.2793 | 1.2542 | 1.2784 |
| $\phi = 65°$ | 1.4102 | 1.2978 | 1.2523 | 1.2236 | 1.2724 |
| $\phi = 70°$ | 1.3632 | 1.3005 | 1.2613 | 1.2946 | 1.2615 |
| $\phi = 75°$ | 1.3411 | 1.2606 | 1.2501 | 1.2713 | 1.2409 |
| $\phi = 80°$ | 1.3405 | 1.2539 | 1.2459 | 1.2416 | 1.2242 |
| $\phi = 85°$ | 1.3189 | 1.2203 | 1.2377 | 1.2319 | 1.2207 |
| $\phi = 90°$ | 1.2732 | 1.1798 | 1.1886 | 1.1788 | 1.1824 |

Table 3.4: Drag coefficients $C_d$, tripped cylinder, random noise forcing

| Re = 12,000 | Downstream location $X/D$ | | | | |
|---|---|---|---|---|---|
| Case | 2 | 4 | 6 | 8 | 10 |
| No forcing | 1.4122 | 1.3811 | 1.3569 | 1.3522 | 1.3687 |
| No forcing with strip | 1.4172 | 1.3051 | 1.2683 | 1.2911 | 1.2596 |
| Two Slits | 1.4543 | 1.3554 | 1.3151 | 1.3029 | 1.2988 |
| $\phi = 90°$ | 1.3804 | 1.2803 | 1.2527 | 1.2633 | 1.2467 |
| $\phi = 95°$ | 1.3087 | 1.2751 | 1.2590 | 1.2664 | 1.2467 |
| $\phi = 100°$ | 1.3773 | 1.2942 | 1.2443 | 1.2627 | 1.2542 |
| $\phi = 105°$ | 1.4268 | 1.3118 | 1.2818 | 1.2751 | 1.2561 |

Table 3.5: Drag coefficients $C_d$, tripped cylinder, Gaussian noise forcing

| Re = 12,000 | Downstream location $X/D$ | | | | |
|---|---|---|---|---|---|
| Case | 2 | 4 | 6 | 8 | 10 |
| No forcing | 1.4122 | 1.3811 | 1.3569 | 1.3522 | 1.3687 |
| No forcing with strip | 1.4172 | 1.3051 | 1.2683 | 1.2911 | 1.2596 |
| Two Slits | 1.4183 | 1.3503 | 1.2366 | 1.2365 | 1.2644 |
| $\phi = 90°$ | 1.3957 | 1.2341 | 1.2523 | 1.2341 | 1.2327 |
| $\phi = 95°$ | 1.4419 | 1.2918 | 1.2787 | 1.2403 | 1.2413 |
| $\phi = 100°$ | 1.4286 | 1.2996 | 1.2594 | 1.2412 | 1.2569 |
| $\phi = 105°$ | 1.4081 | 1.2868 | 1.2653 | 1.2693 | 1.2627 |

### 3.3 Spectral Analysis of the Wake

The hot wire probe was placed at a location of $\frac{y}{D} = 1.4$ and $\frac{x}{D} = 4$, which was the optimal position for measuring power spectra in the upper shear layer and was monitored by analyzing the power spectra processed at every point traversed in the wake of the cylinder in real time with a Hewlett Packard spectrum analyzer.

Figure 3.15 illustrates the effect of random noise forcing on the smooth cylinder as observed from the upper shear layer. The shear layer spectra taken for no forcing case (plotted in the same figure) shows a sharp peak at 23 Hz, which corresponds to the fundamental frequency $f_s$ of von Kármán vortices in the wake. Two slit forcing showed complete elimination of vortex shedding peak. This was also the case as seen for random noise forcing at $\phi = 90°$ . Single slit forcing from $\phi = 60°$ to $\phi = 85°$ show that, with increase of $\phi$ , the effectiveness of noise forcing increased. In Figure 3.15, the shear spectra at lower angles of $\phi$ indicate the presence of smaller strength vortices caused by the breakdown of vortex shedding in the wake.

Figure 3.16 shows the effect of Gaussian noise in the shear layer of the wake. It was observed that Gaussian noise forcing was not as effective in suppressing vortex shedding in the wake. However, two slit forcing using Gaussian noise showed complete elimination of vortex shedding peak. Single slit forcing at $\phi = 60°$ showed that the magnitude of shedding peak was reduced by the action of Gaussian noise on vortex shedding. This lead to partial

breakdown of vortex shedding, causing smaller strength vortices being advected in the wake and shear layer, as seen from the power spectra. The magnitude of smaller strength vortices slowly decreased as $\phi$ was increased, indicating increased effect of noise forcing, until showing complete suppression of shedding peak at $\phi = 90^\circ$ .

In Figure 3.17, the shear spectra for the tripped cylinder are shown. At first, the inclusion of trip strip caused increase in magnitude of the 23 Hz shedding peak, which indicated that although the turbulent strip was effective in reducing drag behind the cylinder by delaying separation, there were vortices of higher energy shed in the wake. Because of the turbulent boundary layer, a delay of separation from $90^\circ$ to about $100^\circ$ was observed.

In general, noise forcing was not as effective in the case of tripped cylinder. In Figures 3.17 and 3.18, it was observed that two slit forcing was successful in suppressing vortex shedding, although resulting in the expansion of the immediate wake behind the cylinder. At $\phi = 90^\circ$ , the effect of both random and Gaussian noise forcing were different than in the case of smooth cylinder. The shear spectra showed that the action of noise forcing resulted in partial suppression of vortex shedding. This caused smaller strength vortices to be advected into the shear layer, having slightly higher energy when compared to the case of smooth cylinder. It was shown that Gaussian noise forcing had more effect in this regime than random noise forcing. At $\phi = 100^\circ$ , Gaussian noise forcing resulted in further suppression of vortex shedding than random noise forcing.

The manner in which Gaussian noise forcing proved effective compared to random noise forcing in the case of tripped cylinder wake may be explained by taking into account the following example. Consider four time series random signals, two having separate uniform distributions (white noise or random noise) and the other two having separate Gaussian distributions. Spectral coherence was deduced from these time series signals using MATLAB of frequencies present by comparing time signals. It was observed that cross-correlation of two random noise signals (Figure 3.19) and that of random and Gaussian signals (Figure 3.20) had lower coherence of frequencies than that of the two Gaussian signals (Figure 3.21). The

statistical models used to describe turbulence suggest a Gaussian distribution of turbulent quantities. Since the tripped cylinder contained fully turbulent flow in the wake, it was assumed that the wake had a Gaussian distribution of turbulence. This allowed increased coherence of Gaussian noise forcing with the turbulent quantities present in the wake, which proved more effective than random noise forcing.

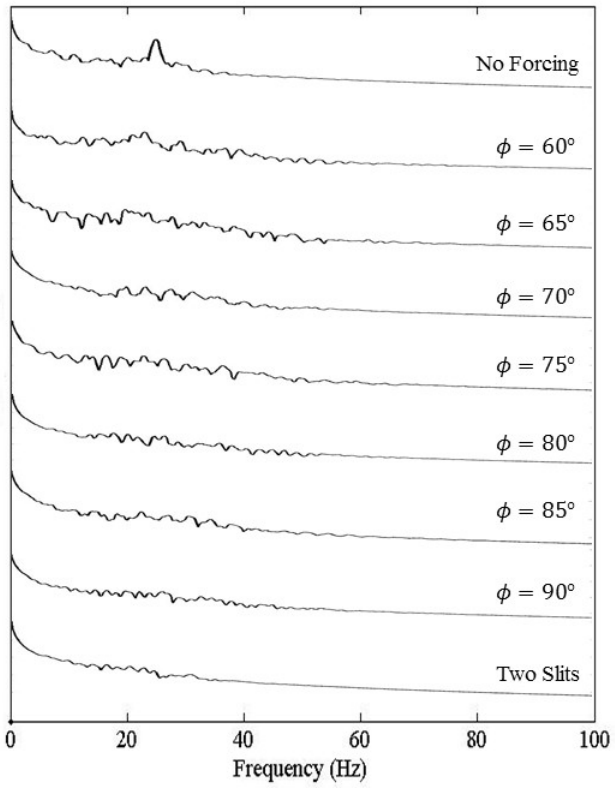


Figure 3.15: Shear layer spectra, random noise forcing

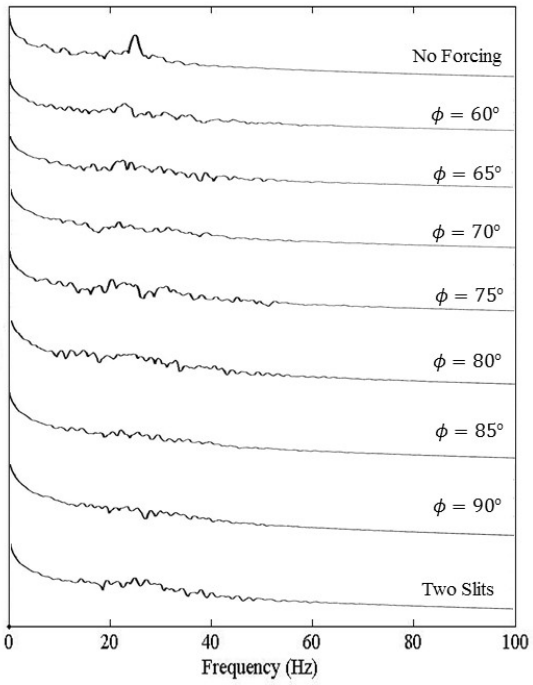


Figure 3.16: Shear layer spectra, Gaussian noise forcing

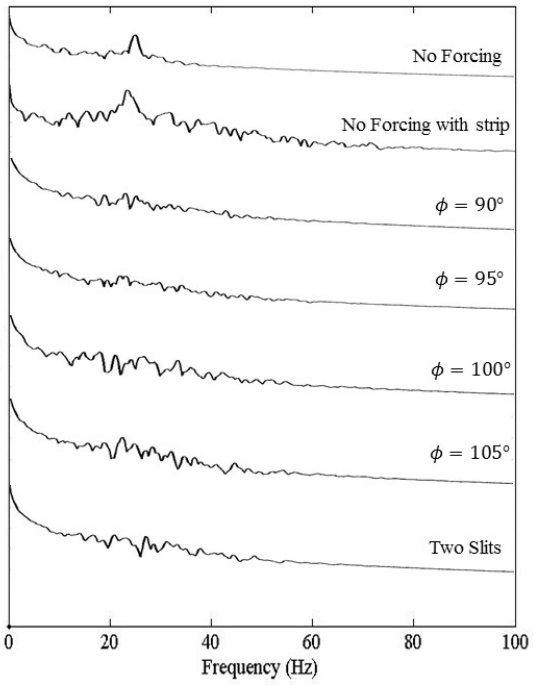


Figure 3.17: Shear layer spectra, cylinder with tripped boundary layer , random noise forcing

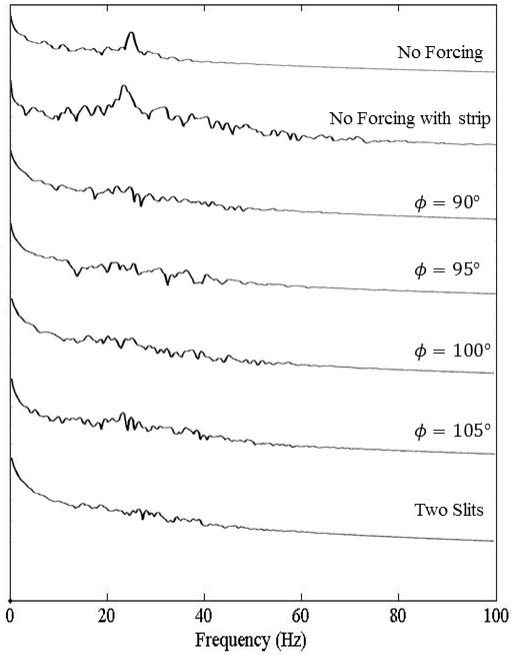


Figure 3.18: Shear layer spectra, cylinder with tripped boundary layer, Gaussian noise forcing

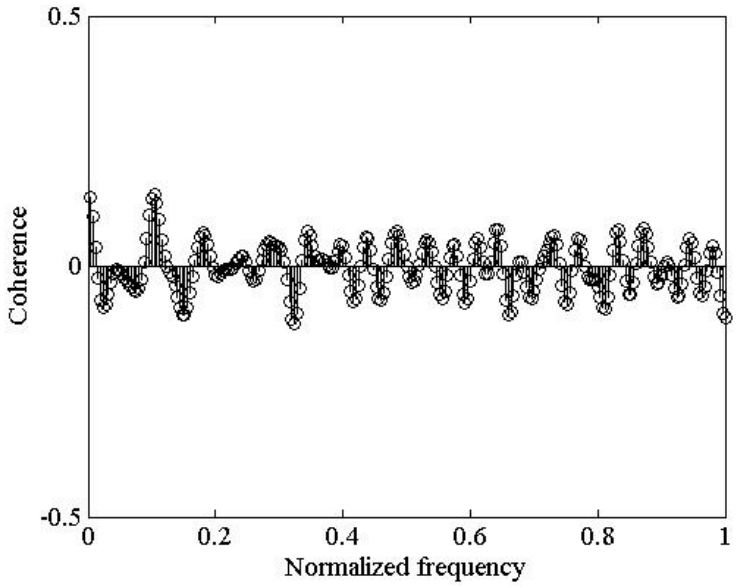


Figure 3.19: Cross-correlation between two separate random signals

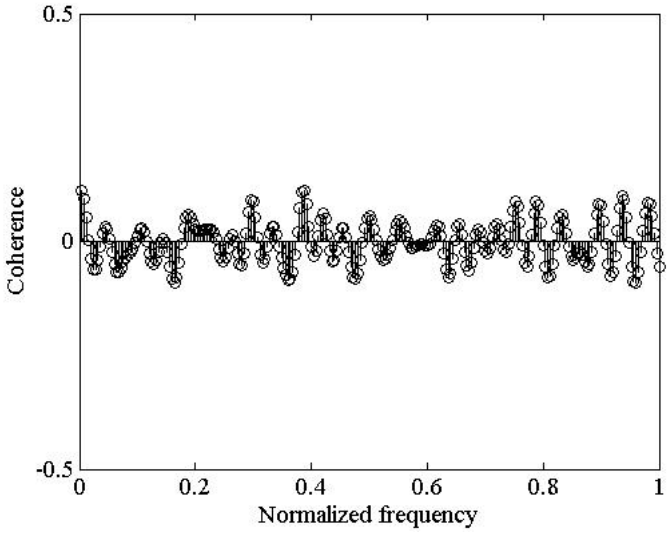


Figure 3.20: Cross-correlation between random signal and Gaussian signal

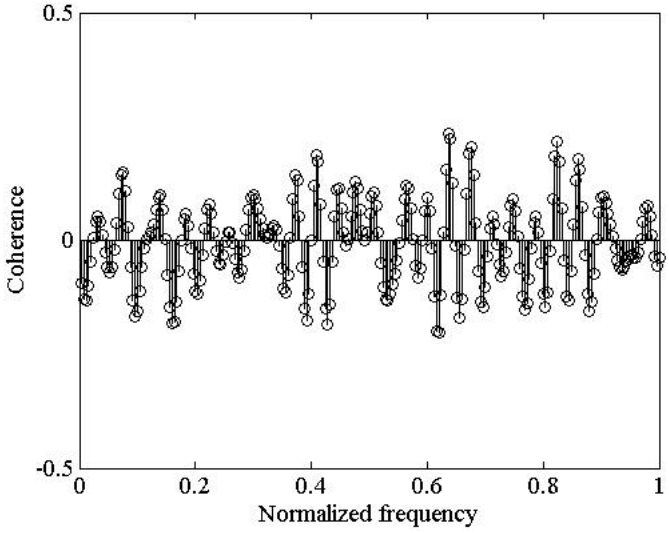


Figure 3.21: Cross-correlation between two separate Gaussian signals

### 3.4 Perturbation velocity and Turbulence intensity

Perturbation velocity was calculated by taking instantaneous velocity samples and using Reynolds decomposition of velocity. The root-mean-square of standard deviation was calculated to obtain $u^{'}$.

$$u^{'} = \sqrt{\frac{1}{N-1}\sum_{1}^{N}(u-\overline{u})^2}$$

where $u$ represents the instantaneous velocity and $\overline{u}$ represents the mean velocity, $N$ represents total number of samples.

Plots of perturbation velocity $u^{'}$ across the wake showed the variation of perturbation velocity in the wake with that of the freestream. It was observed that the magnitude of perturbation velocity was higher in the near wake of the cylinder due to the interaction of vortex shedding and separating shear layers. Figures 3.44 and 3.45 show that the inclusion of turbulent strip increased the magnitude of $u^{'}$ across the entire wake.

For all the forcing cases, with reference to both the smooth cylinder and cylinder fitted with trip strip, a shift in perturbation velocity was observed. In general, the perturbation velocity in the near wake of the cylinder was shown to decrease due to the interaction between the vortices ejected from noise forcing and the vortex shedding in the wake. Further downstream, the magnitude of perturbations dissipated much quicker compared to the no forcing case, which suggested breakdown of vortex shedding in the far wake. It was also observed that single slit forcing caused asymmetry in perturbation velocity across the wake.

Contours of turbulence intensity $Tu = u'/U_\infty$ were also acquired from hot wire data (see Appendix). Higher levels of turbulence intensity existed at areas of maximum shear, immediately behind the cylinder. Downstream in the wake, turbulence intensity dissipated owing to the interaction of von Kármán vortices with the freestream flow. The tripped cylinder was found to have increased values of $Tu$ due to action of increased levels of turbulence caused by turbulent boundary layer. Two slit forcing resulted in a symmetric decrease of $Tu$ in the immediate and near wakes. Single slit forcing caused an asymmetrical variation

of the turbulence intensities. The top shear layer resulted in increased momentum, causing subsequent decrease in $Tu$. As $\phi$ neared the point of boundary layer separation, $Tu$ showed maximum reduction over the top shear layer.

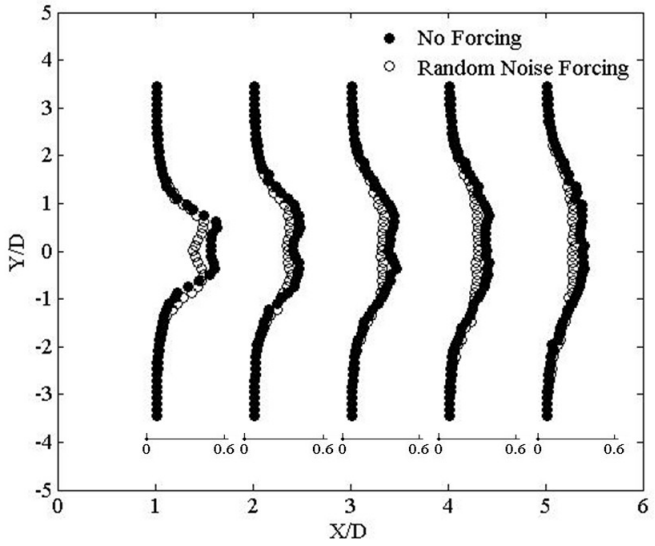


(a) Immediate Wake

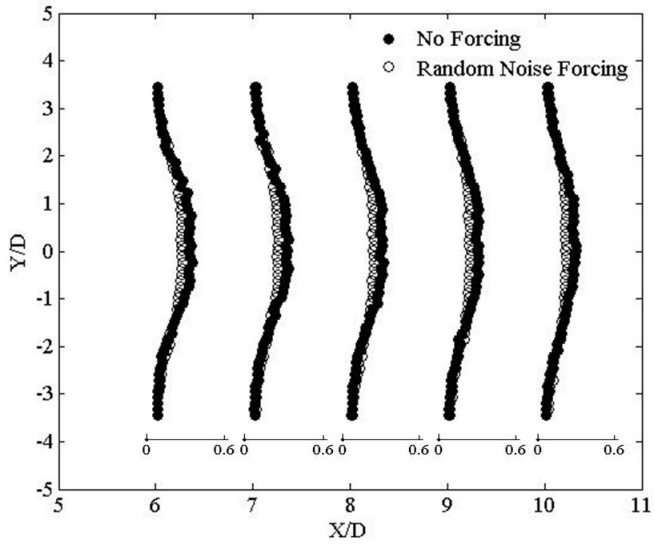


(b) Near Wake

Figure 3.22: Plots of perturbation velocity $u^{'}$, random noise forcing, two slits

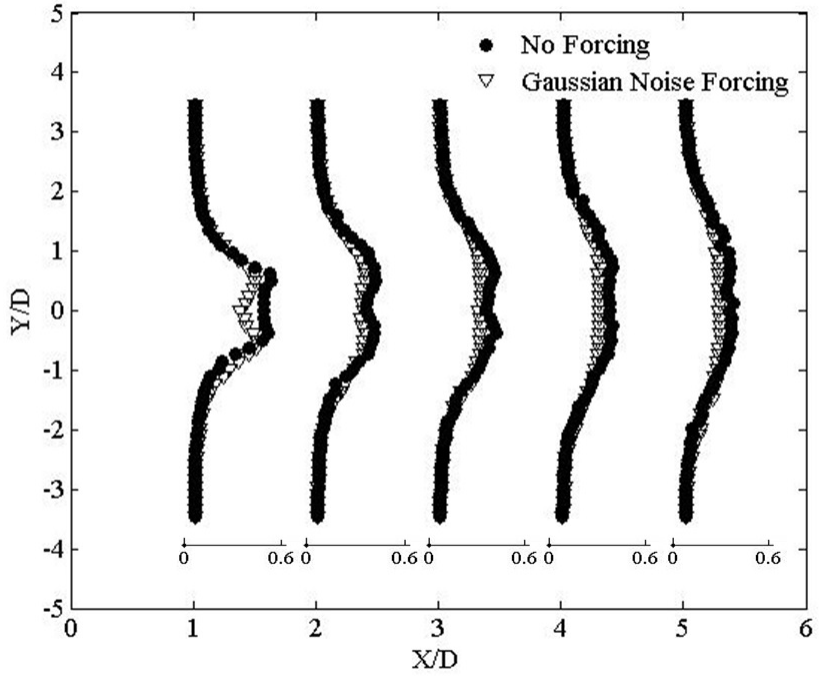


(a) Immediate Wake

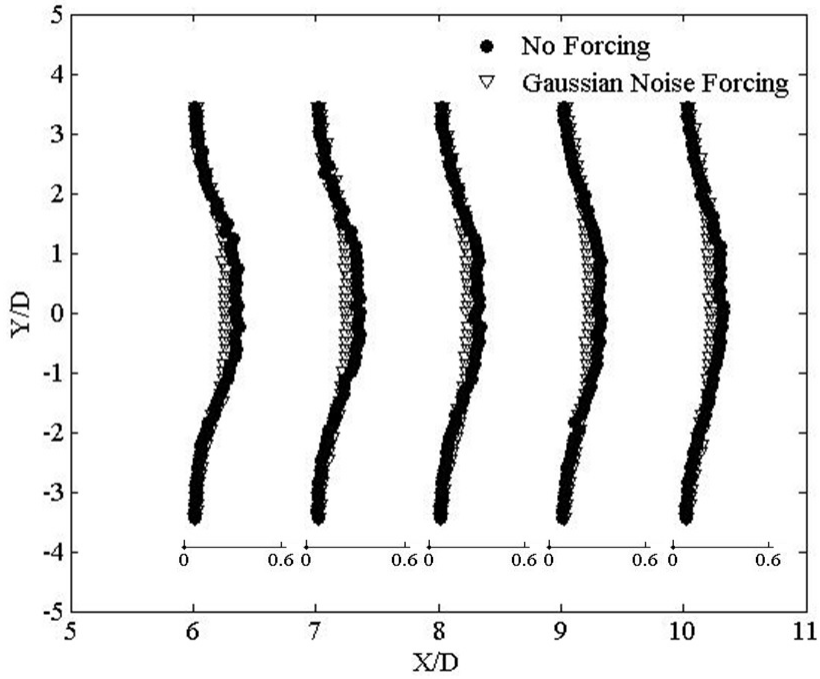


(b) Near Wake

Figure 3.23: Plots of perturbation velocity $u^{'}$, Gaussian noise forcing, two slits

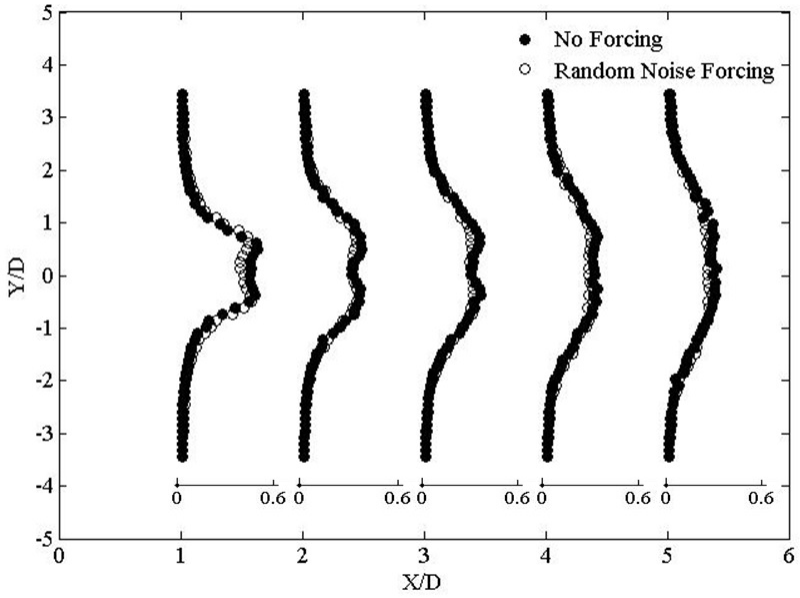


(a) Immediate Wake

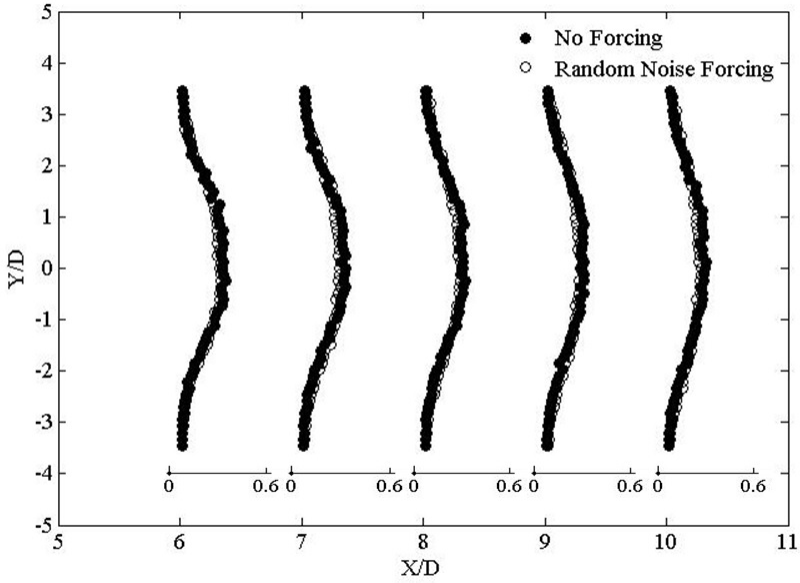


(b) Near Wake

Figure 3.24: Plots of perturbation velocity $u^{'}$, random noise forcing, single slit, $\phi = 60°$

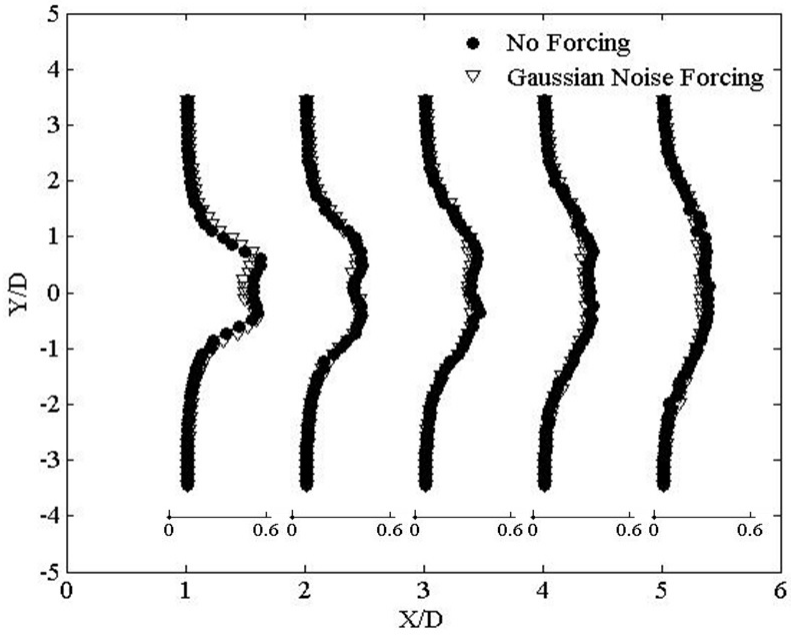


(a) Immediate Wake

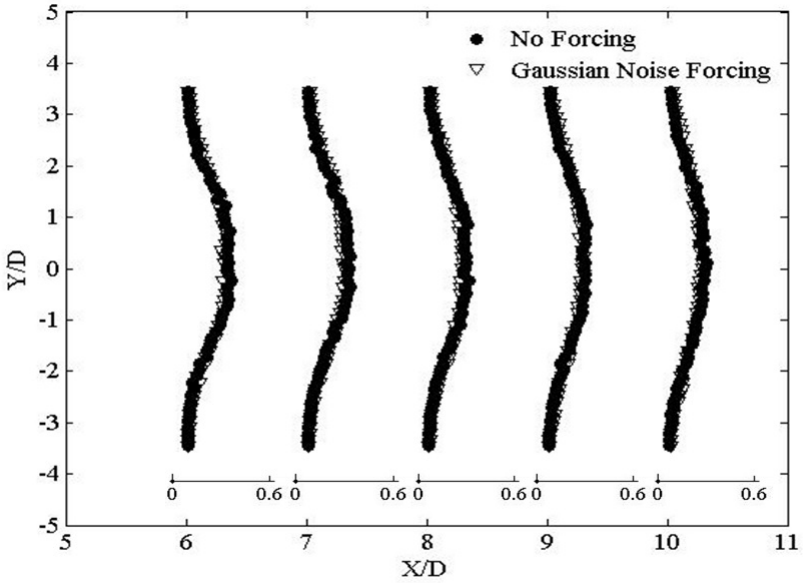


(b) Near Wake

Figure 3.25: Plots of perturbation velocity $u^{'}$, Gaussian noise forcing, single slit, $\phi = 60°$

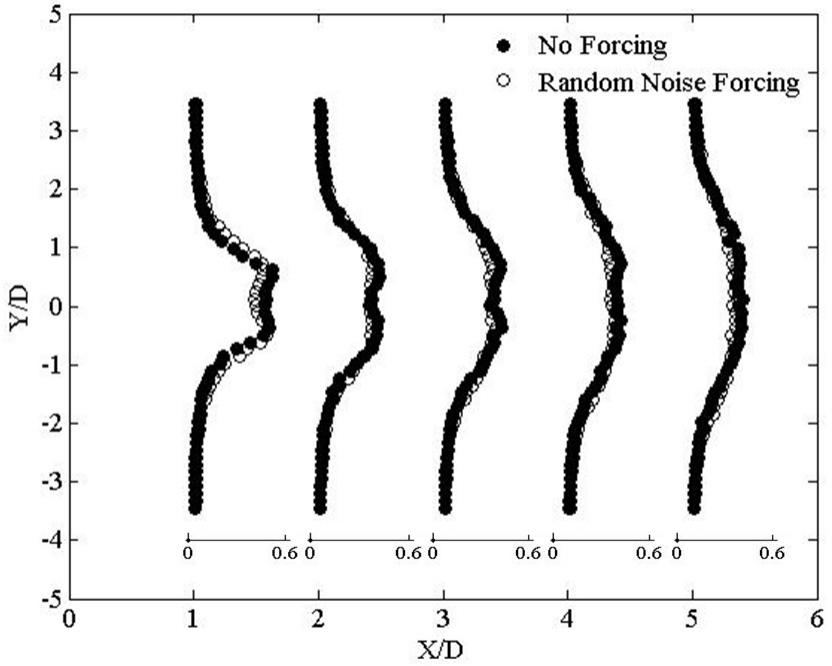


(a) Immediate Wake

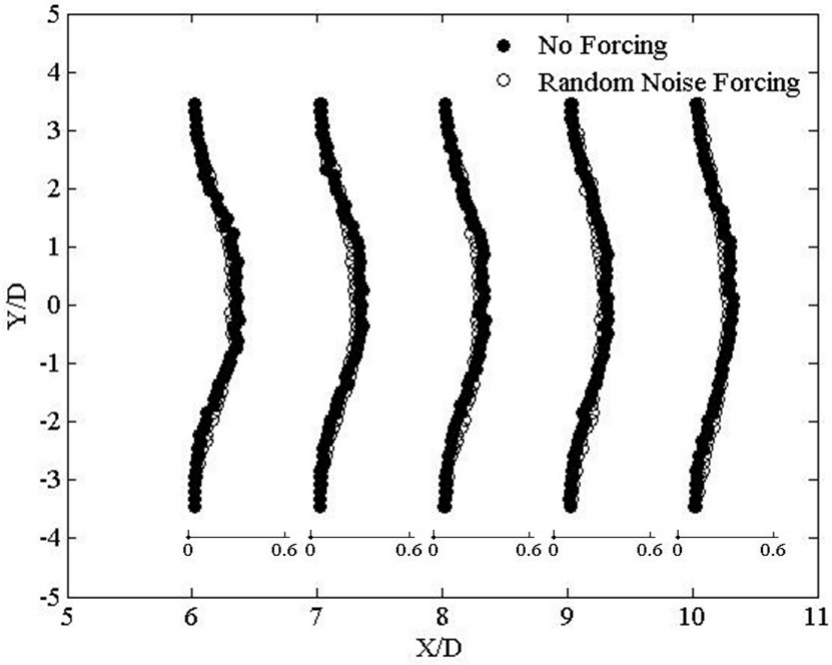


(b) Near Wake

Figure 3.26: Plots of perturbation velocity $u'$, random noise forcing, single slit, $\phi = 65°$

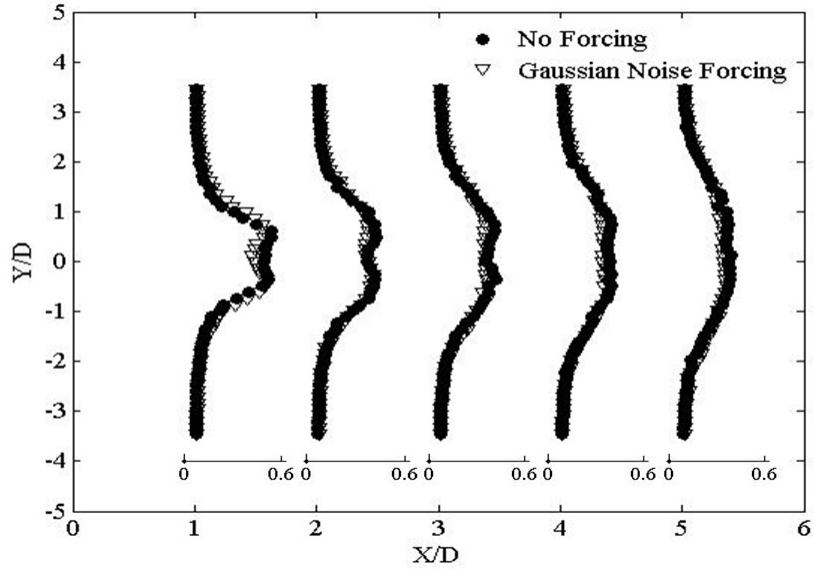


(a) Immediate Wake

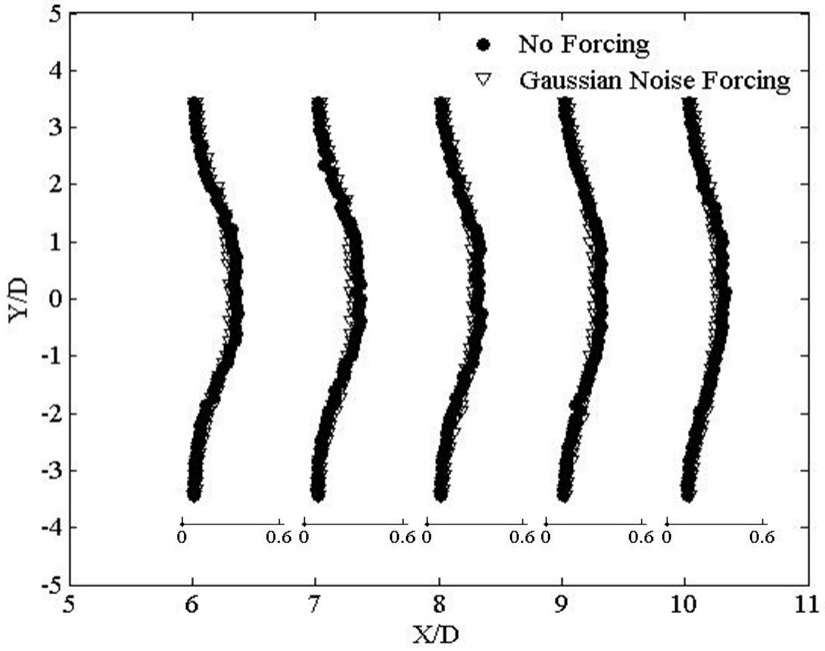


(b) Near Wake

Figure 3.27: Plots of perturbation velocity $u^{'}$, Gaussian noise forcing, singe slit, $\phi = 65^{\circ}$

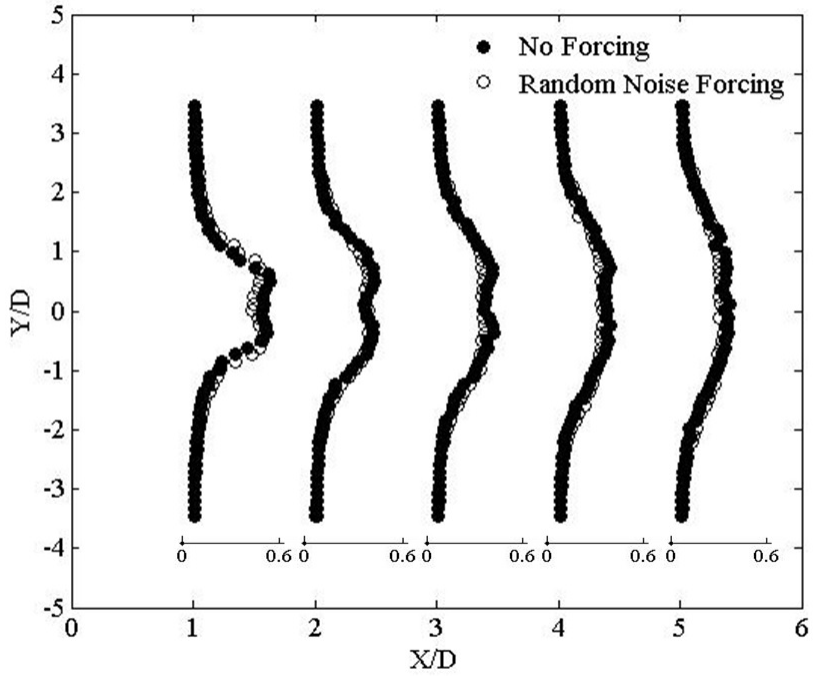


(a) Immediate Wake

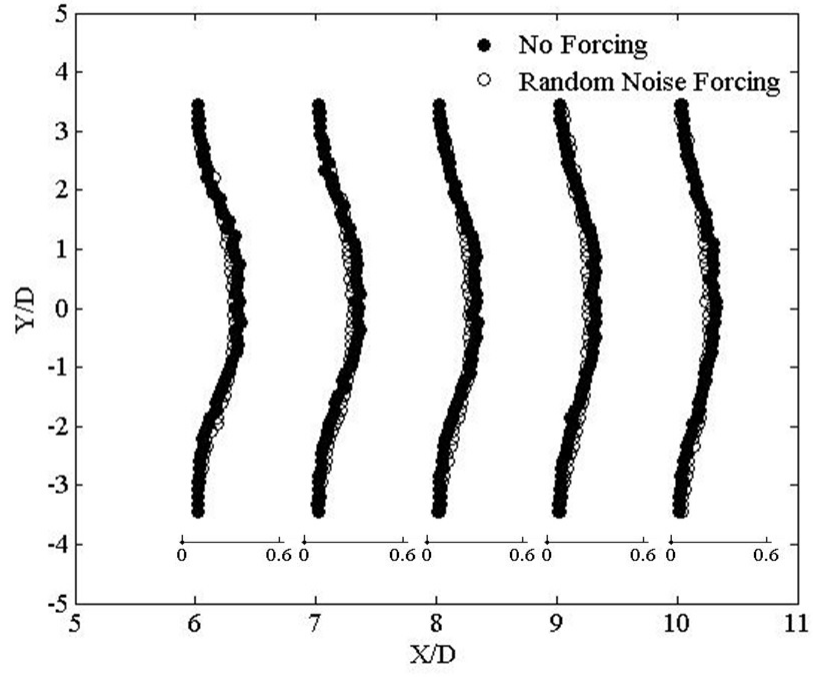


(b) Near Wake

Figure 3.28: Plots of perturbation velocity $u^{'}$, random noise forcing, single slit, $\phi = 70°$

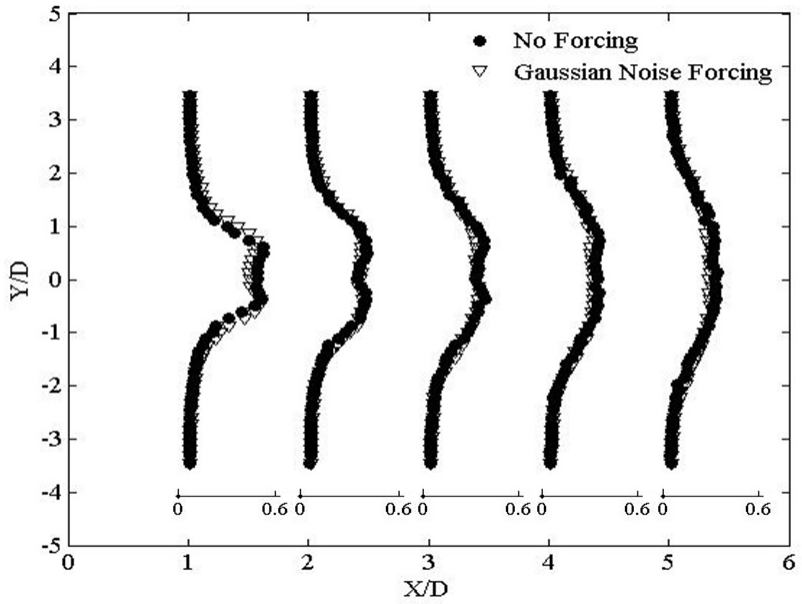


(a) Immediate Wake

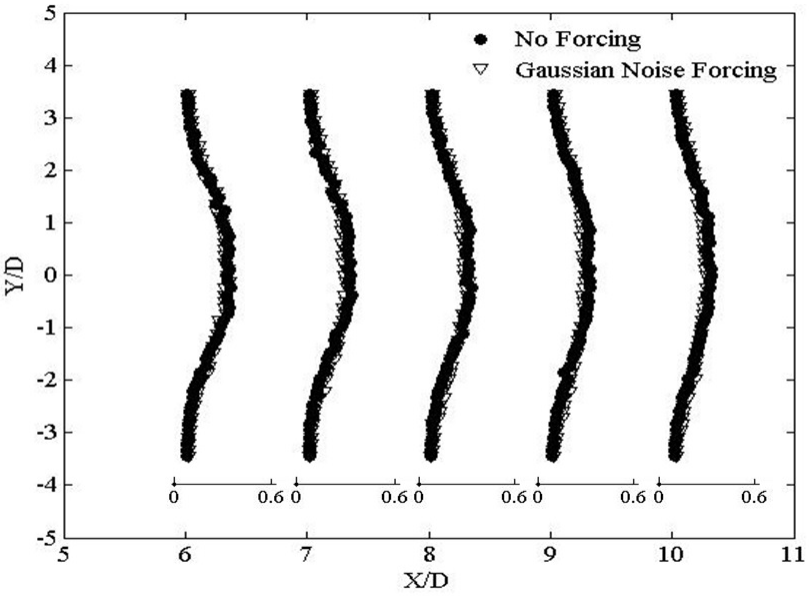


(b) Near Wake

Figure 3.29: Plots of perturbation velocity $u^{'}$, Gaussian noise forcing, single slit, $\phi = 70°$

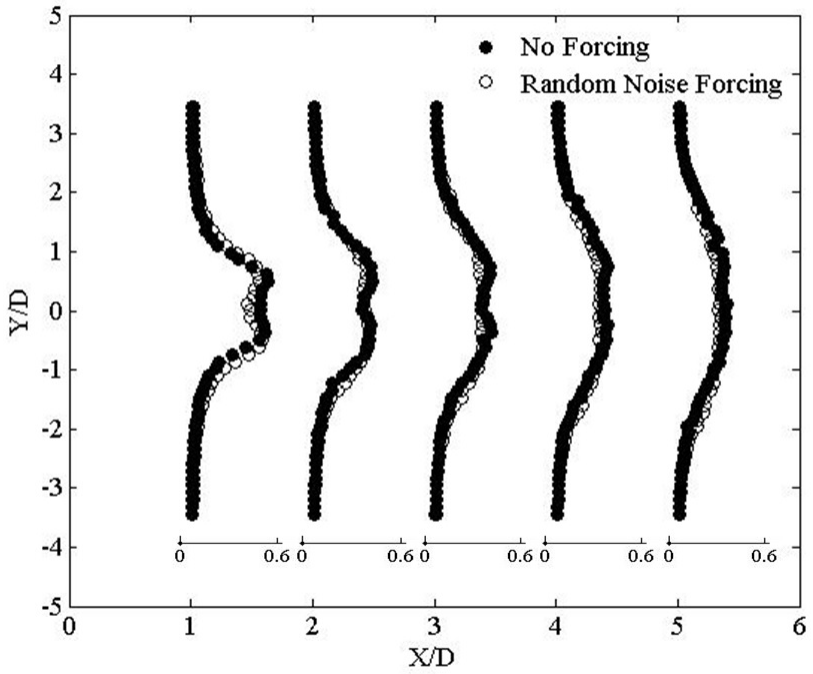


(a) Immediate Wake

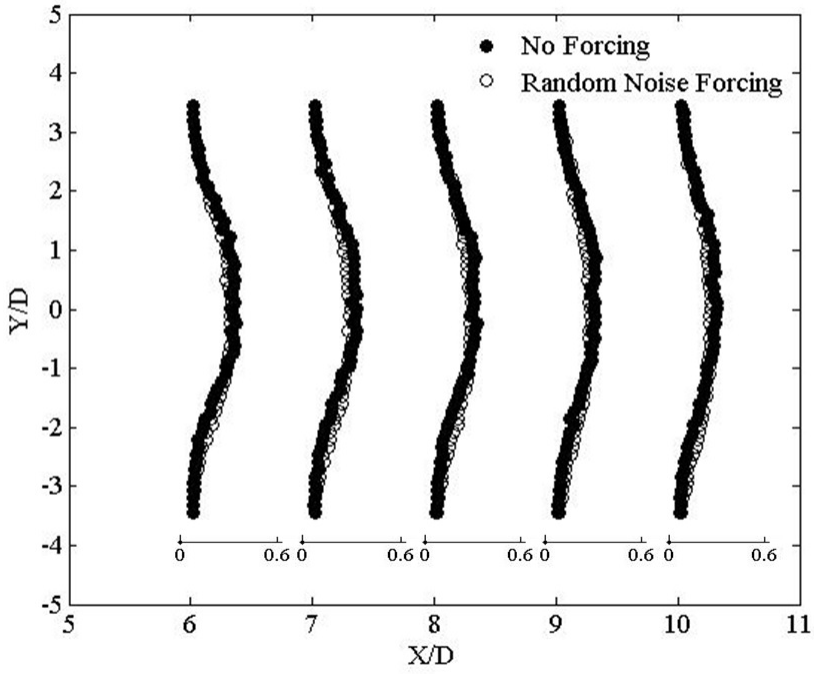


(b) Near Wake

Figure 3.30: Plots of perturbation velocity $u^{'}$, random noise forcing, single slit, $\phi = 75°$

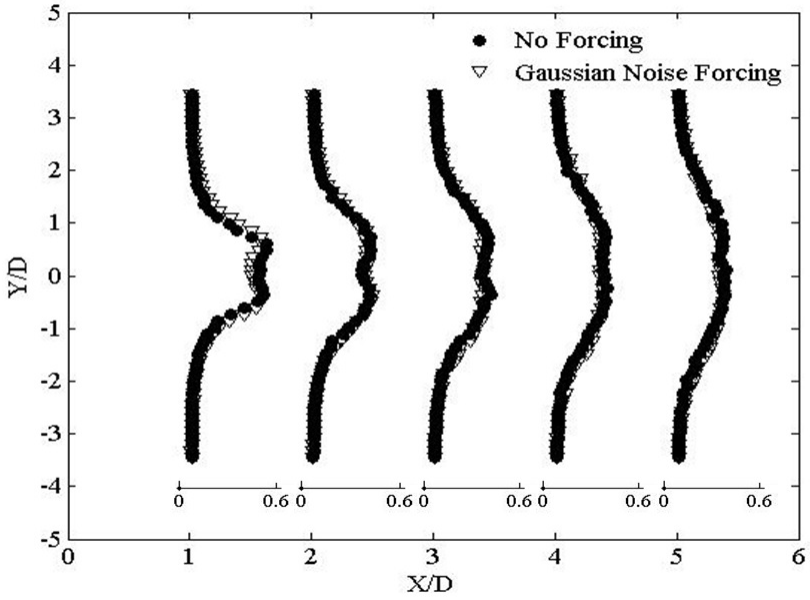


(a) Immediate Wake

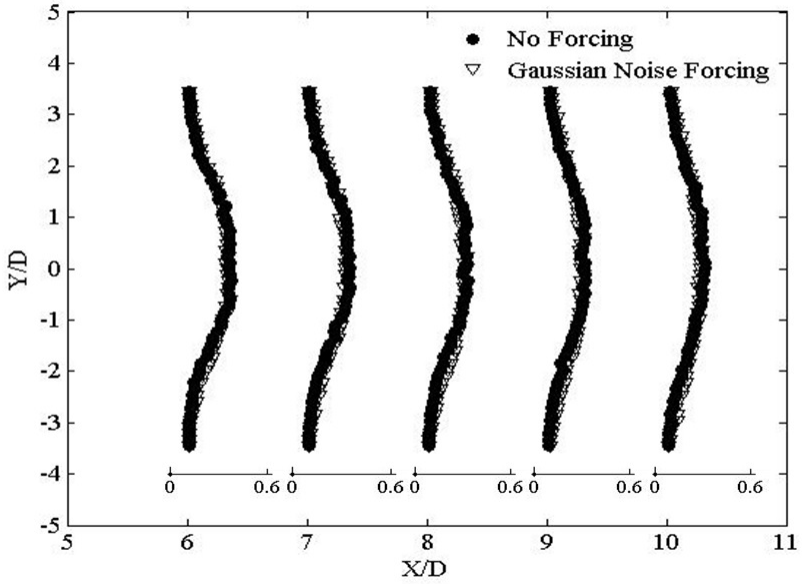


(b) Near Wake

Figure 3.31: Plots of perturbation velocity $u^{'}$, Gaussian noise forcing, single slit, $\phi = 75°$

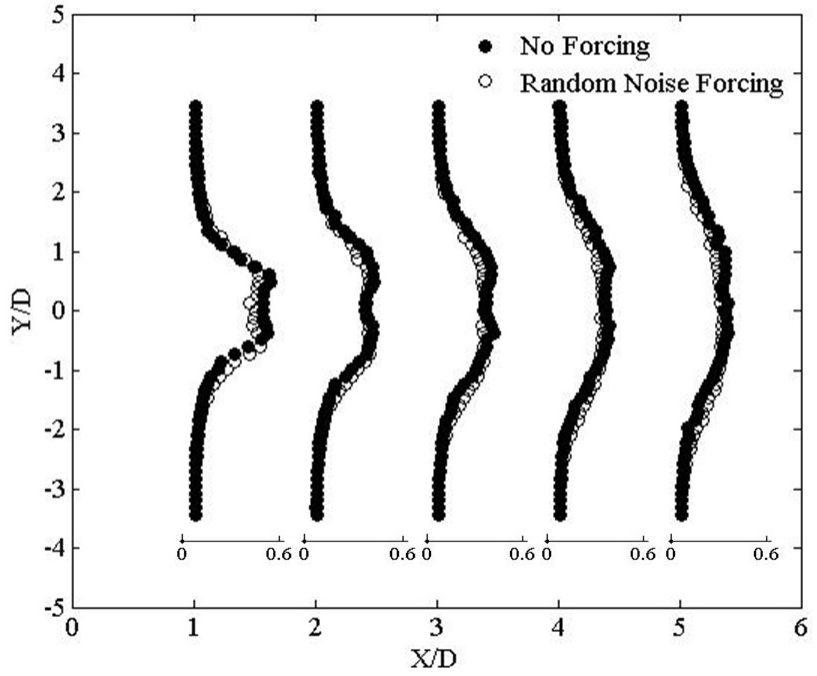


(a) Immediate Wake

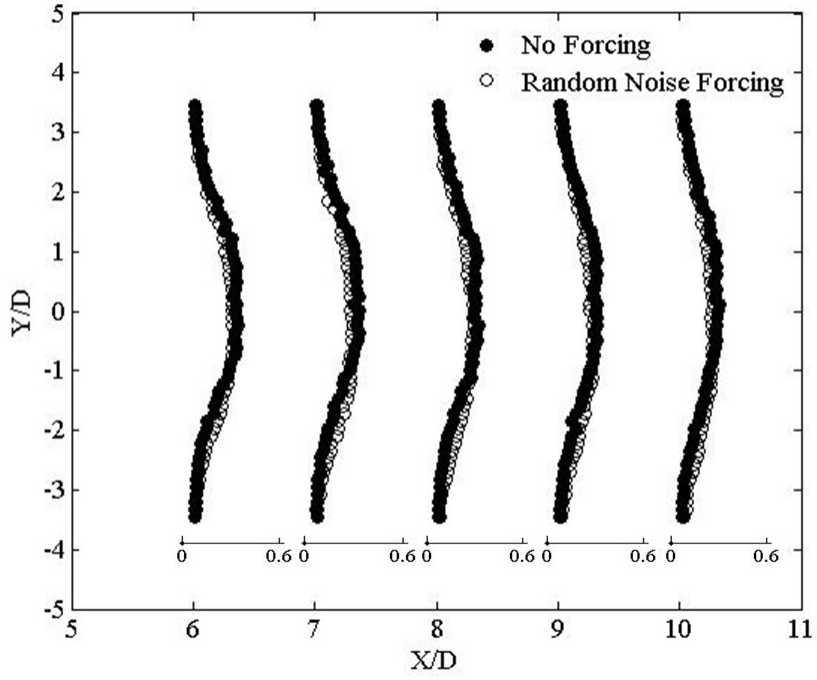


(b) Near Wake

Figure 3.32: Plots of perturbation velocity $u^{'}$, random noise forcing, single slit, $\phi = 80°$

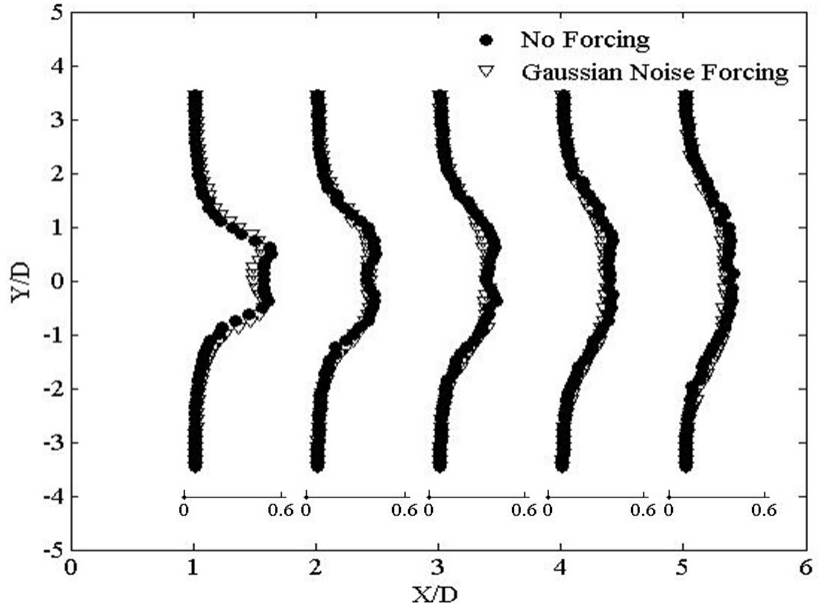


(a) Immediate Wake

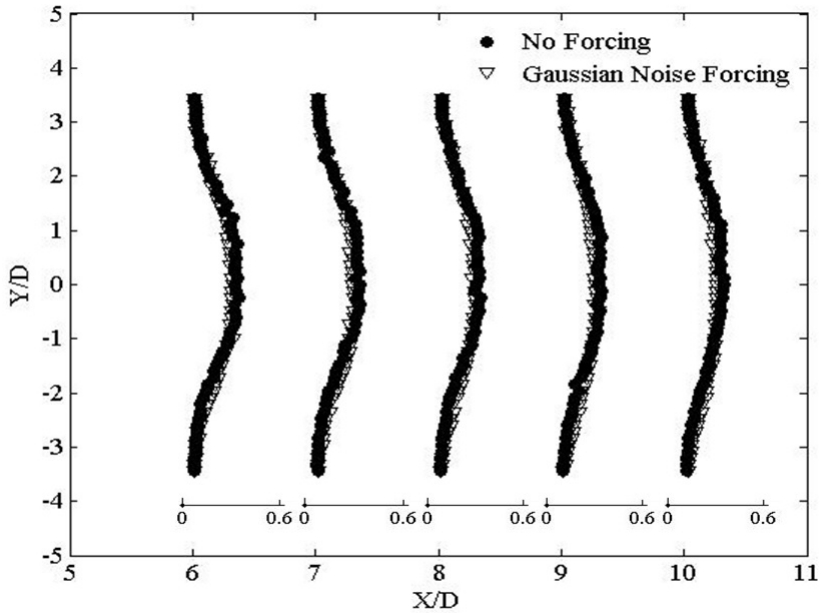


(b) Near Wake

Figure 3.33: Plots of perturbation velocity $u^{'}$, Gaussian noise forcing, single slit, $\phi = 80°$

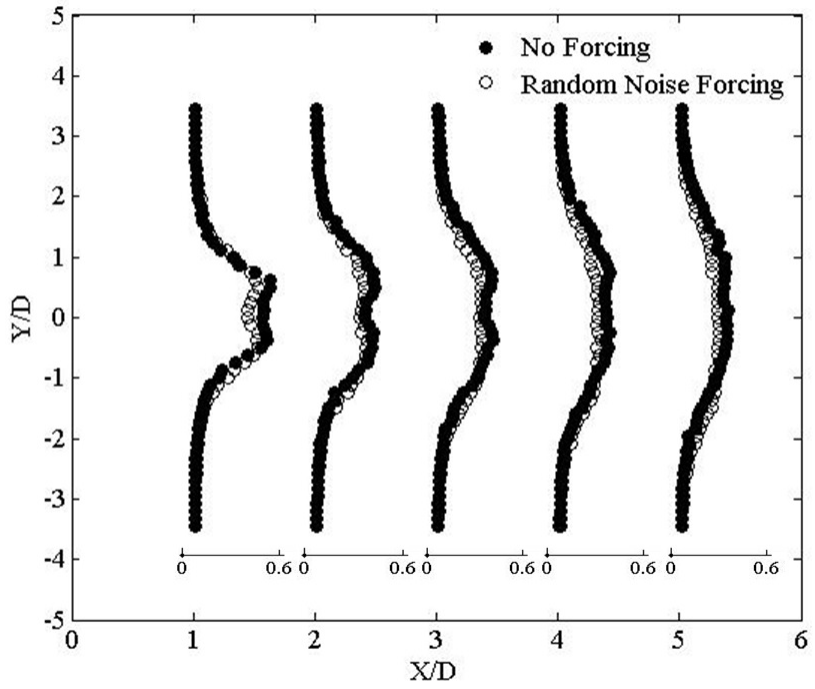


(a) Immediate Wake

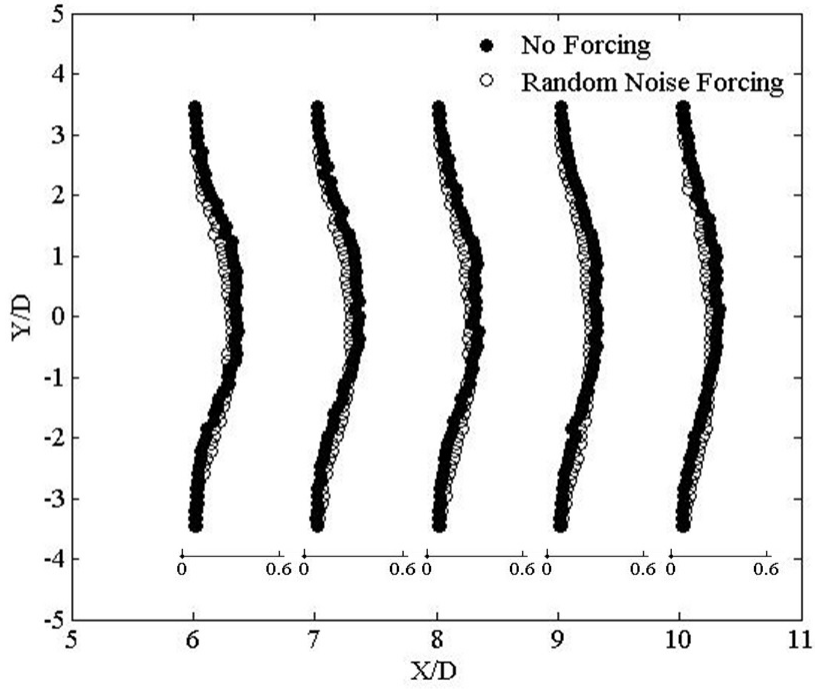


(b) Near Wake

Figure 3.34: Plots of perturbation velocity $u^{'}$, random noise forcing, single slit, $\phi = 85°$

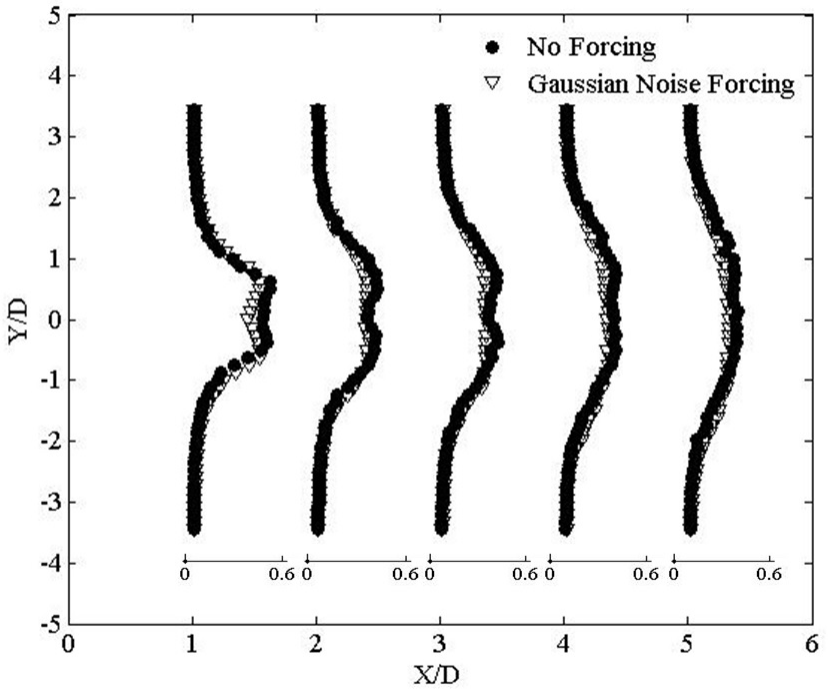


(a) Immediate Wake

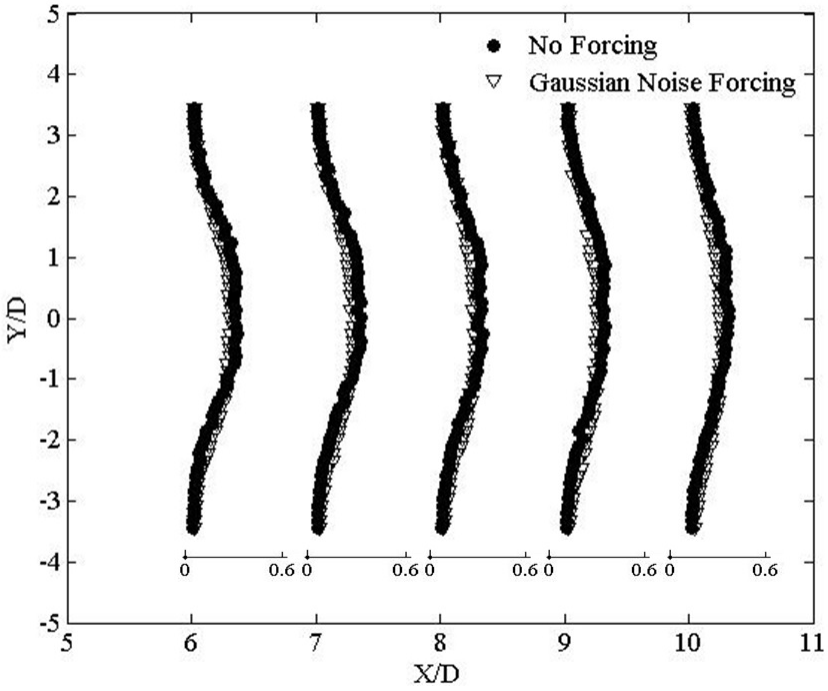


(b) Near Wake

Figure 3.35: Plots of perturbation velocity $u^{'}$, Gaussian noise forcing, single slit, $\phi = 85°$

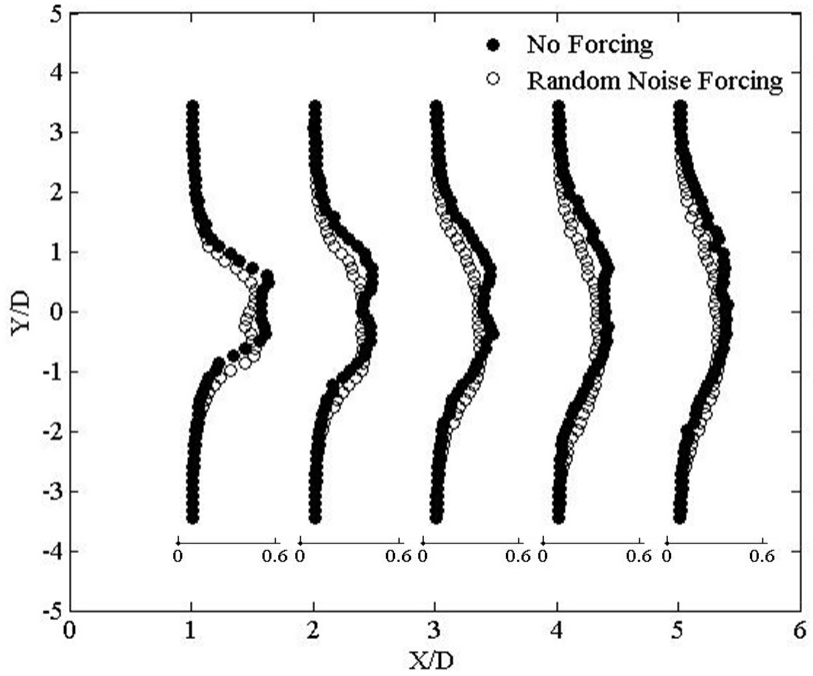


(a) Immediate Wake

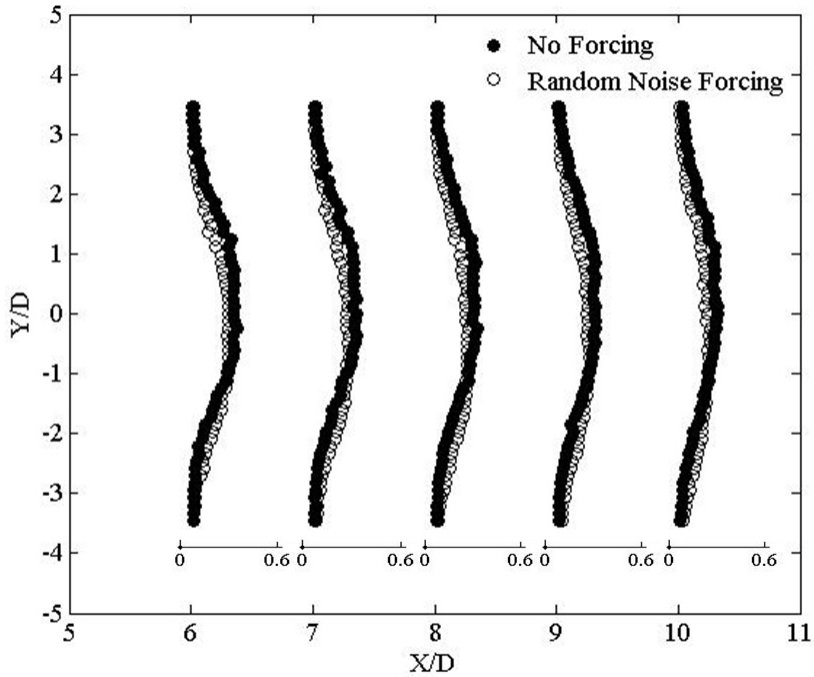


(b) Near Wake

Figure 3.36: Plots of perturbation velocity $u^{'}$, random noise forcing, single slit, $\phi = 90°$

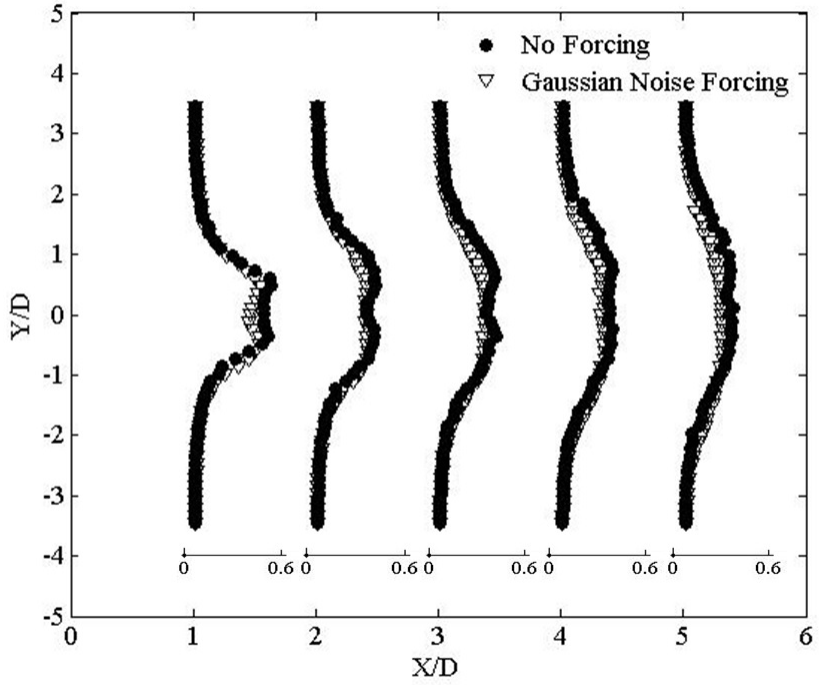


(a) Immediate Wake

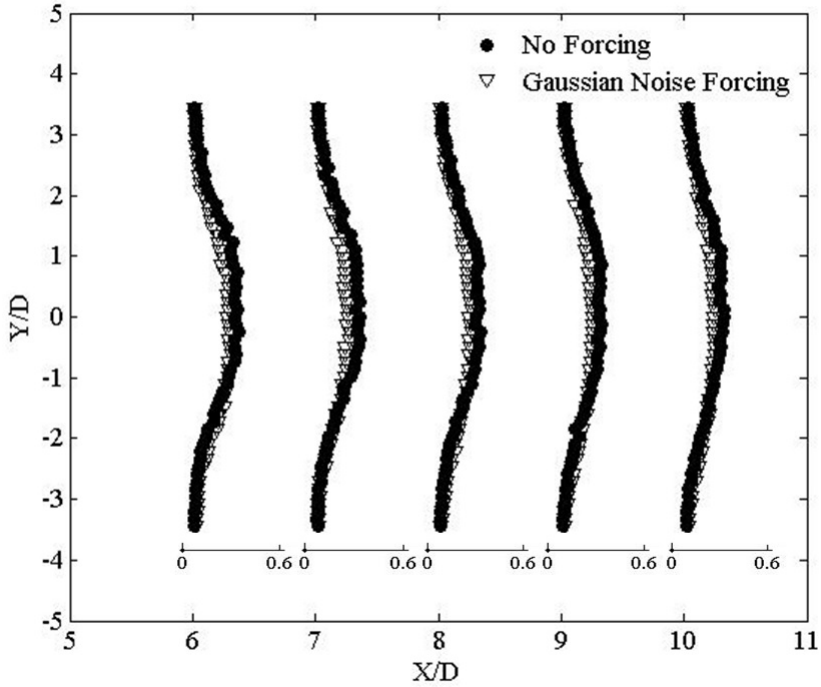


(b) Near Wake

Figure 3.37: Plots of perturbation velocity $u^{'}$, Gaussian noise forcing, single slit, $\phi = 90°$

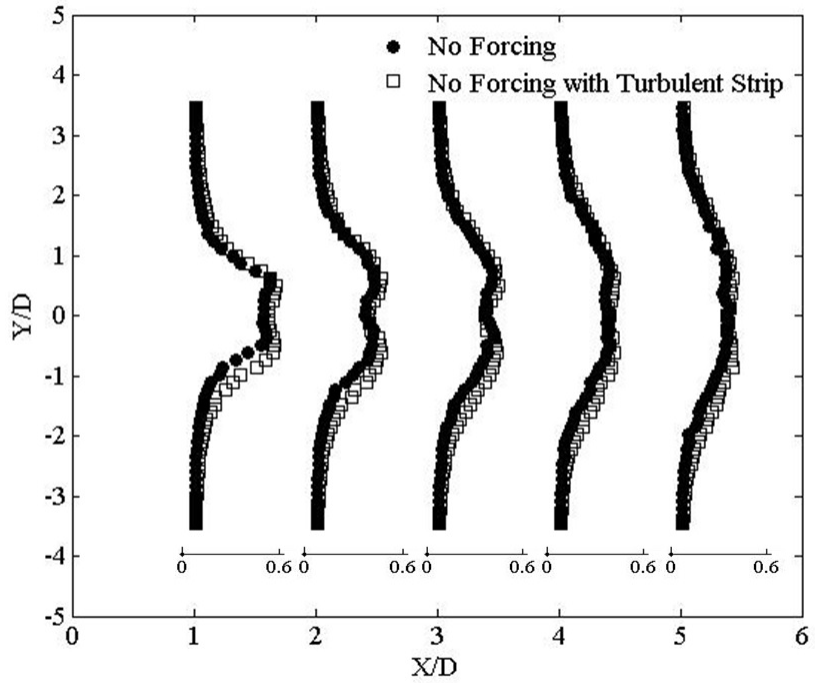


(a) Immediate Wake

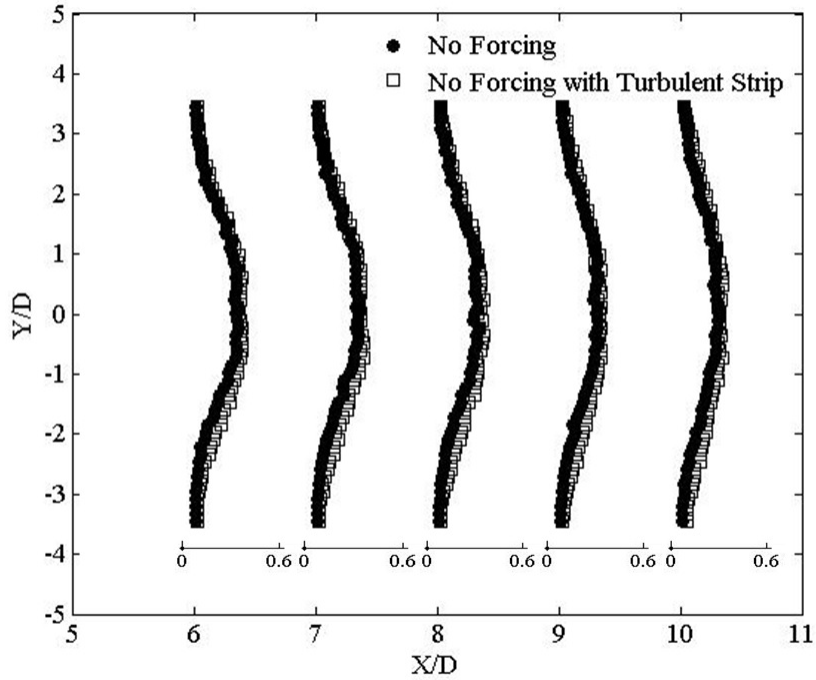


(b) Near Wake

Figure 3.38: Plots of perturbation velocity $u^{'}$, smooth cylinder vs tripped cylinder, no forcing

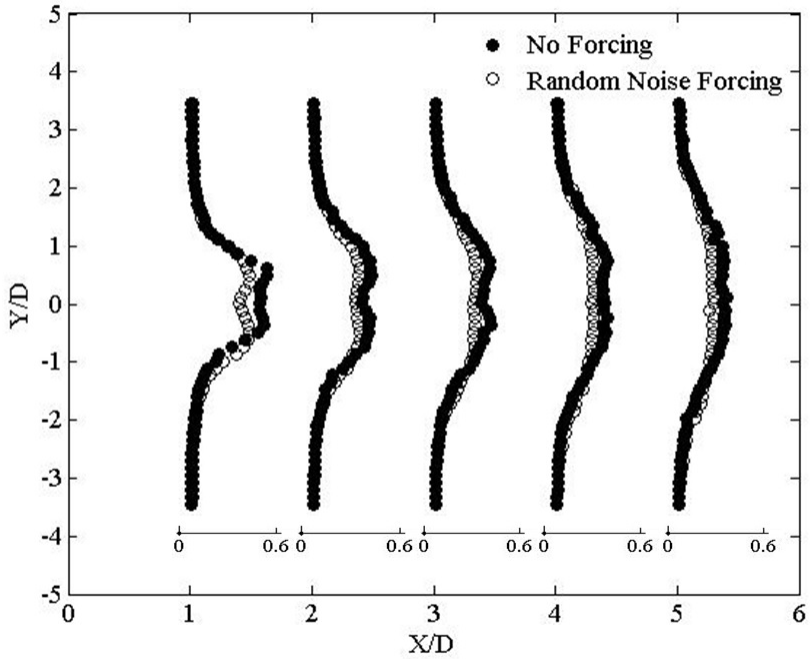


(a) Immediate Wake

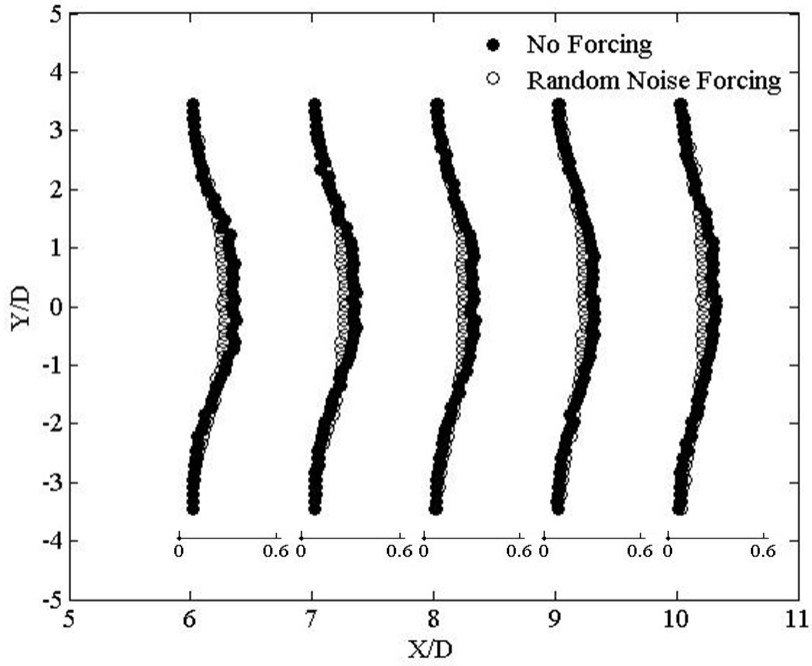


(b) Near Wake

Figure 3.39: Plots of perturbation velocity $u^{'}$, cylinder with trip strip, random noise forcing, two slits

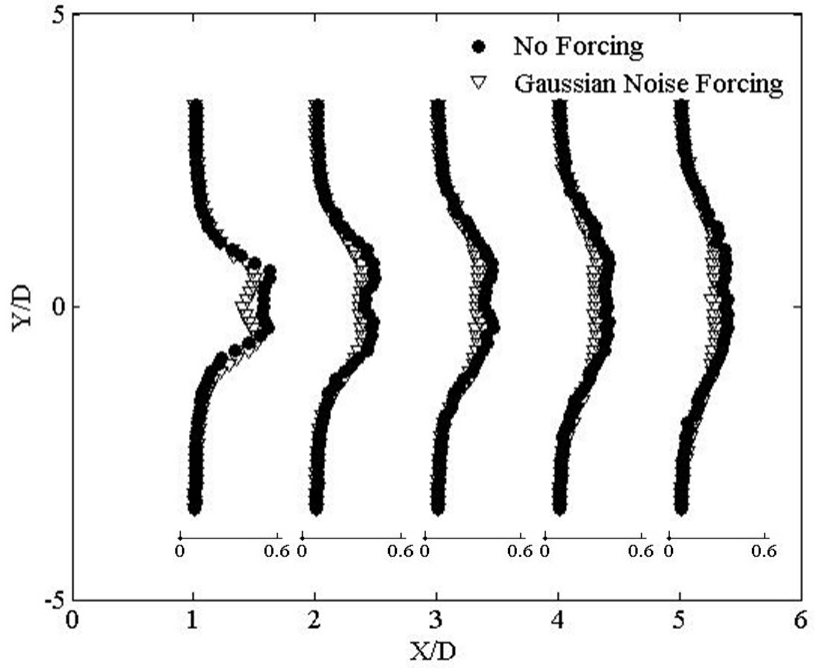


(a) Immediate Wake

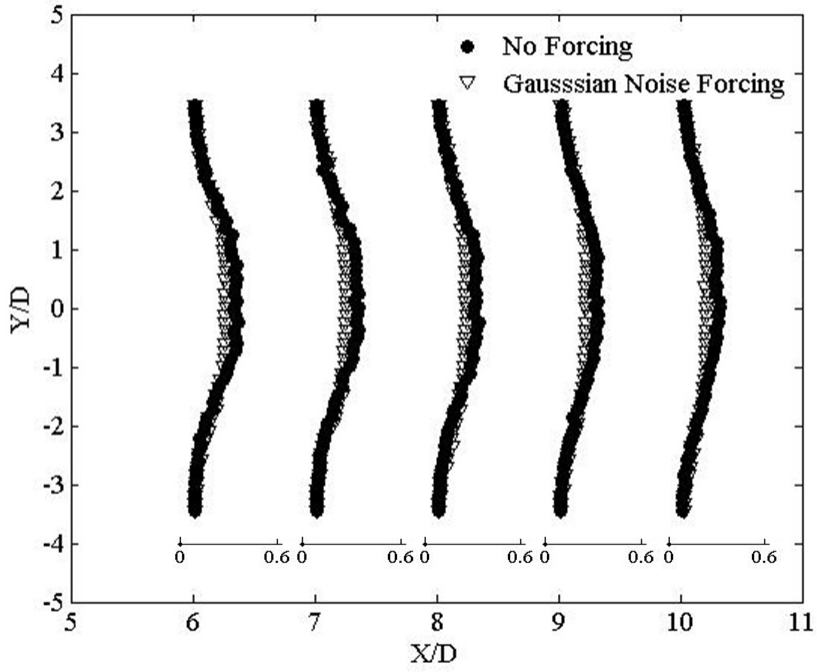


(b) Near Wake

Figure 3.40: Plots of perturbation velocity $u^{'}$, cylinder with trip strip, Gaussian noise forcing, two slits

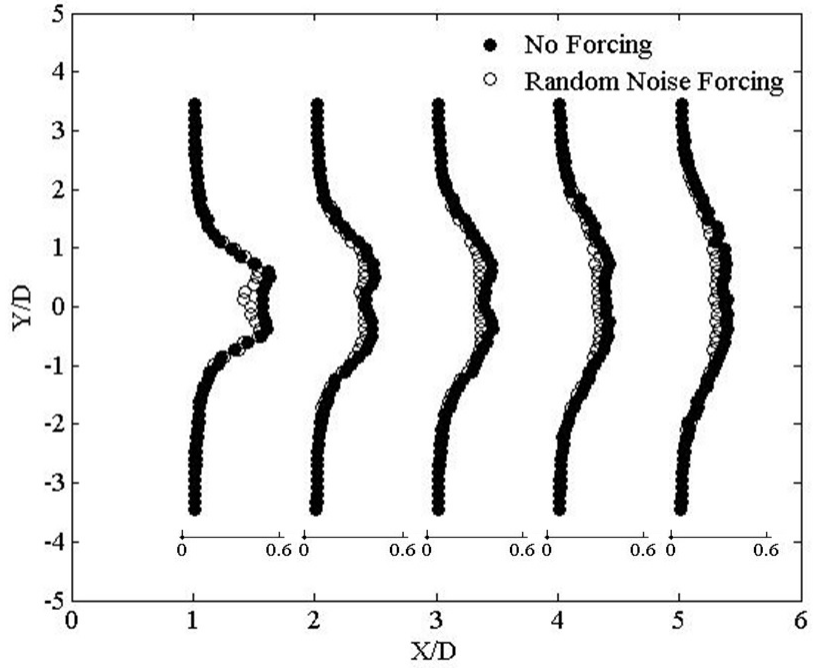


(a) Immediate Wake

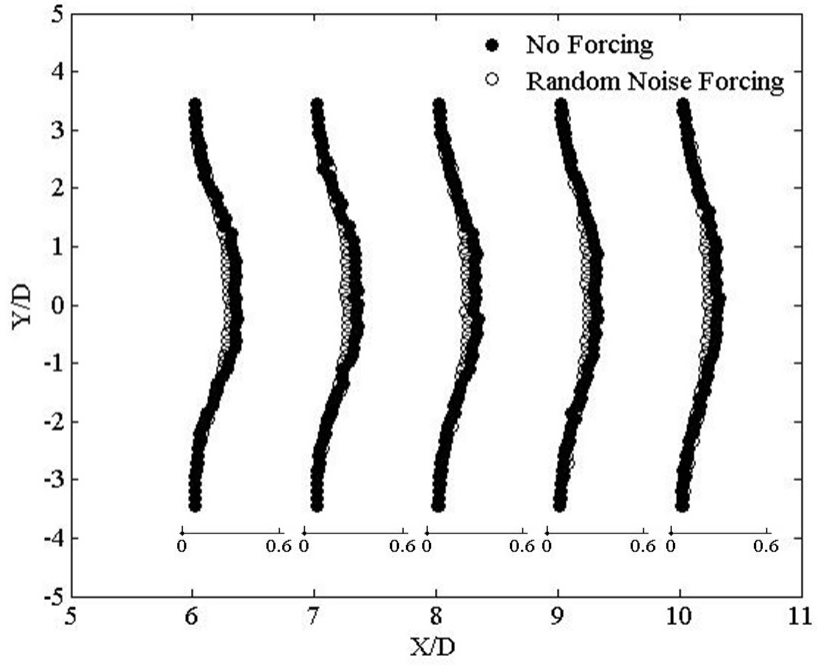


(b) Near Wake

Figure 3.41: Plots of perturbation velocity $u^{'}$, cylinder with trip strip, random noise forcing, single slit, $\phi = 90^{\circ}$

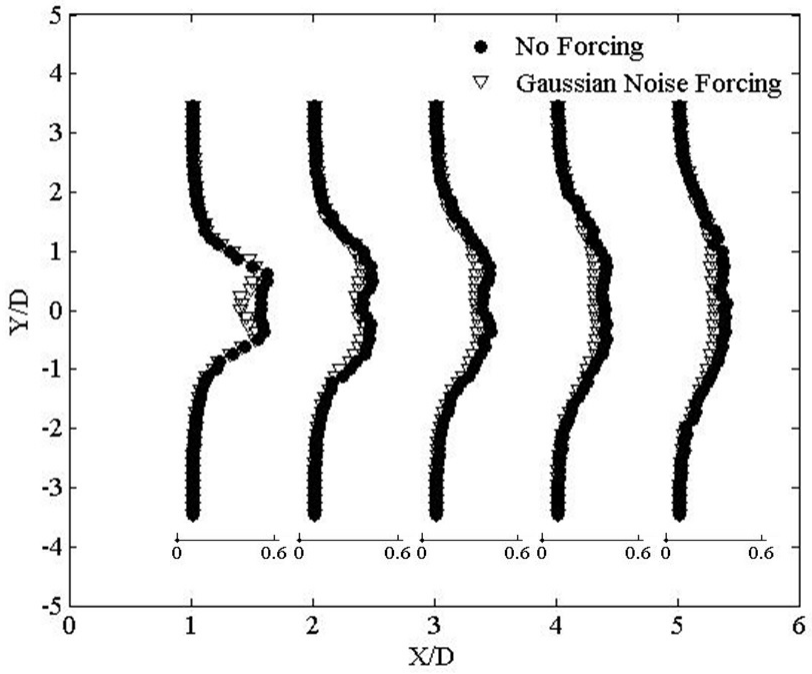


(a) Immediate Wake

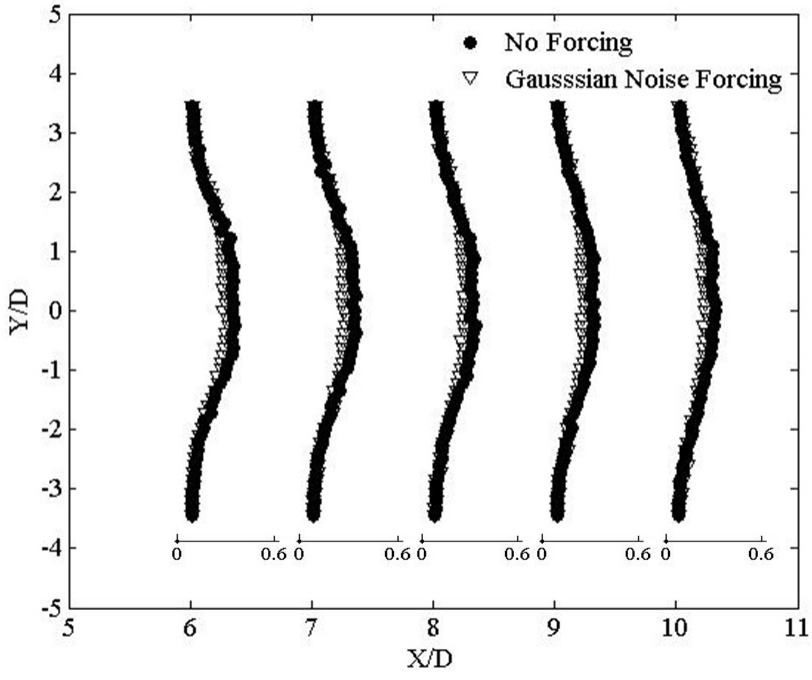


(b) Near Wake

Figure 3.42: Plots of perturbation velocity $u^{'}$, cylinder with trip strip, Gaussian noise forcing, single slit, $\phi = 90°$

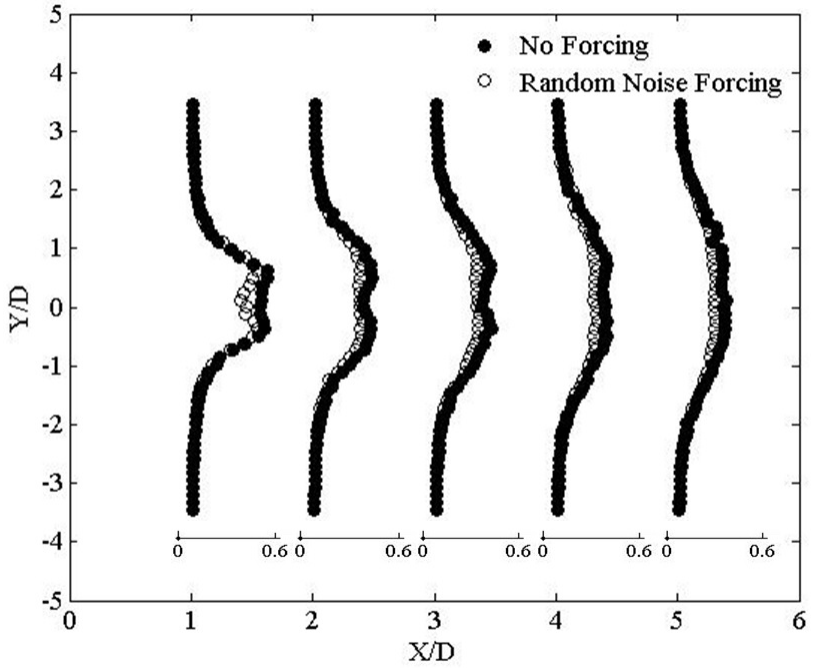


(a) Immediate Wake

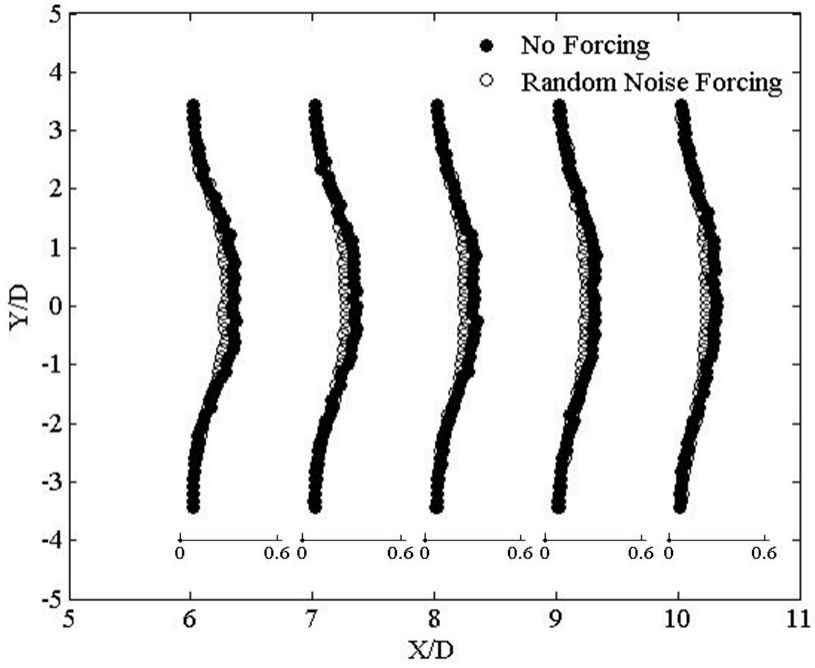


(b) Near Wake

Figure 3.43: Plots of perturbation velocity $u^{'}$, cylinder with trip strip, random noise forcing, single slit, $\phi = 95^{\circ}$

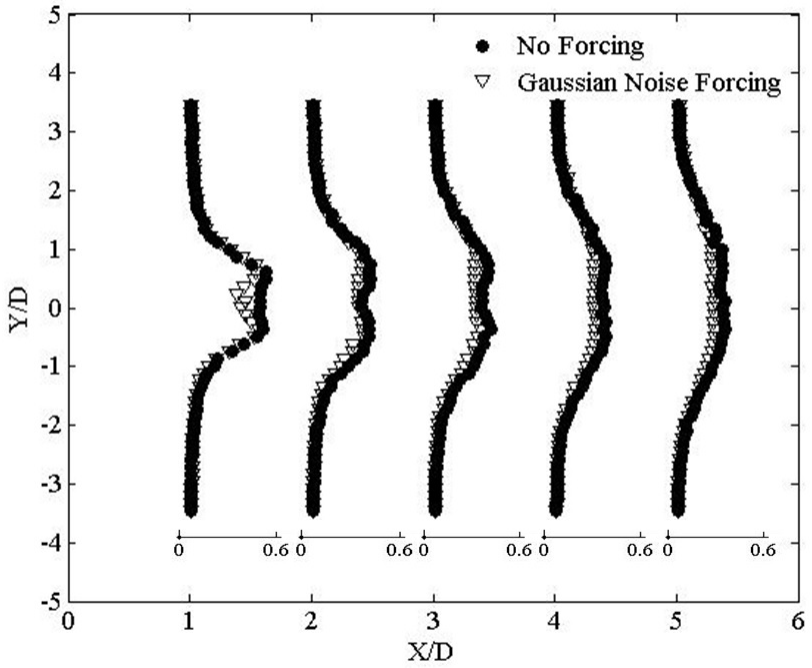


(a) Immediate Wake

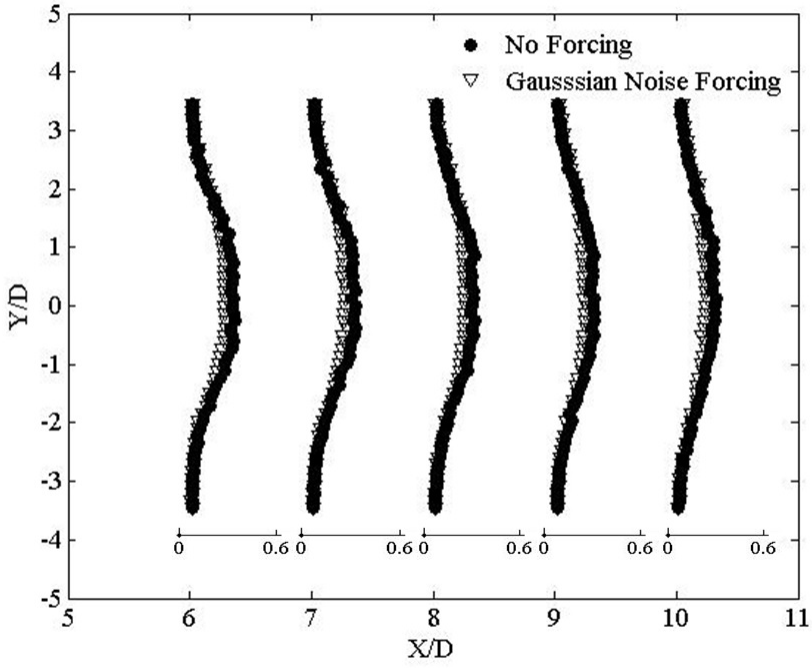


(b) Near Wake

Figure 3.44: Plots of perturbation velocity $u^{'}$, cylinder with trip strip, Gaussian noise forcing, single slit, $\phi = 95°$

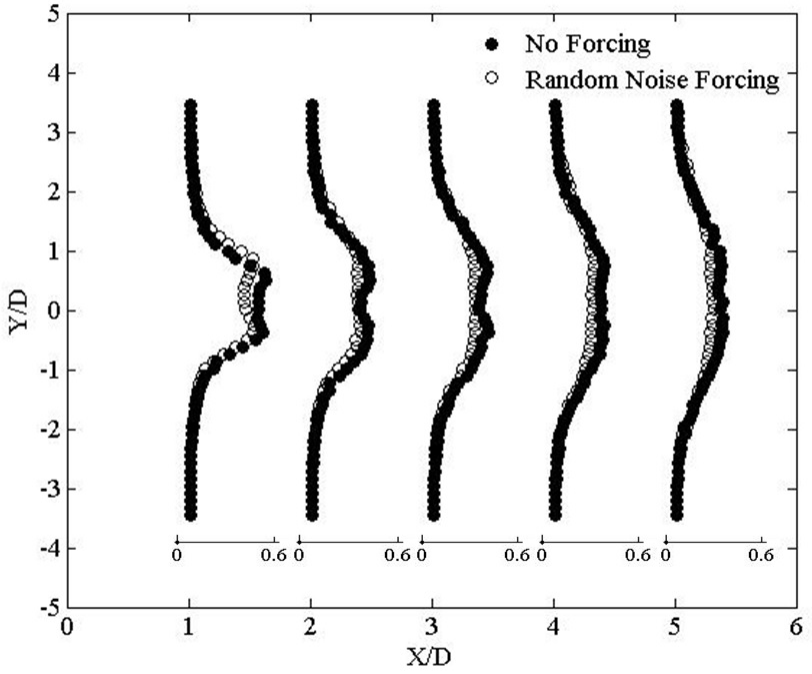


(a) Immediate Wake

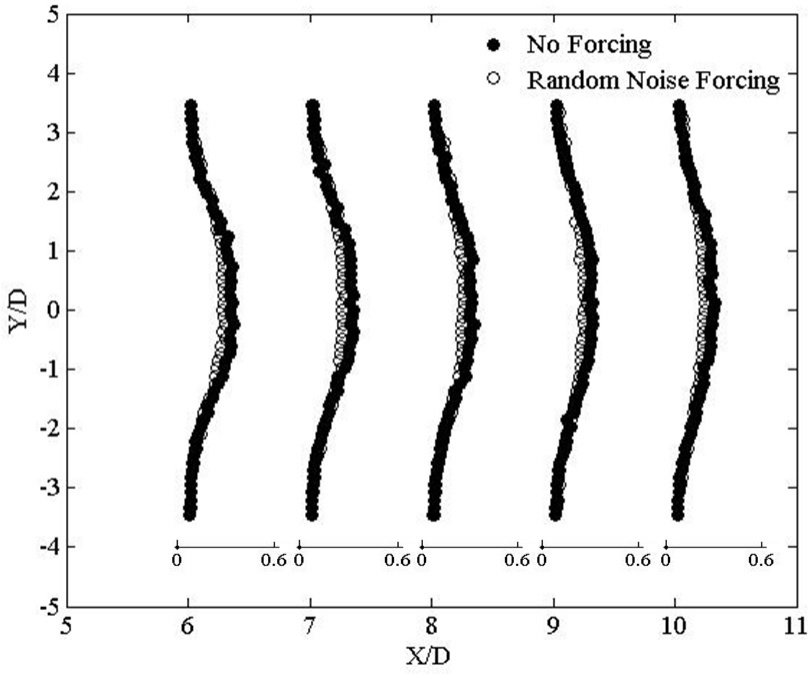


(b) Near Wake

Figure 3.45: Plots of perturbation velocity $u^{'}$, cylinder with trip strip, random noise forcing, single slit, $\phi = 100°$

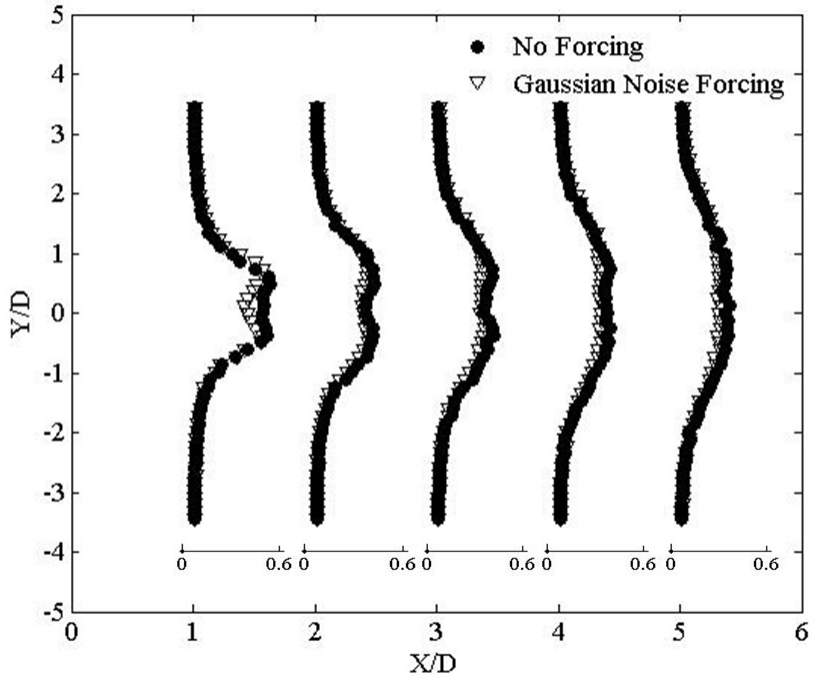


(a) Immediate Wake

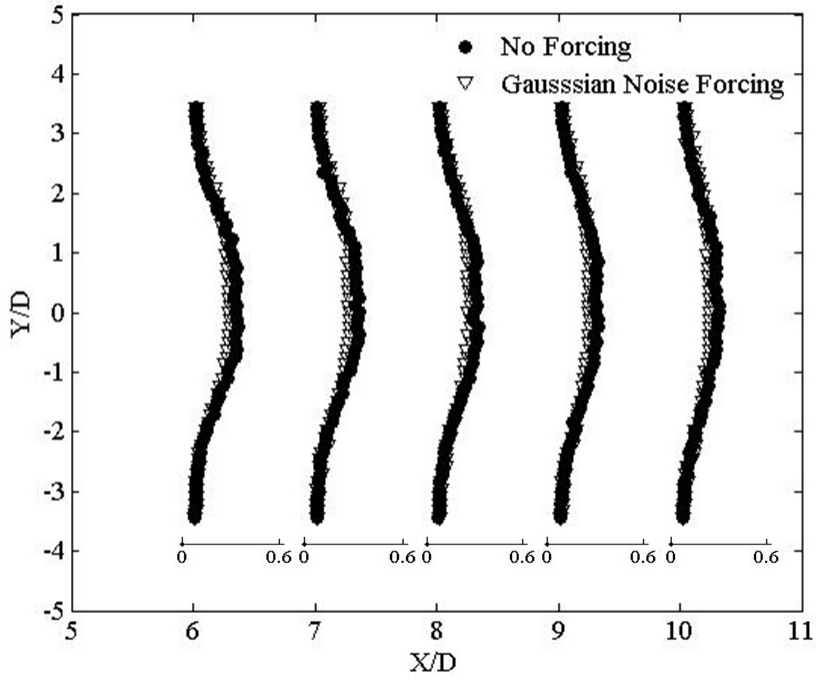


(b) Near Wake

Figure 3.46: Plots of perturbation velocity $u^{'}$, cylinder with trip strip, Gaussian noise forcing, single slit, $\phi = 100^{\circ}$

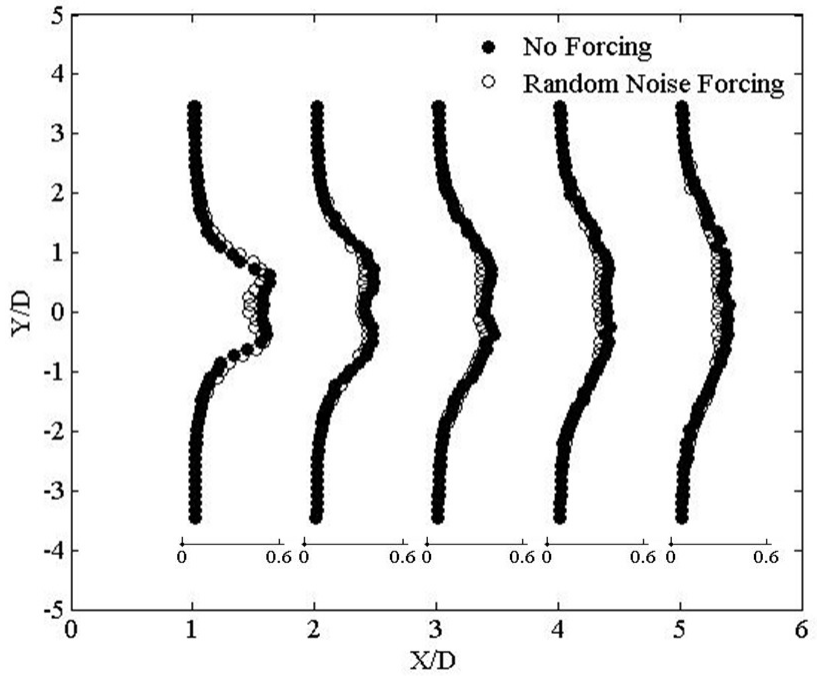


(a) Immediate Wake

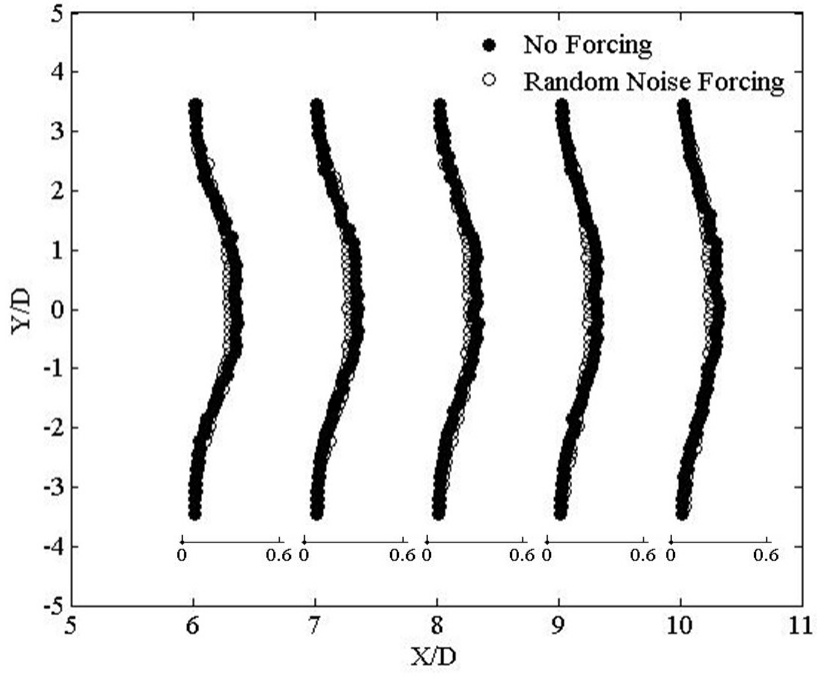


(b) Near Wake

Figure 3.47: Plots of perturbation velocity $u^{'}$, cylinder with trip strip, random noise forcing, single slit, $\phi = 105^{\circ}$

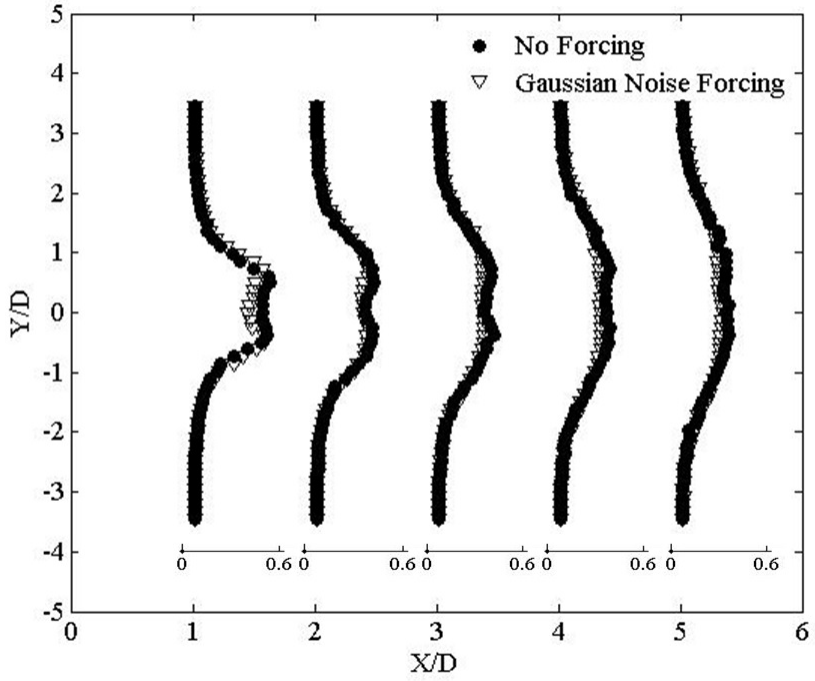


(a) Immediate Wake

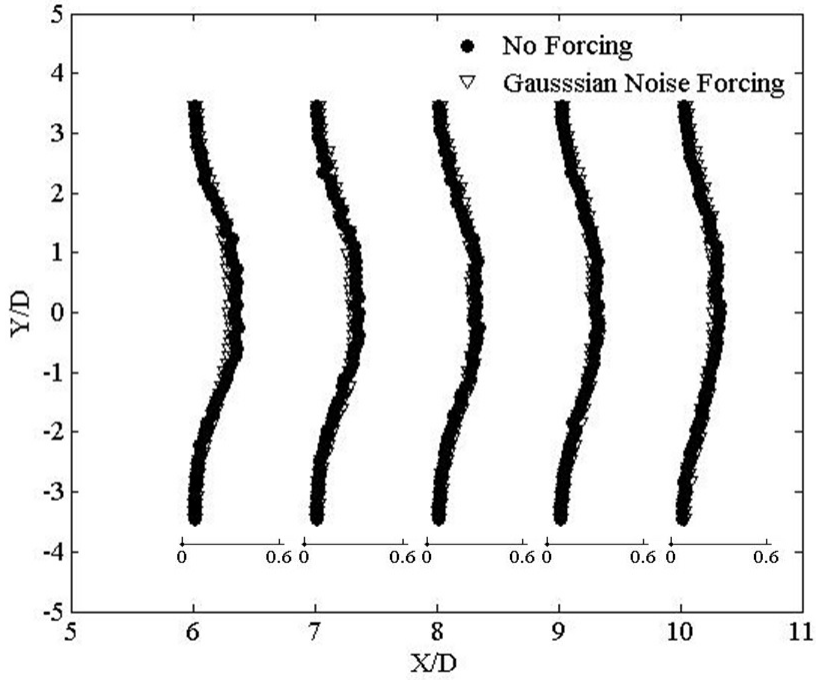


(b) Near Wake

Figure 3.48: Plots of perturbation velocity $u^{'}$, cylinder with trip strip, Gaussian noise forcing, single slit, $\phi = 105°$

## 3.5 Vortex Formation Length

The time-averaged flow in the wake of a circular cylinder contains alternatively shedding von Kármán vortices. Time-averaged streamlines of the flow describe the presence of a recirculation region starting immediately behind the cylinder, and extending upto a certain distance downstream of the wake. The recirculation region terminates at the confluence point of the separating shear layers in the wake centerline. The extent of the recirculation region behind the cylinder in the downstream of the wake is quantified by the vortex formation length $L$. Vortex formation length is described as the point in the wake centerline where velocity fluctuation $u^{'}$ reaches a maximum value. This can also be defined as the location along the wake centerline where the exterior flow first crosses into the wake. At this point in the wake, the interaction of shear layers caused the vortex shedding frequency to be doubled, having a high magnitude.

The no forcing case for smooth cylinder presented in Figure 3.49 shows a vortex formation length $L$ at X/D = 4. No forcing case for tripped cylinder showed a decrease in formation length, caused by delayed separation of the boundary layer. Noise forcing resulted in the acceleration of either the top shear layer (single slit forcing) or both shear layers (two slit forcing), which resulted in the contraction of the recirculation region in the wake. This allowed the freestream flow to cross the wake centerline at an earlier downstream location, allowing the breakdown of Kármán vortices into smaller structures. For the smooth cylinder, Two slit forcing and single slit forcing at all angles of $\phi$ showed that the reduction of formation length as observed from Figures 3.50 to 3.57.

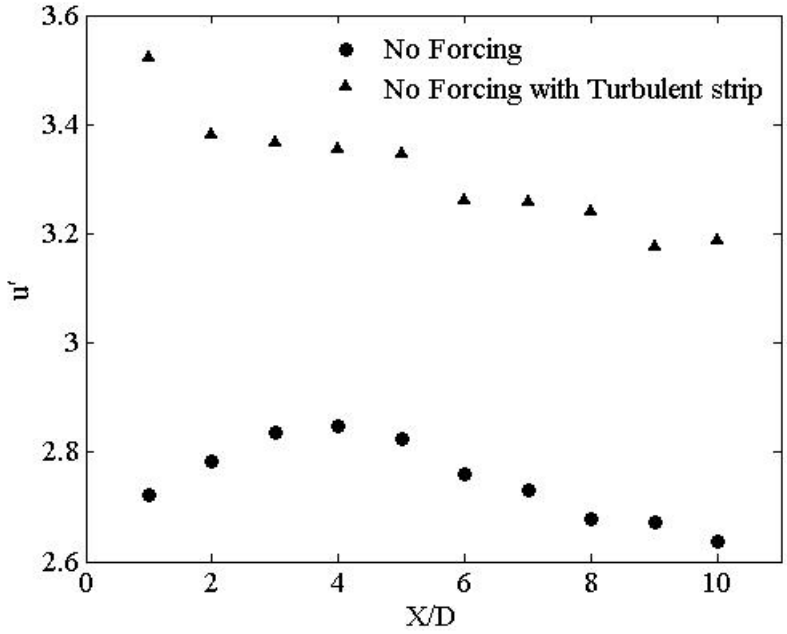


Figure 3.49: Vortex formation length, no forcing

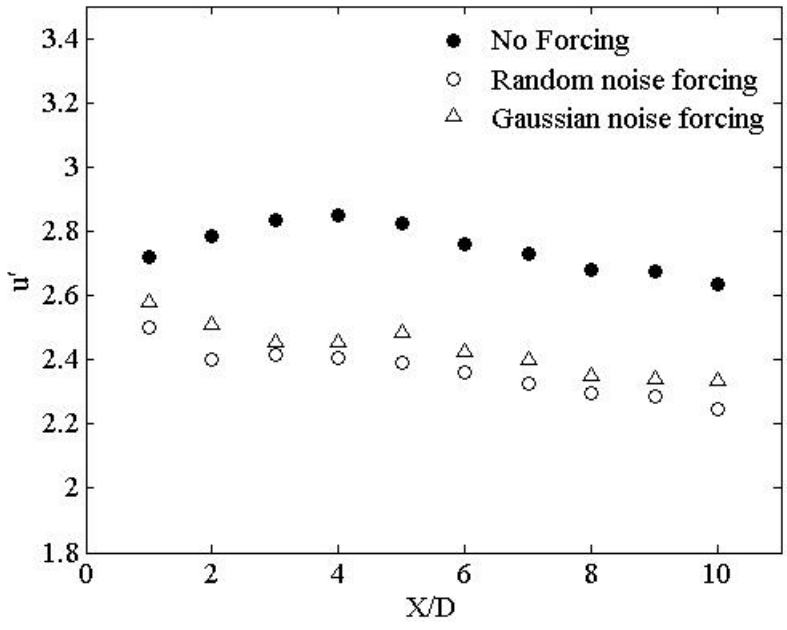


Figure 3.50: Vortex formation length, two slit forcing

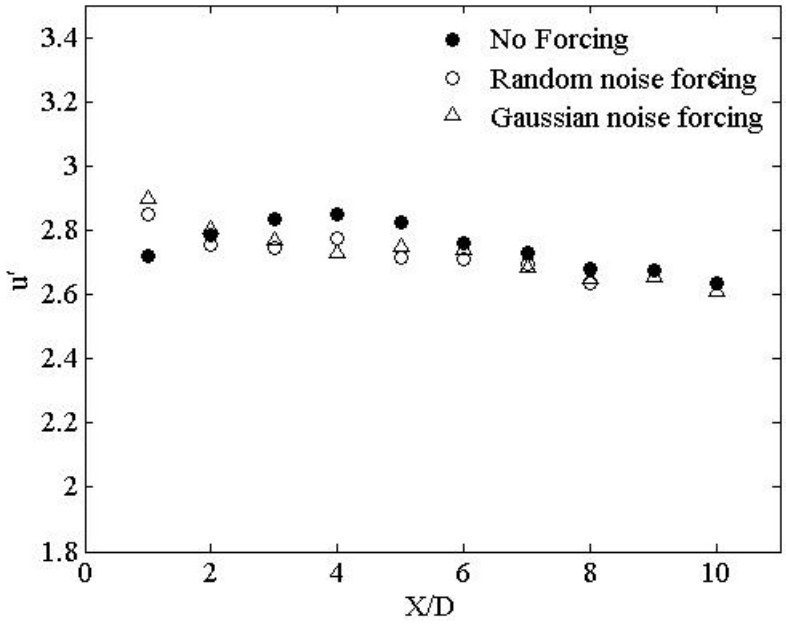


Figure 3.51: Vortex formation length, single slit forcing, $\phi = 60°$

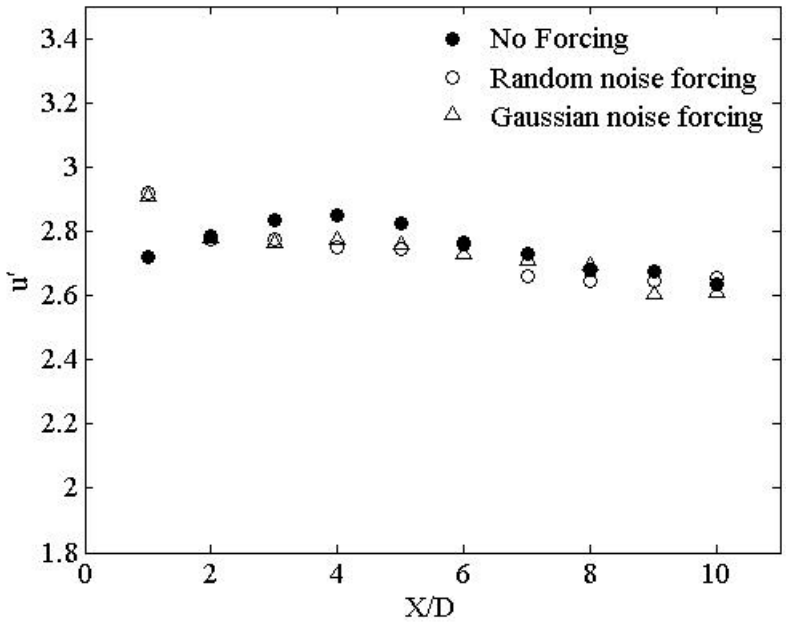


Figure 3.52: Vortex formation length, single slit forcing, $\phi = 65°$

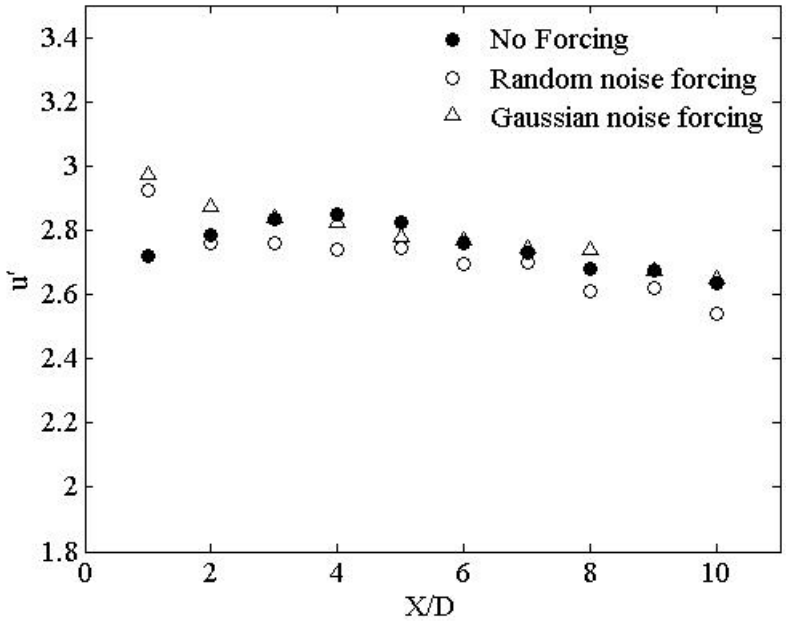


Figure 3.53: Vortex formation length, single slit forcing, $\phi = 70°$

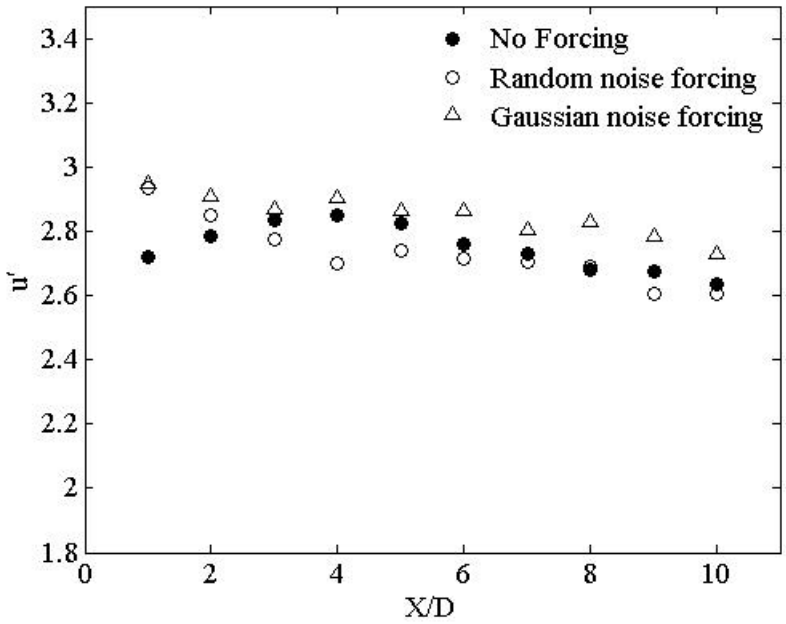


Figure 3.54: Vortex formation length, single slit forcing, $\phi = 75°$

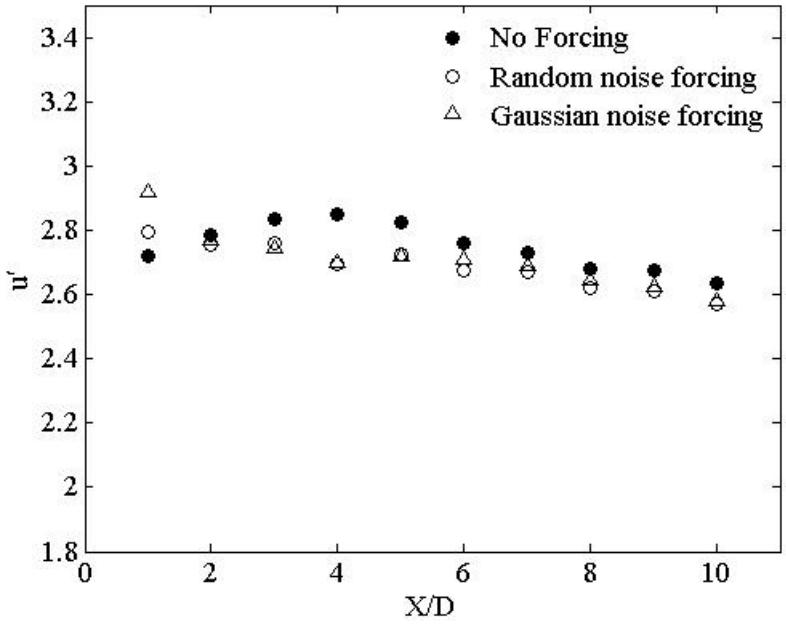


Figure 3.55: Vortex formation length, single slit forcing, $\phi = 80°$

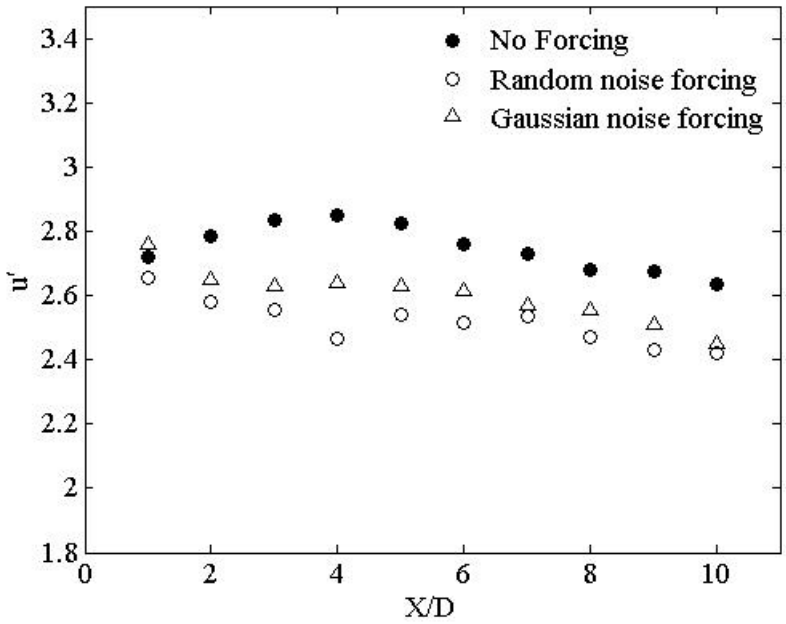


Figure 3.56: Vortex formation length, single slit forcing, $\phi = 85°$

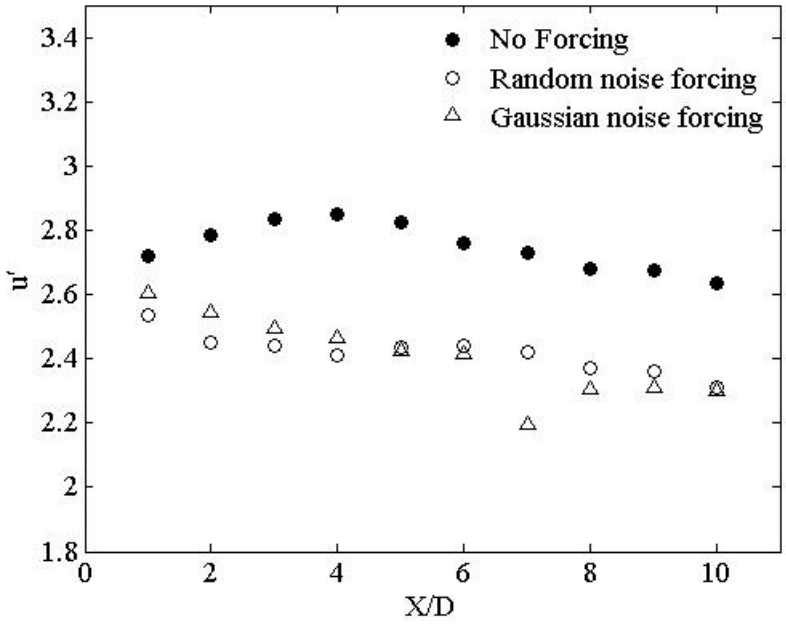


Figure 3.57: Vortex formation length, single slit forcing, $\phi = 90°$

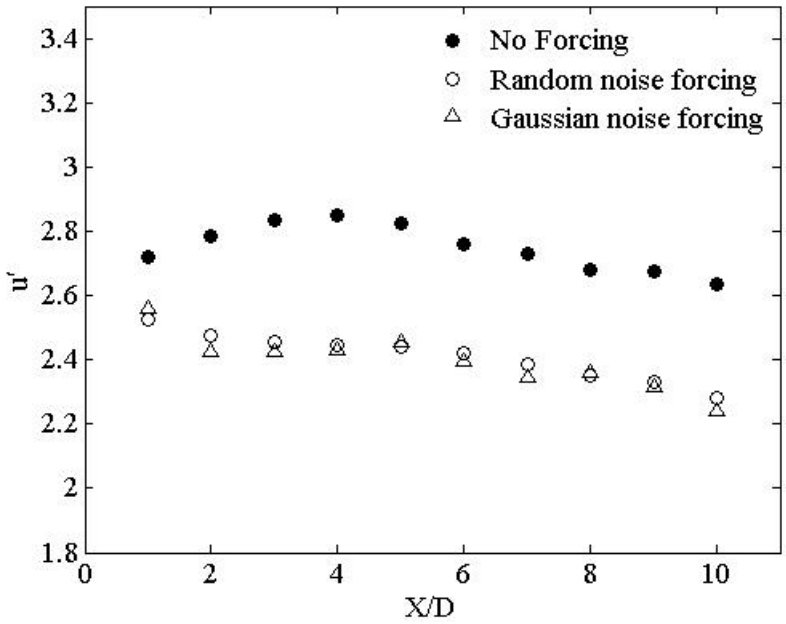


Figure 3.58: Vortex formation length, cylinder with trip strip, two slit forcing

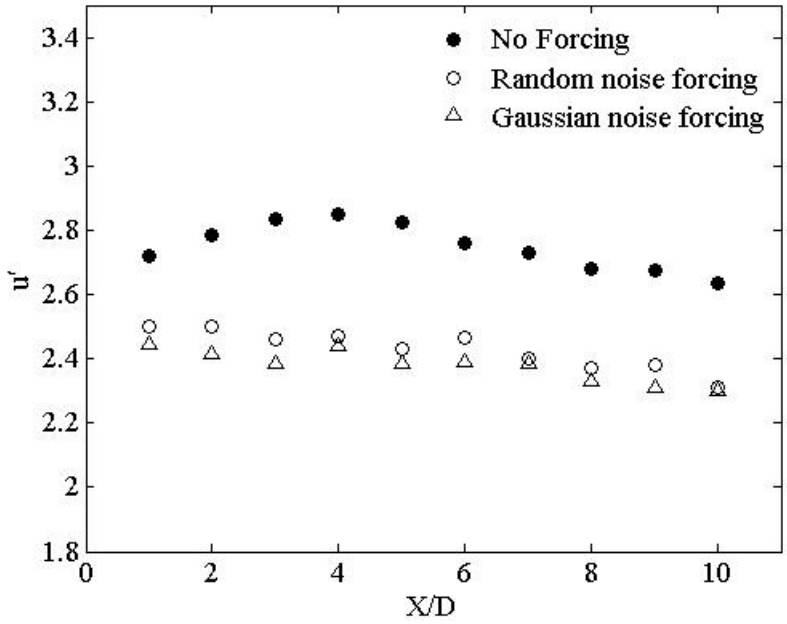


Figure 3.59: Vortex formation length, cylinder with trip strip, single slit forcing, $\phi = 90°$

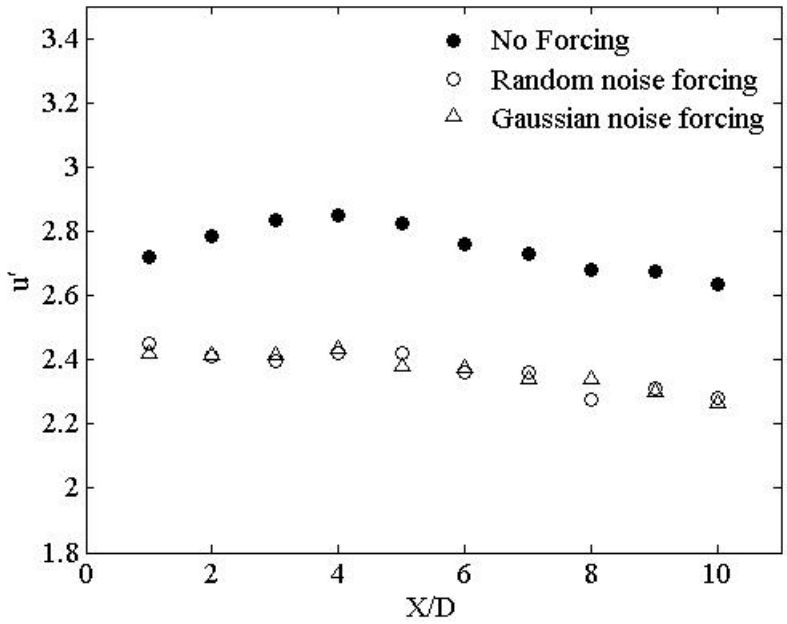


Figure 3.60: Vortex formation length, cylinder with trip strip, single slit forcing, $\phi = 95°$

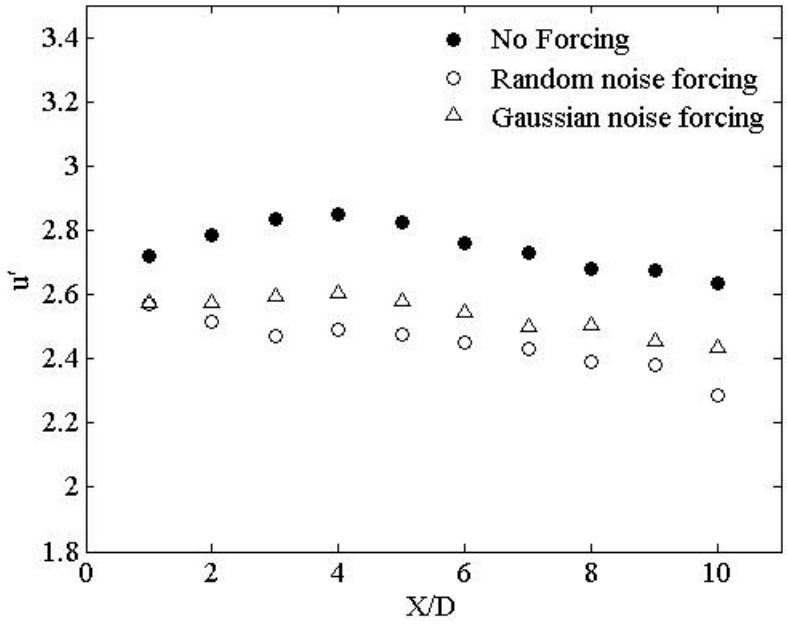


Figure 3.61: Vortex formation length, cylinder with trip strip, single slit forcing, $\phi = 100°$

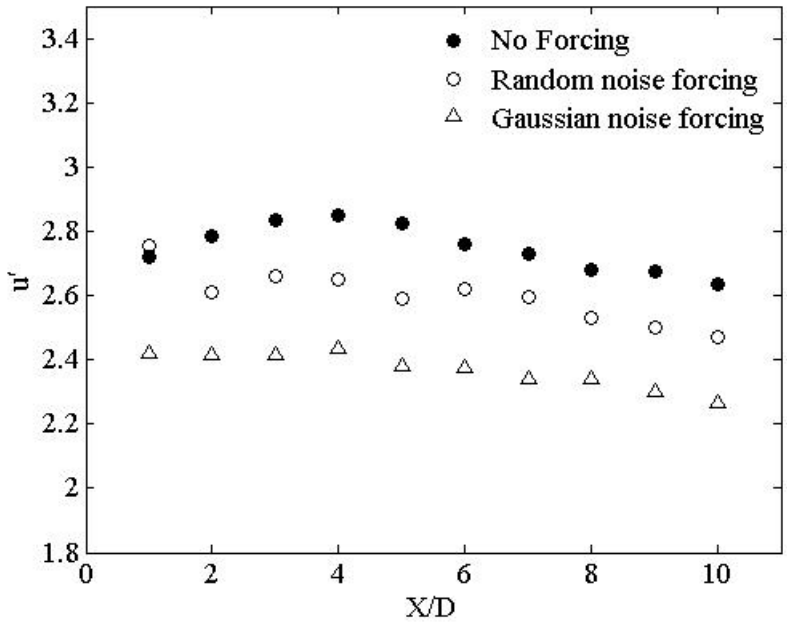


Figure 3.62: Vortex formation length, cylinder with trip strip, single slit forcing, $\phi = 105°$

### 3.6 Self - Preservation of the wake

Extensive research to characterize the near and far wakes behind a circular cylinder stated that the wake would have reached a self-similar or a self-preserved asymptotic state when all flow properties have reached a universal distribution, independent on the initial flow condition. The development of flow in the far wake was characterized by the drag contributed by the flow over the bluff body. The immediate wake of the body was strongly influenced by the characteristics of the body and also of the flow condition upstream. Turbulent structures underwent a change in the immediate wake of the cylinder. Vorticity generated by the wall of the cylinder was advected with the mean flow. Also, pressure field adjustments influenced the characteristics of the immediate wake. According to Sreenivasan [46], the wake is said to have reached a self- similar state when the following asymptotic conditions are reached.

$$W_0 \ \propto \ X^{-\frac{1}{2}}$$

$$b \ \propto \ X^{\frac{1}{2}}$$

where $W_0$ is the maximum velocity deficit and $b$ is the wake half width. The self - preservation of the wake were described by the expressions

$$\left(\frac{W_0}{U_0}\right)\sqrt{\frac{X}{\theta}}$$

$$\frac{b}{\sqrt{X\theta}}$$

where $\theta$ is termed as the momentum thickness in the wake. The self - similarity parameter reaches an asymptotic value of 1.63 in the far wake. Momentum thickness of the wake is given by the expression

$$\theta = \int_{-\infty}^{\infty} \frac{U}{U_\infty}\left(1 - \frac{U}{U_\infty}\right) dy$$

The behavior of wake deficit similarity parameter downstream of the wake would indicate the manner in which the wake would reach asymptotic state. The parameter was used to describe the variation of $W_0$ in relation to downstream location in the wake. In Figure 3.64, no forcing case for a smooth cylinder showed a regularly asymptotic approach further downstream. However, no forcing for the tripped cylinder showed an almost linear approach to self - similarity. The behavior of this similarity parameter has indicated that each case of noise forcing, either using two slits or a single slit had different approaches to self - similarity. The general trend for all the noise forcing cases showed that the immediate wake had a slightly higher magnitude of the parameter, which maybe attributed to the increase of maximum wake deficit $W_0$ caused by the action of noise forcing on the near wake characteristics of the cylinder. Further downstream, the parameter indicated that the behavior of similarity parameter has changed in order to reach another state of self - preservation. The effect of noise forcing on the wake of the smooth cylinder both for two slit and single slit actuation were depicted in Figures 3.65 to 3.72, which was a trend different from the no forcing case. A similar trend was also observed from Figures 3.73 to 3.77.

Another parameter used in describing the self-similar approach of the wake is the half wake width similarity parameter. This parameter was used to describe how the half wake width of the wake reached asymptotic state. Half wake width is defined as the location on the wake from the center-line where the velocity deficit is half the maximum velocity deficit at that location in the wake.

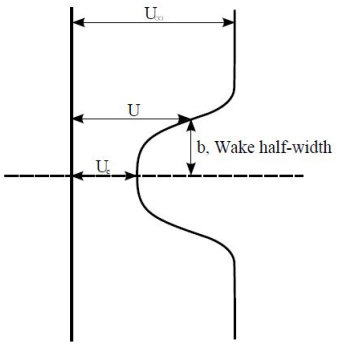


Figure 3.63: Illustration of half wake width

$$U_\infty - U = \frac{1}{2}(U_\infty - U_c)$$

No forcing cases for both smooth and tripped cylinders observed the wake width parameter reaching self-preservation (Fig. 3.78). Noise forcing caused increased dissipation in the near and immediate wake of the cylinder. This resulted in decreased velocity deficit, with an increase in values of half wake width $b$. Noise forcing altered the approach of $b$ to self-preservation state. Each forcing case caused the trend of $b$ to follow a different trend to self-similarity (Figures 3.81 to 3.88).

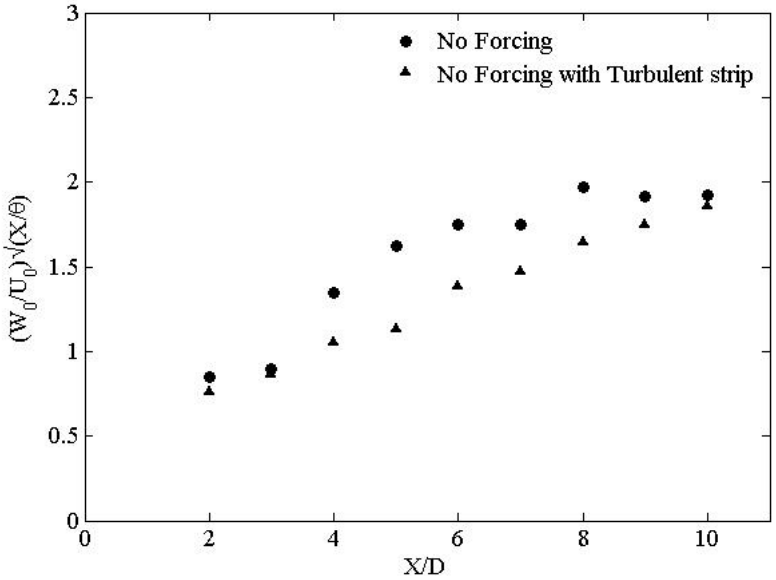


Figure 3.64: Wake deficit parameter, no forcing

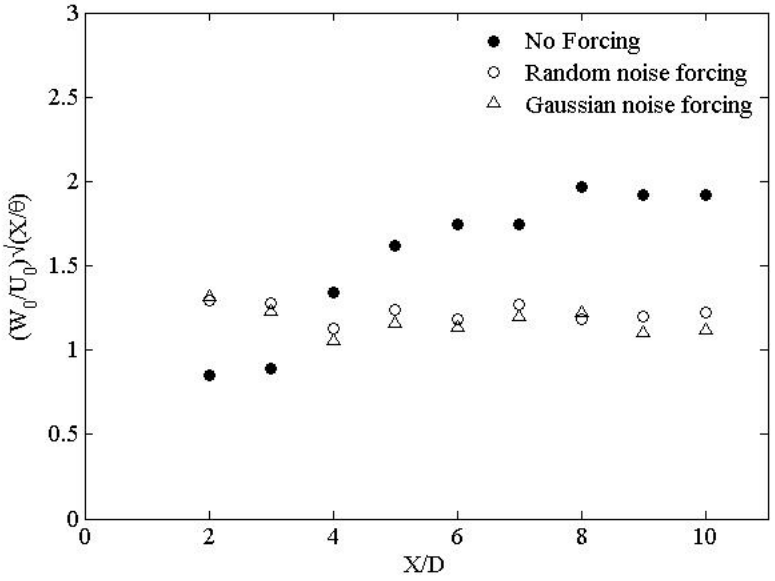


Figure 3.65: Wake deficit parameter, smooth cylinder, two slit forcing

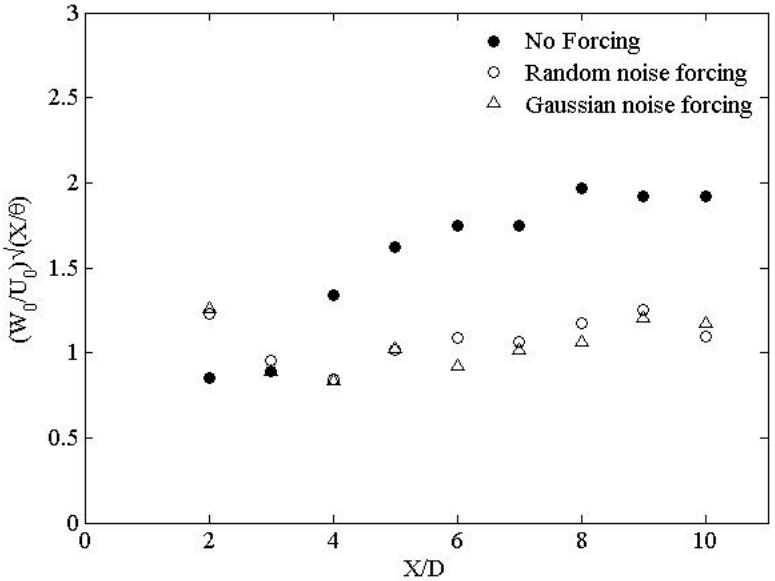


Figure 3.66: Wake deficit parameter, smooth cylinder, single slit forcing, $\phi = 60°$

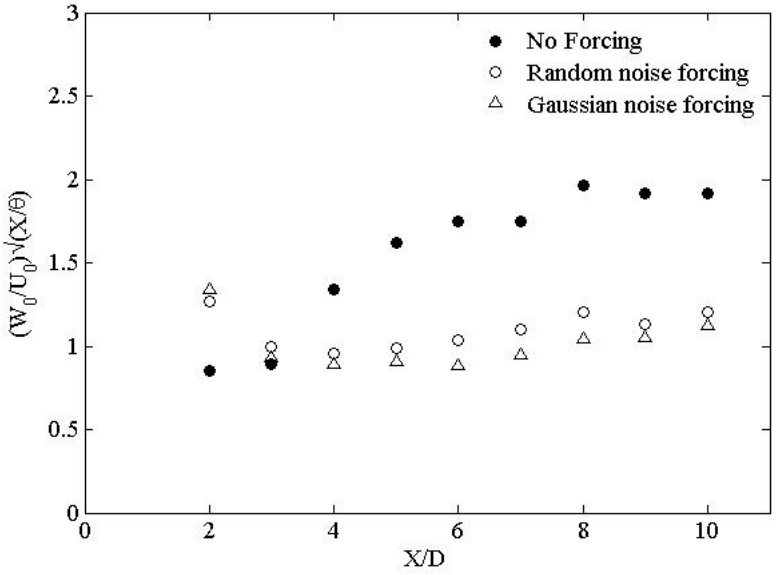


Figure 3.67: Wake deficit parameter, smooth cylinder, single slit forcing, $\phi = 65°$

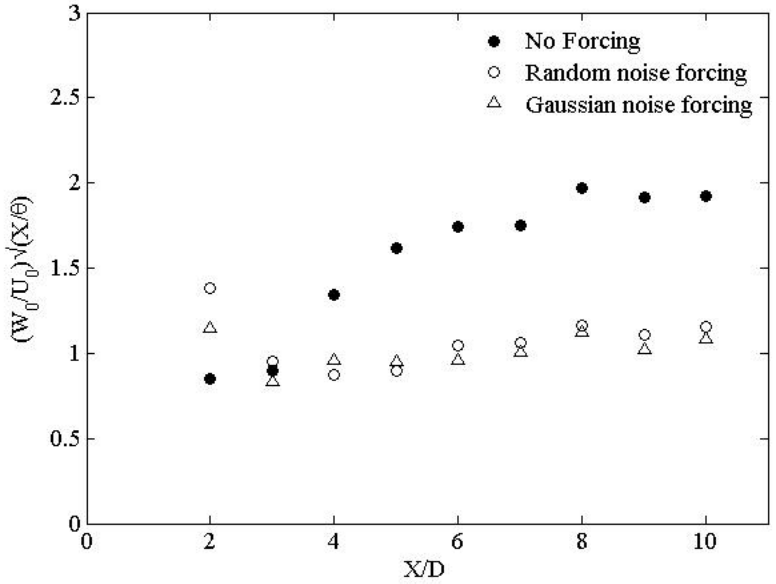


Figure 3.68: Wake deficit parameter, smooth cylinder, single slit forcing, $\phi = 70°$

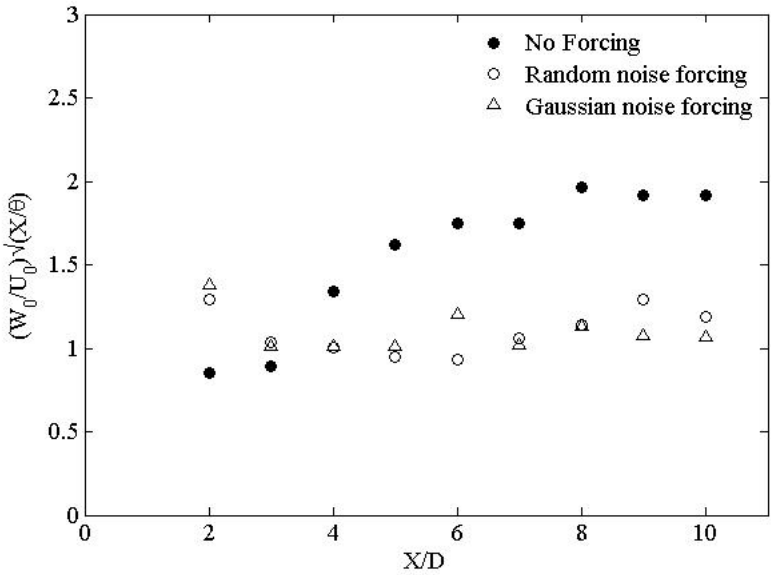


Figure 3.69: Wake deficit parameter, smooth cylinder, single slit forcing, $\phi = 75°$

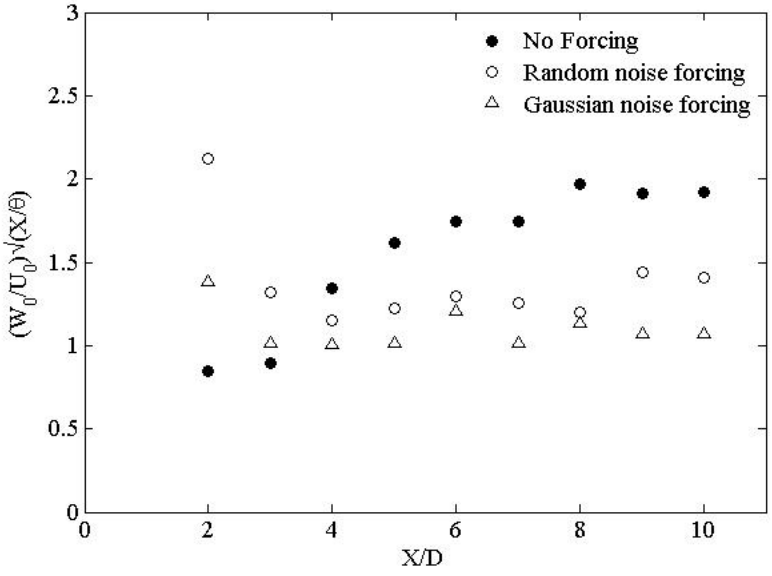


Figure 3.70: Wake deficit parameter, smooth cylinder, single slit forcing, $\phi = 80°$

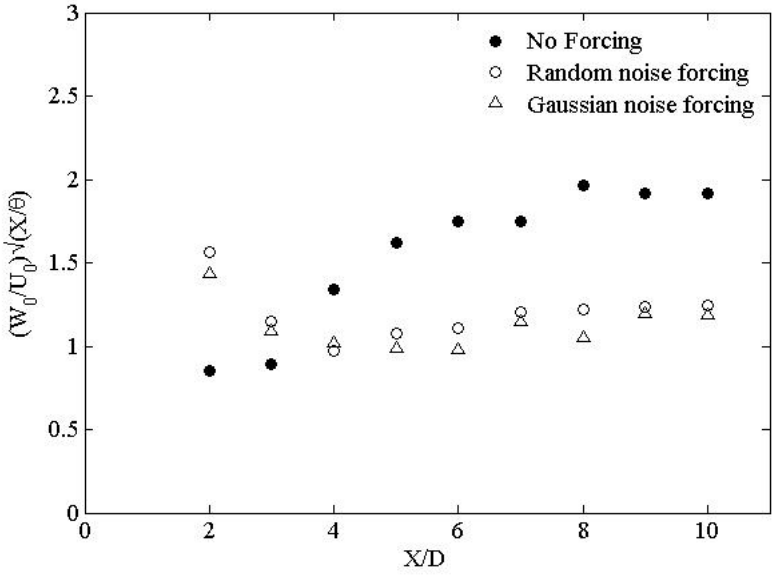


Figure 3.71: Wake deficit parameter, smooth cylinder, single slit forcing, $\phi = 85°$

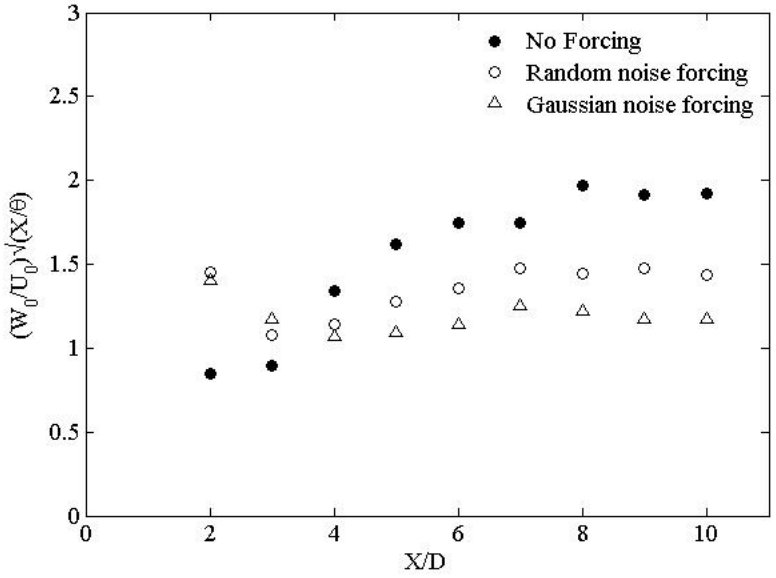


Figure 3.72: Wake deficit parameter, smooth cylinder, single slit forcing, $\phi = 90°$

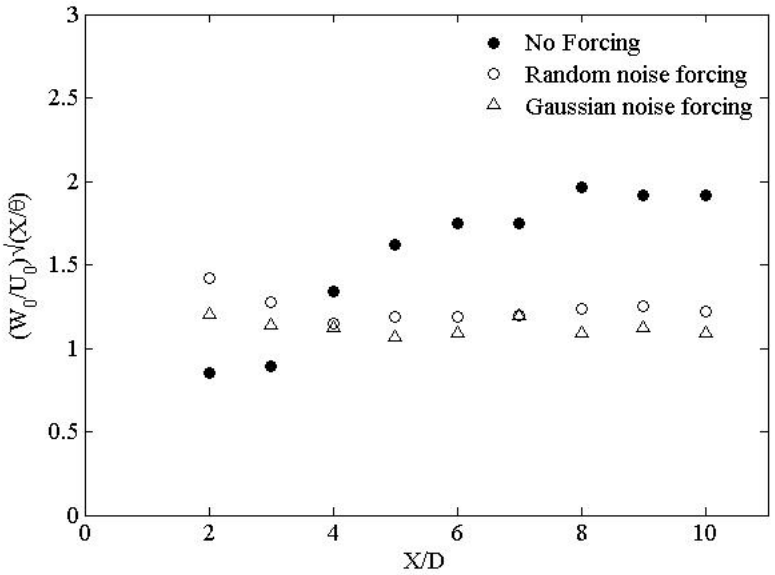


Figure 3.73: Wake deficit parameter, tripped cylinder, two slit forcing

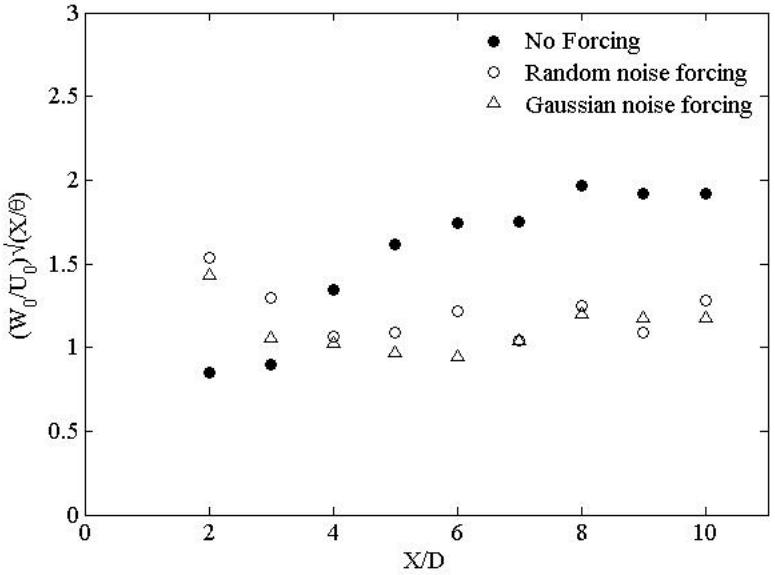


Figure 3.74: Wake deficit parameter, tripped cylinder, single slit forcing, $\phi = 90°$

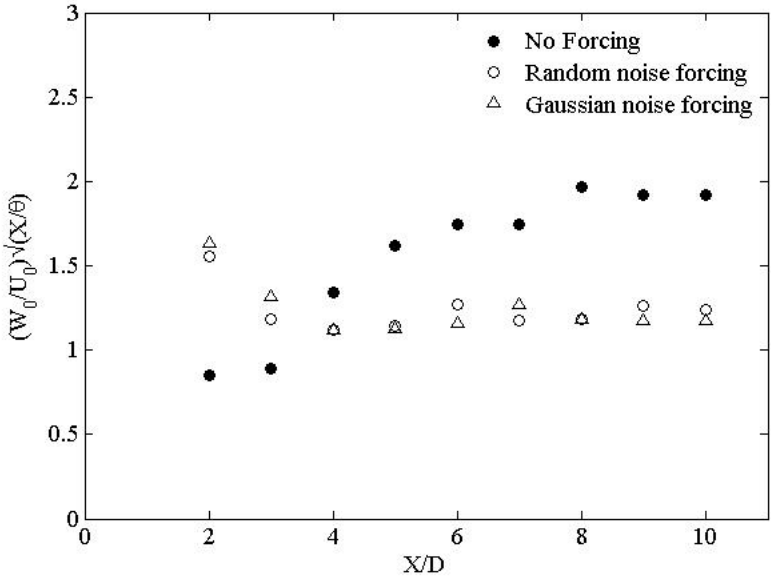


Figure 3.75: Wake deficit parameter, tripped cylinder, single slit forcing, $\phi = 95°$

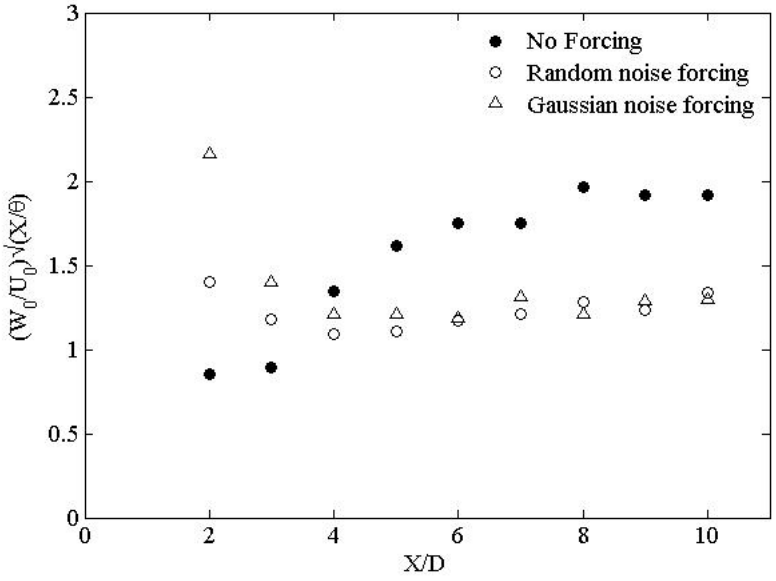


Figure 3.76: Wake deficit parameter, tripped cylinder, single slit forcing, $\phi = 100°$

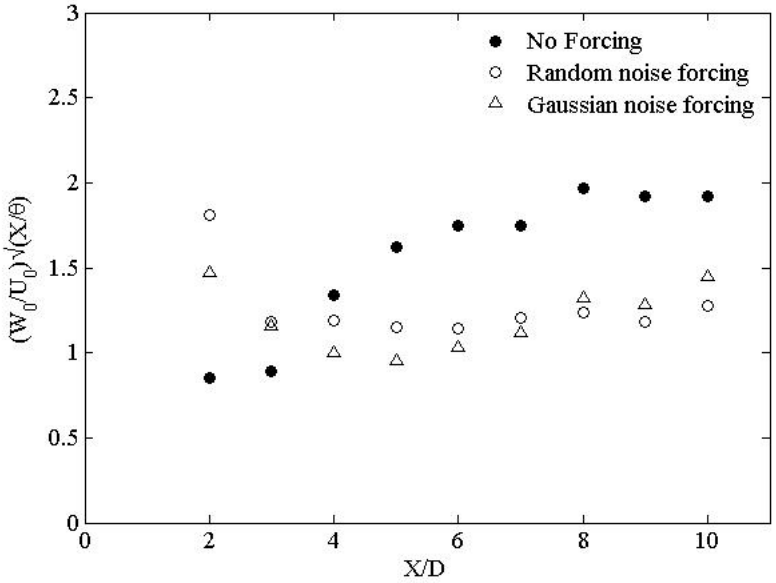


Figure 3.77: Wake deficit parameter, tripped cylinder, single slit forcing, $\phi = 105°$

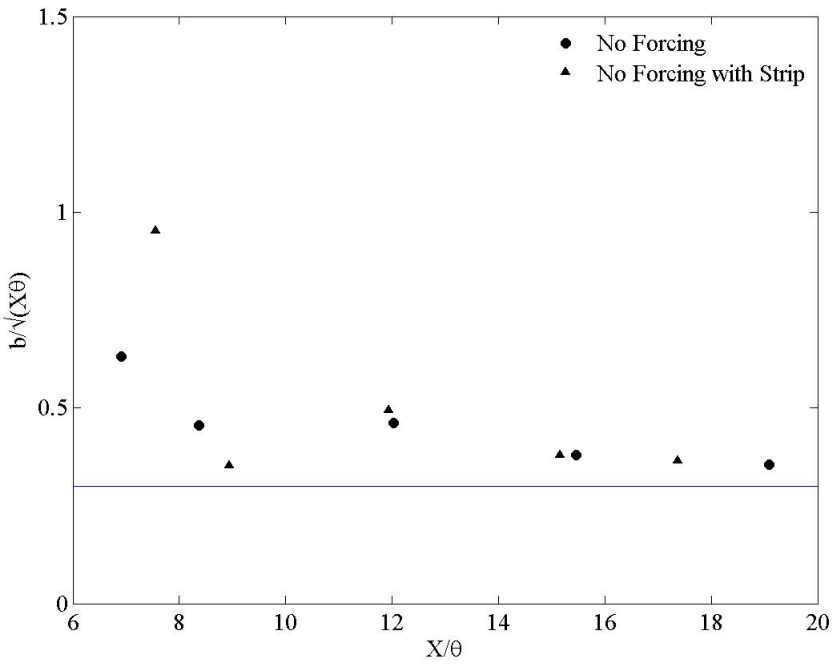


Figure 3.78: Half wake width parameter, no forcing

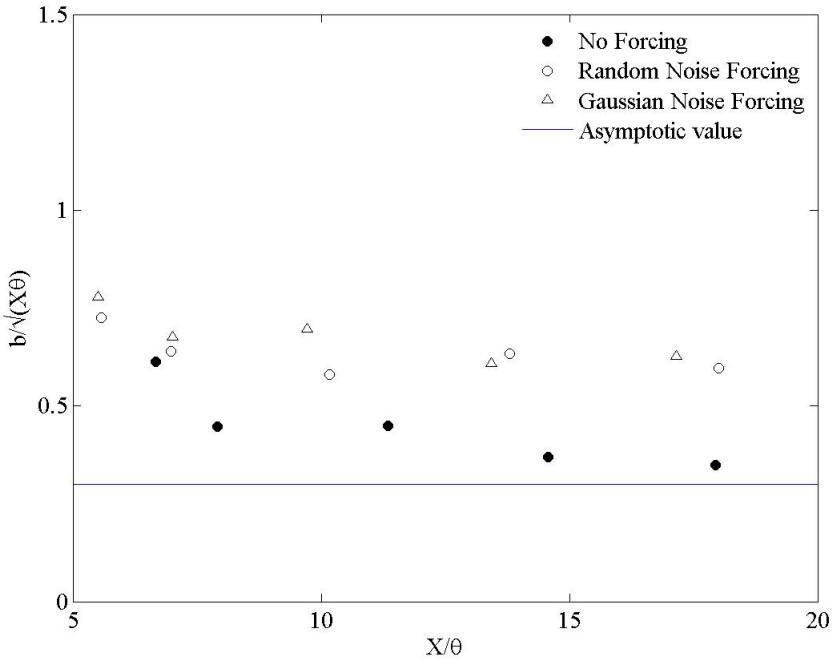


Figure 3.79: Half wake width parameter, two slit forcing

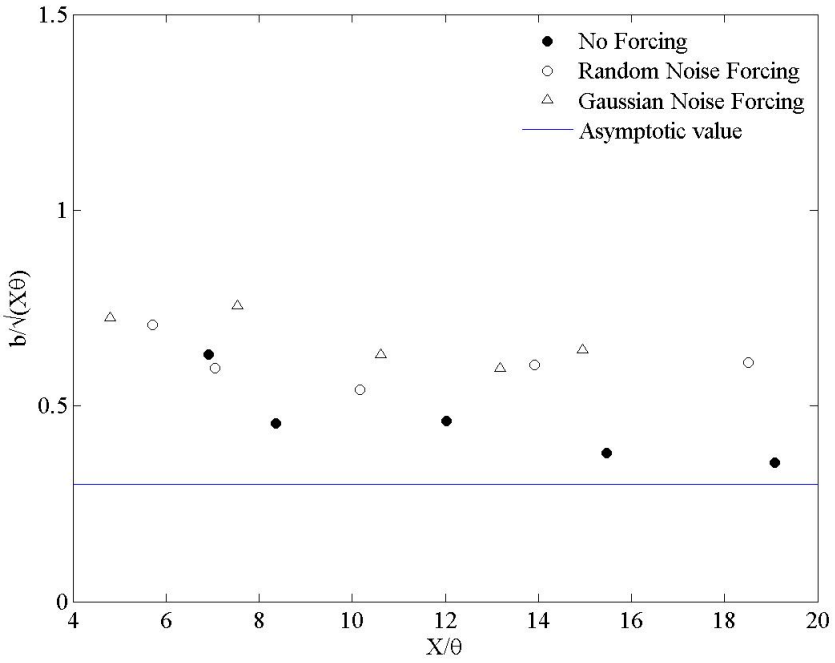


Figure 3.80: Half wake width parameter, cylinder with trip strip, two slit forcing

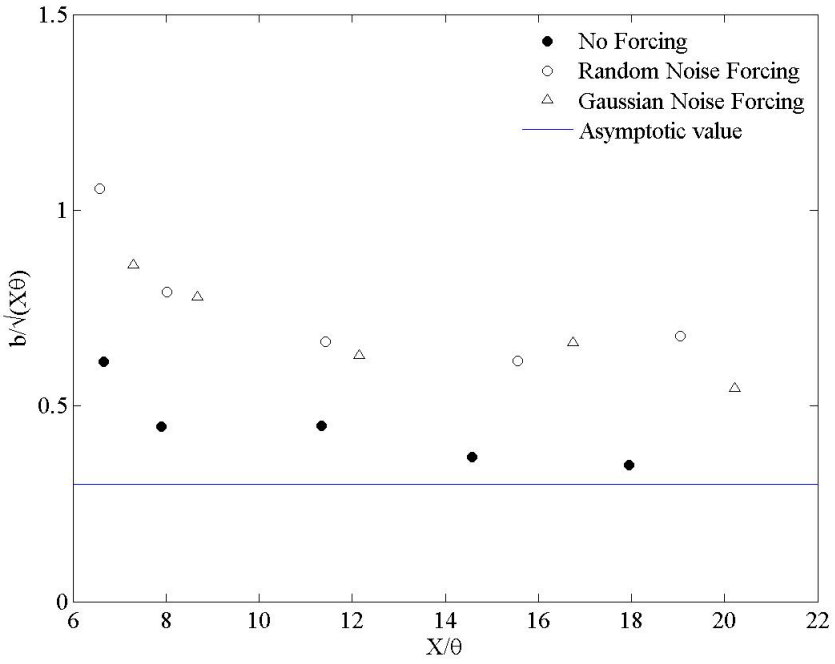


Figure 3.81: Half wake width parameter, single slit forcing, $\phi$ =60°

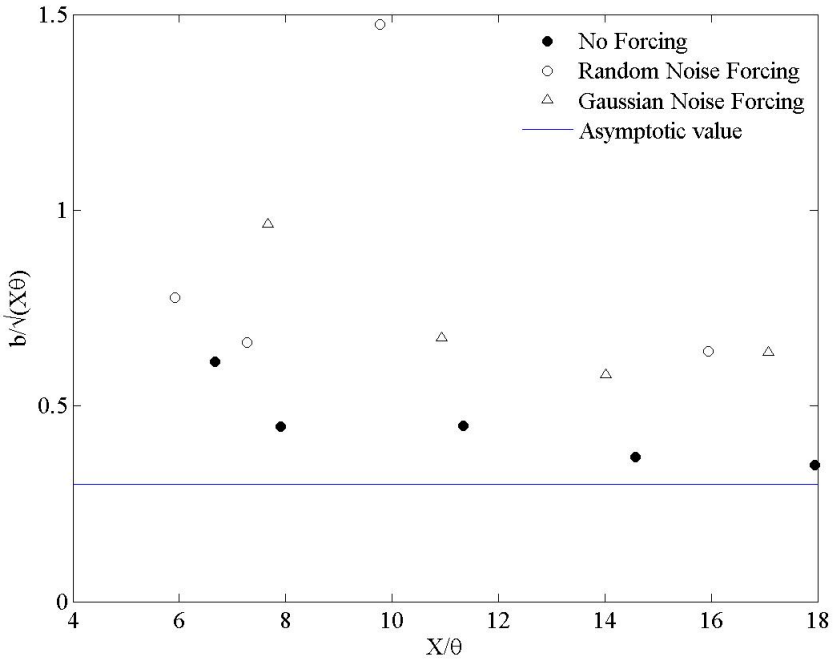


Figure 3.82: Half wake width parameter, single slit forcing, $\phi$ =65°

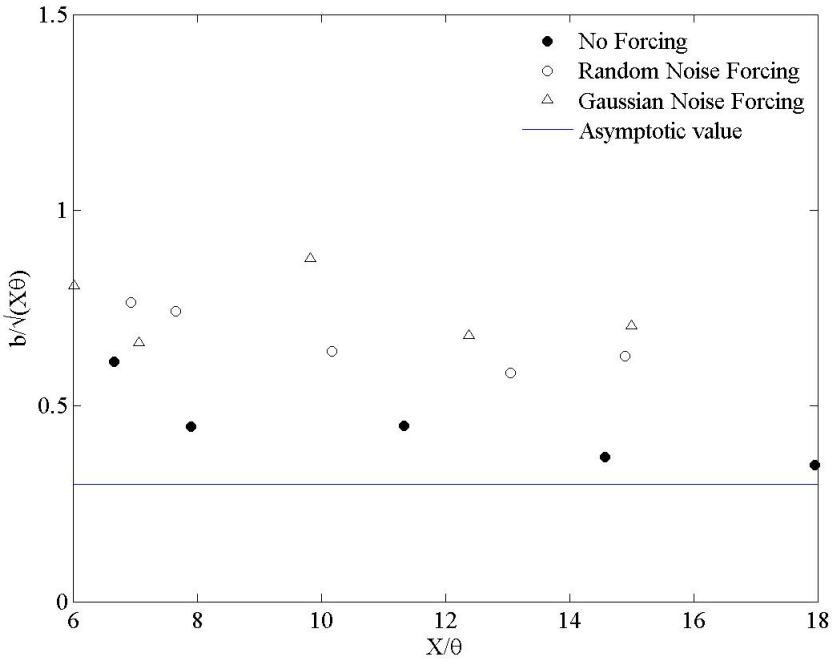


Figure 3.83: Half wake width parameter, single slit forcing, $\phi$ =70°

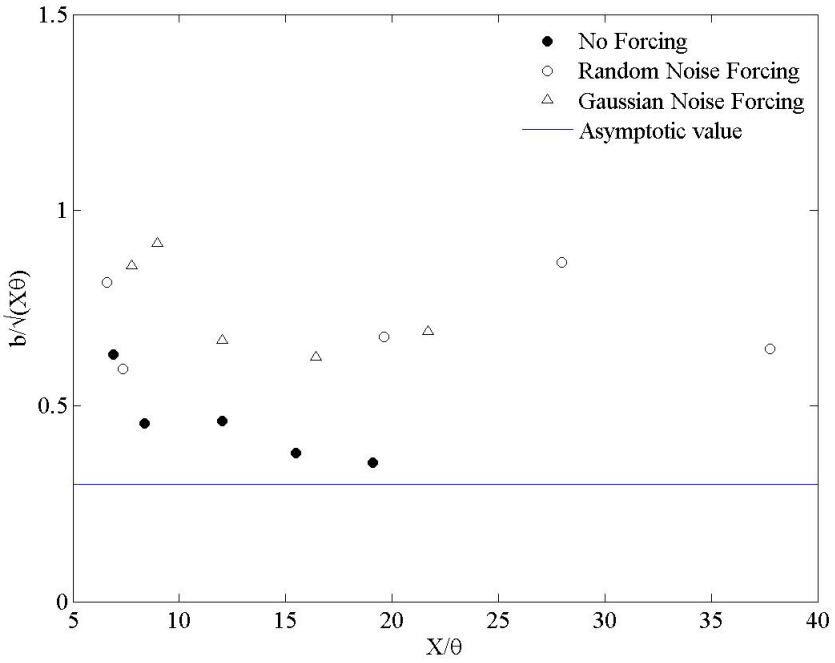


Figure 3.84: Half wake width parameter, single slit forcing, $\phi$ =90°

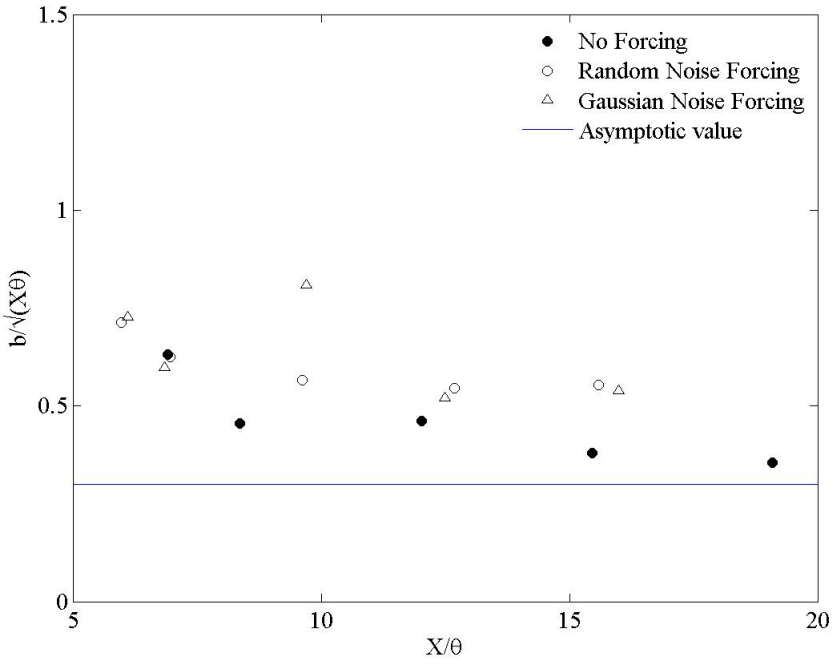


Figure 3.85: Half wake width parameter, cylinder with trip strip, single slit forcing, $\phi$ =90°

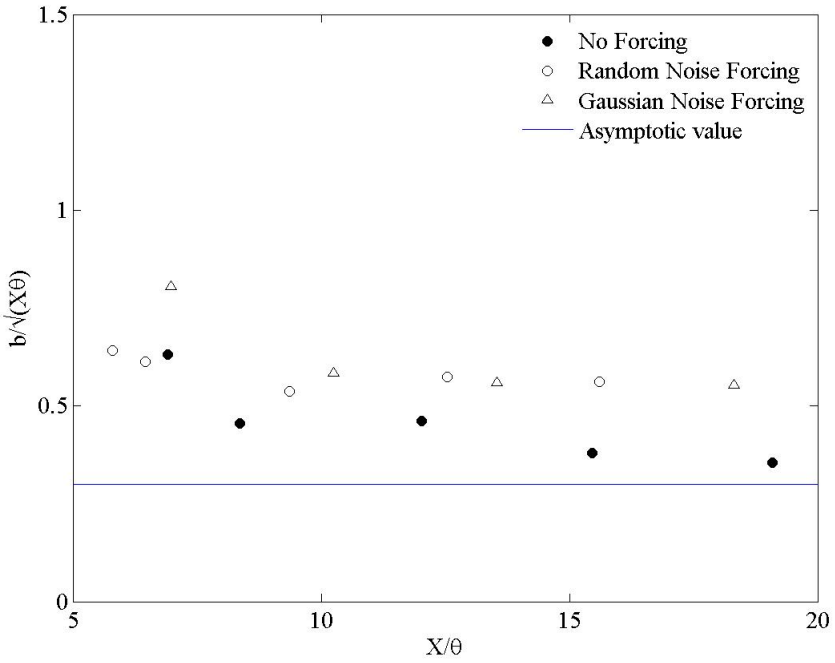


Figure 3.86: Half wake width parameter, cylinder with trip strip, single slit forcing, $\phi$ =95°

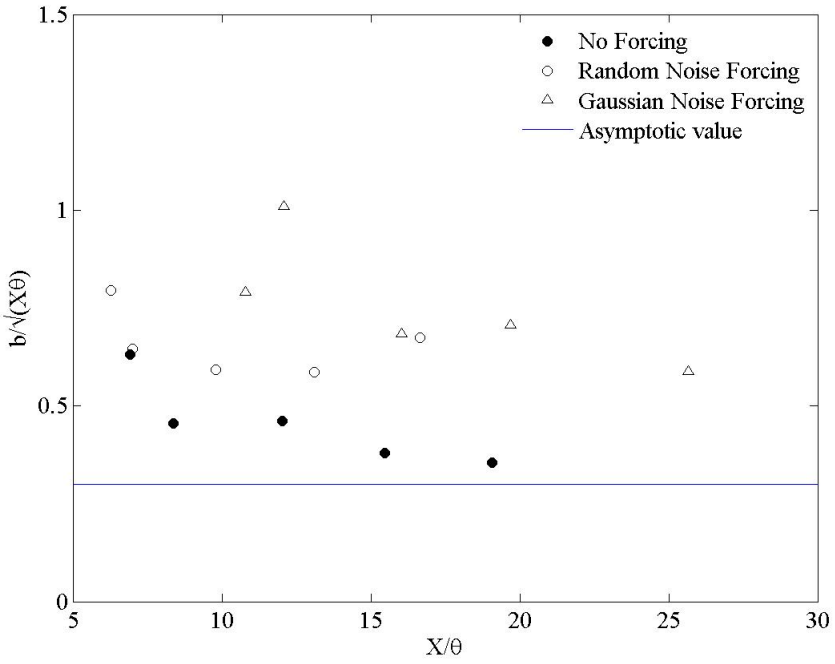


Figure 3.87: Half wake width parameter, cylinder with trip strip, single slit forcing, $\phi$ =100°

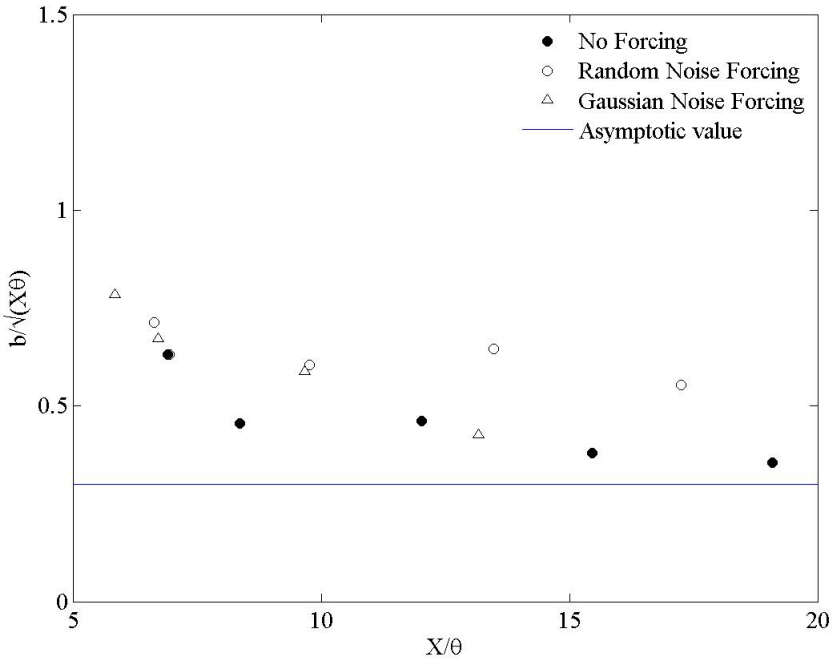


Figure 3.88: Half wake width parameter, cylinder with trip strip, single slit forcing, $\phi$ =105°

# Chapter 4

# Conclusion

The effects of random and Gaussian noise forcing were investigated on the wake of a circular cylinder at a Reynolds number of 12,000. Experiments involving noise forcing using two straight slits situated diametrically opposite on the cylinder surface, and single slit forcing at slit angle $\phi$ relative to the forward stagnation point were conducted in order to understand the mechanism that noise forcing had on the wake. It was shown that affecting one of the separating shear layers resulted in asymmetrical distribution of mean velocity, and global changes to the characteristics of the wake, causing subsequent reduction in drag. Noise forcing caused suppression of spectral peak associated with von Kármán vortex shedding. This promoted contraction of vortex formation region, thereby causing reduction in drag on the cylinder. Noise forcing at lower angles of $\phi$ caused breakdown of von Kármán vortices, which resulted in advection of smaller scale vortices in the shear layers. The magnitude of these smaller scale vortices were attenuated when $\phi$ was near the region of flow separation on the cylinder surface. Single slit noise forcing for a smooth cylinder from $\phi$=60° to $\phi$=90° shown random noise to be more efficient in suppressing Kármán vortex shedding compared to Gaussian noise. Maximum drag reduction by random noise forcing was 47% at $\phi$=90° , and by Gaussian noise forcing was 36% at $\phi$= 90° . The presence of turbulent strip at the forward stagnation point increased surface friction drag on the cylinder, adding energy to the boundary layer on the cylinder, delaying flow separation, reducing drag by 18%. Hybrid flow control using noise forcing with turbulent strip found Gaussian noise forcing more effective in suppression of vortex shedding, providing a maximum drag reduction of 28% at $\phi$=100° compared to random noise forcing, achieving a maximum drag reduction of 24% at $\phi$=100°

.

Bibliography


[1] M.M. Zdravkovich, *Flow Around Circular Cylinders*, Oxford University Press, 1997.

[2] Milton van Dyke, *An Album of Fluid Motion*, The Parabolic Press, 1982.

[3] J.H. Gerrard,"Vortex-Induced Vibrations", *Annual Review of Fluid Mechanics*, Vol.36, 2004, pp 413-455.

[4] E.Berger, R. Wille,"Periodic Flow Phenomena", *Annual Review of Fluid Mechanics*, Vol.4, 1972, pp 314-340.

[5] H. Oertel,"Wakes behind Blunt Bodies",*Annual Review of Fluid Mechanics*, Vol.22, 1990, pp 539-564.

[6] C.H.K. Williamson,"Vortex Dynamics in the Cylinder Wake", *Annual Review of Fluid Mechanics*, Vol.28, 1996, pp 447-539.

[7] A. Roshko,"On the Wake and Drag of Bluff Bodies",*Journal of Aeronautical Sciences*, Vol.22, 1955, pp 124-132.

[8] M.S. Bloor,"The Transition to Turbulence in the Wake of a Circular Cylinder",*Journal of Fluid Mechanics*, 1964, pp 290-303.

[9] J.C. Owen, P. Bearman,"Passive Control of VIV with Drag Reduction",*Journal of Fluid Mechanics*, Vol.15, 2001, pp 597-605.

[10] H. Nakamura, T. Igarashi,"Reductions in drag and fluctuating forces for a circular cylinder by attaching cylindrical rings", *Journal of Fluid Science and Technology*, Vol.2, No.1, 2007, pp. 12-22.

[11] Y.Z. Liu, L.L. Shi, J. Yu,"TR-PIV measurement of the wake behind a grooved cylinder at low Reynolds number",*Journal of Fluids and Structures*, 2011, pp 394-407.

[12] A. Ahmed, B. Bays-Muchmore, "Transverse Flow over a Wavy Cylinder", *Physics of Fluids A*, Vol.4, No.9, 1992, pp 1959-1967.

[13] A. Ahmed, M.J. Khan, B. Bays-Muchmore, "Experimental Investigation of Three Dimensional Bluff Body Wake", *AIAA Journal*, Vol.31, No.3, 1993, pp 559-563.

[14] C.H. Chang, *Volumetric PIV Measurement in the Wake of Wavy Cylinder*, Masters Thesis, Auburn University, 2014.

[15] P.W. Bearman, "Vortex Shedding from Oscillating Bluff Bodies", *Annual Review of Fluid Mechanics*, 1984, pp 195-222.

[16] E.A. Anderson, A.A. Szewczyk, "Effects of a splitter plate on the near wake of a circular cylinder in 2 and 3-dimensional flow configurations", *Experiments in Fluids*, 1997, pp 161-174.

[17] N.K. Randeria, *Flows with Nodal and Saddle Attachment and Separation*, Masters Thesis, Texas A & M University, 1994.

[18] K. Kwon, H. Choi, "Control of Laminar Vortex Shedding behind a Circular Cylinder using Splitter Plates", *Physics of Fluids*, Vol.8, No.2, 1996, pp 479-486.

[19] S. Ozono, "Flow Control of vortex shedding by a short splitter plate asymmetrically arranged downstream of a cylinders", *Physics of Fluids*, Vol.11, No.10, 1999, pp 2928-2934.

[20] J.Y. Hwang, K.S. Yang, S.H. Sun, "Reduction of flow-induced forces on a circular cylinder using a detached splitter plate", *Physics of Fluids*, Vol.15, No.8, 2003, pp 2433-2436.

[21] A. Ekmecki, D. Rockwell, "Effects of a geometrical surface disturbance on flow past a circular cylinder: a large- scale spanwise wire", *Journal of Fluid Mechanics*, Vol.665, 2010, pp 129-157.

[22] H. Y. Wong and A. Kokkalis, "A comparative study of three dimensional devices for suppressing vortex-induced oscillation", *Journal of Wind Engineering and Industrial Aerodynamics*, Vol.10, 1982, pp 21-29.

[23] C. Scruton and D.E. Walshe, "A means of avoiding wind-excited oscillations of structures with a circular or nearly circular cross-section", National Physics Laboratory, Technical report 335, Middlesex, England, 1957.

[24] L. Woodgate and J.F.M. Mabey, "Further experiments on the use of helical strakes for avoiding wind-excited oscillations of sturctures of circular or nearly circular section", Technical report 351, 1959.

[25] M.J. Every, R. King, D.S. Weaver, "Vortex-induce vibrations of cylinders and cables and their suppression", *Ocean Engineering*, Vol.9, 1982, pp 135-157.

[26] J. Yoon, *Control of flow over a circular cylinder using a wake disrupter*, Master's Thesis, Seoul National University, Korea, 2005.

[27] P.T. Tokumaru, P.E. Domitakis, "Rotary oscillation control of a cylinder wake", *Journal of Fluid Mechanics*, Vol.224, 1991, pp 77-90.

[28] G.H. Koopman, "The vortex wakes of vibrating cylinders at low Reynolds numbers", *Journal of Fluid Mechanics*, Vol.28, 1967, pp 501-512.

[29] C.J. Wood, "The effect of base bleed on a periodic wake", *Journal of the Royal Aeronautics Society*, Vol.68, 1964, pp 477-482.

[30] P.W. Bearman, "The effect of base bleed on the flow behind a two-dimensional model with a blunt trailing edge", *Aeronautical Quarterly*, Vol.18, 1967, pp 207-224.

[31] J.H.M. Fransson, P. Konieczny, P.H. Alfreddson, "Flow around porous cylinder subject to continuous suction or blowing", *Journal of Fluids and Structures*, Vol.19, 2004, pp 1031-1048.

[32] W. Chen, H. Hu, H. Li, "Suppression of Vortex shedding from a circular cylinder by using suction flow control method", No. 2013-0103, 51st AIAA Aerospace Sciences Meeting, 2013.

[33] E. Detemple-Laake, H. Ecklemann, "Phenomenology of Kármán vortex streets in oscillatory flow", *Experiments in Fluids*, Vol.7, 1997, pp 217-227.

[34] R.D. Blevins, "The effect of sound on vortex shedding from cylinders", *Journal of Fluid Mechanics*, Vol.161, 1985, pp 217-237.

[35] F.B. Hsiao and J.Y. Shyu, "Influence of Internal Acoustic Excitation upon Flow Passing a Circular Cylinder", *Journal of Fluids and Structures*, Vol.5, 1991, pp 427-442.

[36] X.Y. Huang, "Suppression of vortex shedding from a circular cylinder by internal acoustic excitation", *Journal of Fluids and Structures*, Vol.9, 1995, pp 563-570.

[37] N. Fujisawa and G. Takeda, "Flow control around a circular cylinder by internal acoustic excitation", *Journal of Fluids and Structures*, Vol.19, 2004, pp 1031-1048.

[38] E.P. DeMauro, C.M. Leong, M. Amitay, "Modification of the near wake behind a finite-span cylinder by a single synthetic jet", *Experiments in Fluids*, Vol.53, 2012, pp 1963-1978.

[39] S. Bhattacharya, *Effect of three dimensional forcing on the wake of a circular cylinder*, Masters' Thesis, Auburn University, 2009.

[40] M.H. Moore, *Effect of in phase and out of phase forcing on circular cylinder wake*, Masters' thesis, Auburn University, 2012.

[41] H. Tyagi, R. Liu, David S-K. Ting, *Measurement of Wake Properties of a Sphere in Freestream Turbulence*, Masters' thesis, University of Calgary, Alberta, Canada, 2006.

[42] A. Glezer, "Some aspects of aerodynamic flow control using synthetic-jet actuation", *Philosophical Transactions of The Royal Society*, Vol.369, 2011, pp 1476-1494.

[43] L.H. Feng, J.J. Wang, "Circular cylinder vortex-synchronization control with a synthetic jet positioned at the rear stagnation point", *Journal of Fluid Mechanics*, Vol.662, 2010, pp 232-259.

[44] A. Naim, D. Greenblatt, A. Seifert, I. Wygnanski, "Active Control of a Circular Cylinder Flow at Transitional Reynolds Numbers", *Journal of Flow Turbulence and Combustion*, Vol.78, 2007, pp 383-407.

[45] R. Chevray, L.S.G. Kovasznay, "Turbulence Measurements in the Wake of a Thin Flat Plate", *AIAA Journal*, vol.7, 1969, pp 1641-1643.

[46] K.R. Sreenivasan,"Approach to Self-Preservation in Plane Turbulent Wakes", *AIAA Journal*, No. 81-4276, 1980.

[47] B.R. Ramaprian, V.C. Patel, M.S. Sastry, "The symmetric Turbulent Wake of a Flat Plate", *AIAA Journal*, vol.20, 1982, pp 1228-1235.

[48] F.E. Jorgensen, *How to Measure Turbulence with Hot-wire Anemometry: A Practical Guide*, Dantec Dynamics, 2005.

Appendices

Appendix A

Additional Results

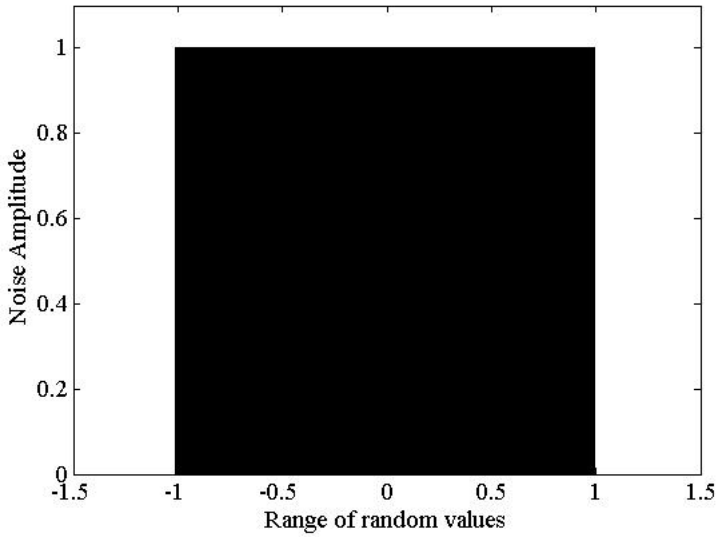


Figure A.1: PDF of Random Noise signal

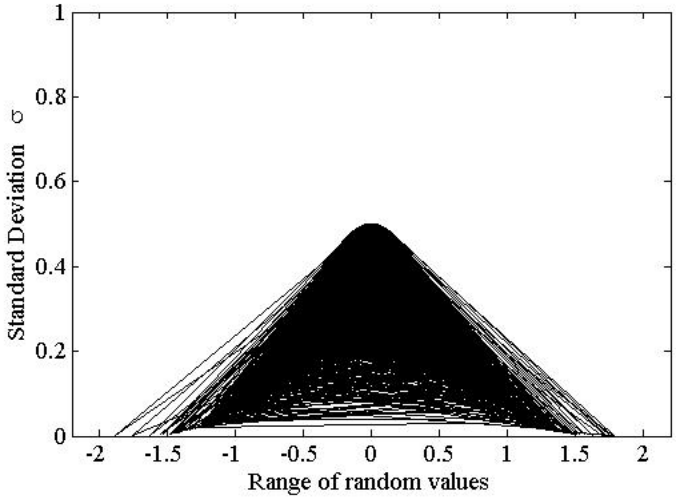


Figure A.2: PDF of Gaussian Noise signal

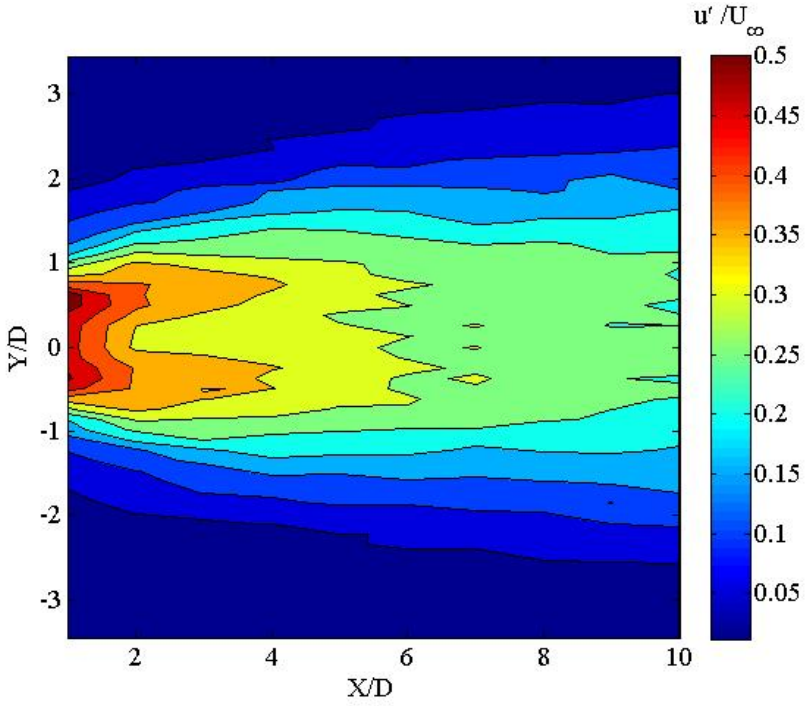


Figure A.3: Turbulence intensity contours, smooth cylinder, no forcing

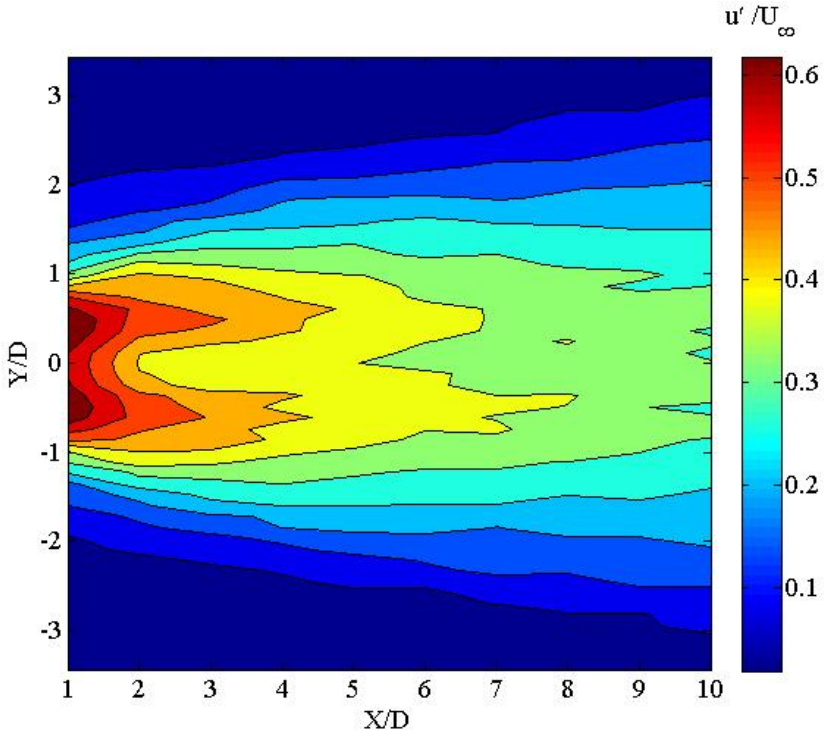


Figure A.4: Turbulence intensity contours, tripped cylinder, no forcing

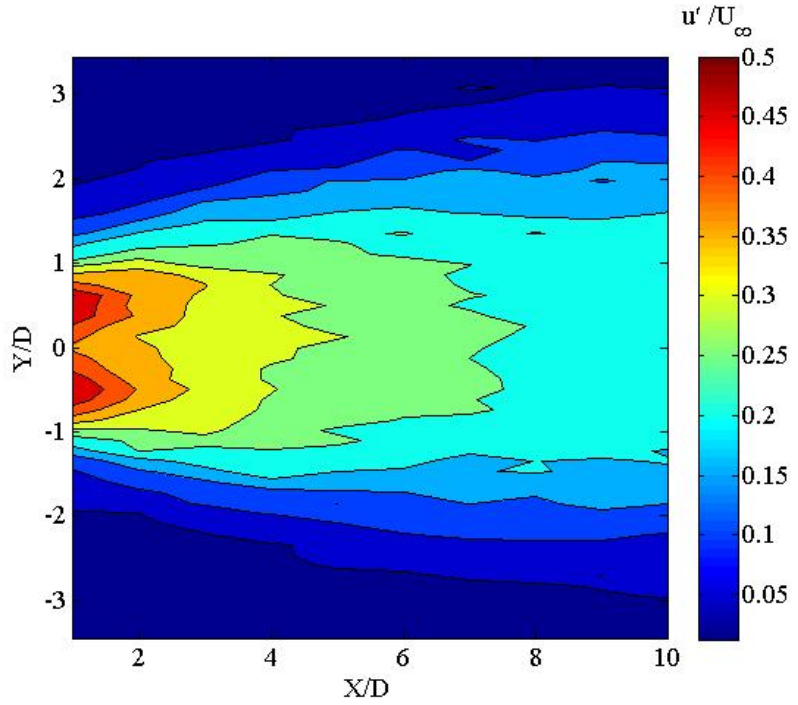


Figure A.5: Turbulence intensity contours, smooth cylinder, two slit forcing, random noise

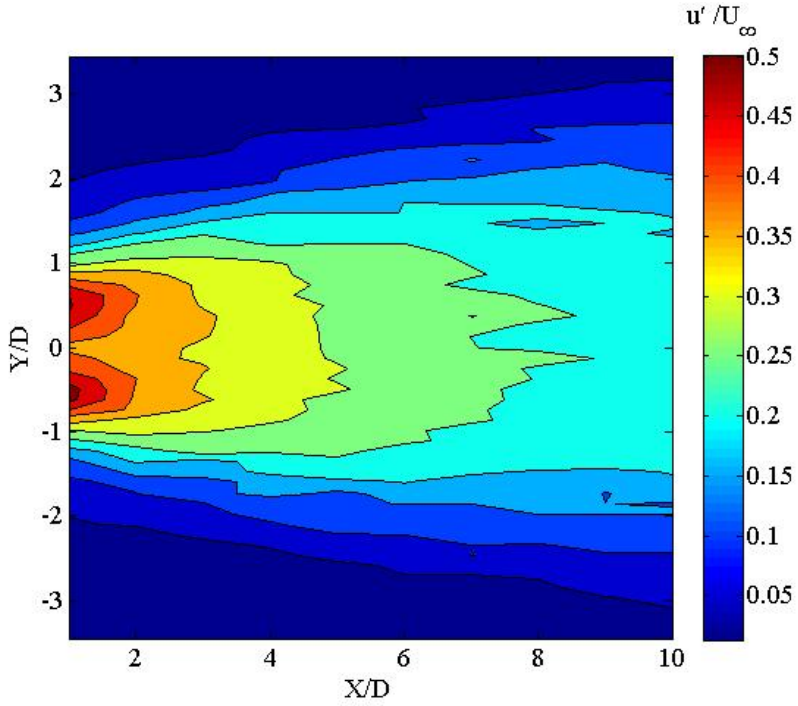


Figure A.6: Turbulence intensity contours, smooth cylinder, two slit forcing, Gaussian noise

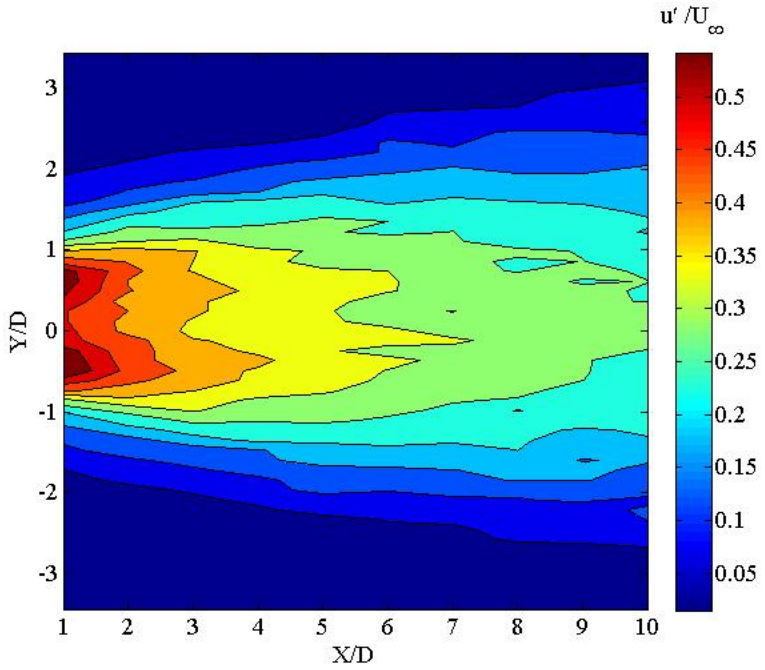


Figure A.7: Turbulence intensity contours, smooth cylinder, single slit forcing, random noise, $\phi$ =60°

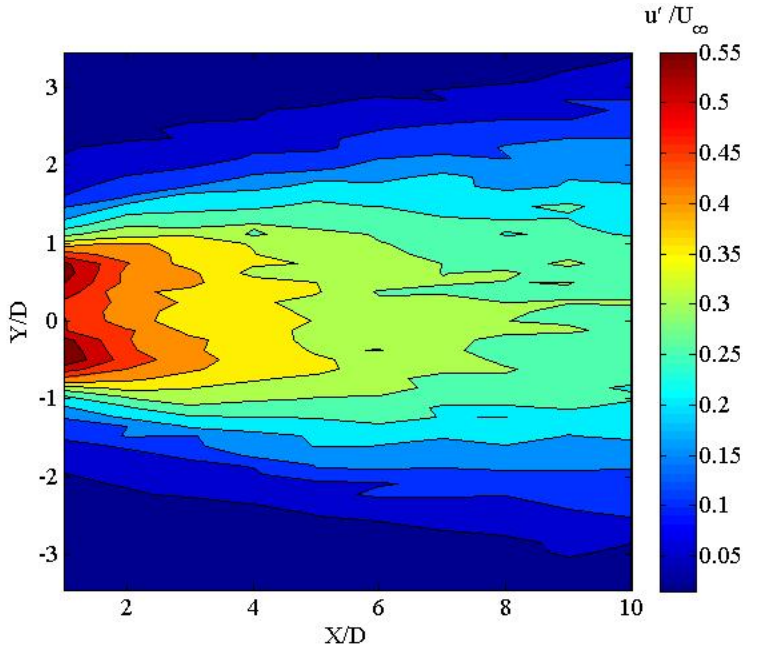


Figure A.8: Turbulence intensity contours, smooth cylinder, single slit forcing, Gaussian noise, $\phi$ =60°

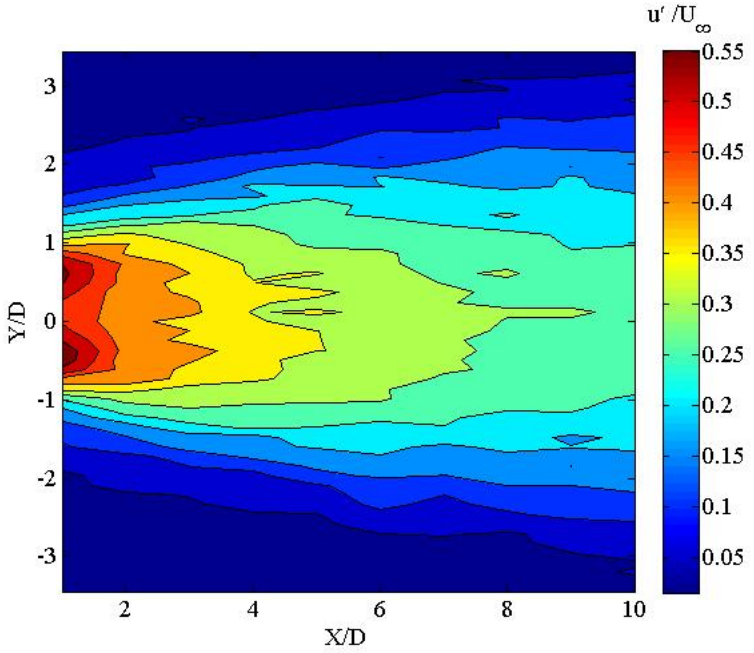


Figure A.9: Turbulence intensity contours, smooth cylinder, single slit forcing, random noise, $\phi$ =65°

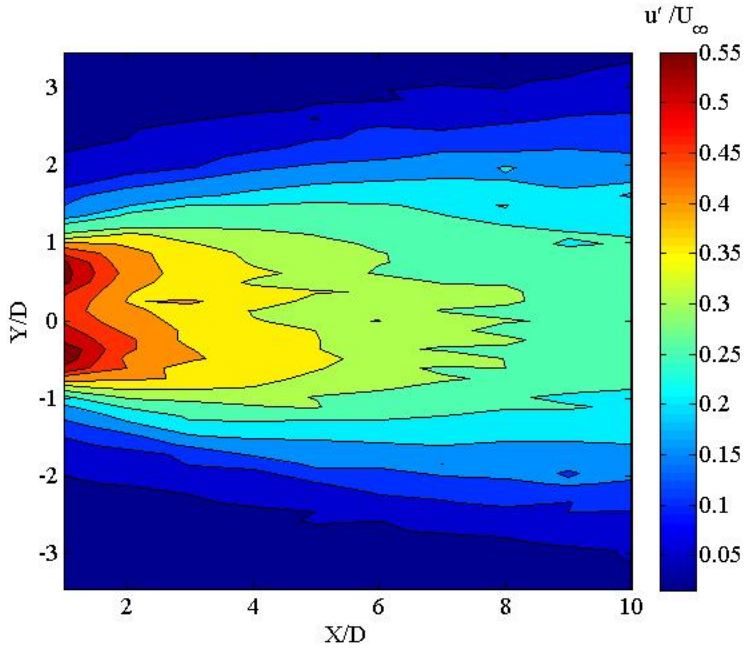


Figure A.10: Turbulence intensity contours, smooth cylinder, single slit forcing, Gaussian noise, $\phi$ =65°

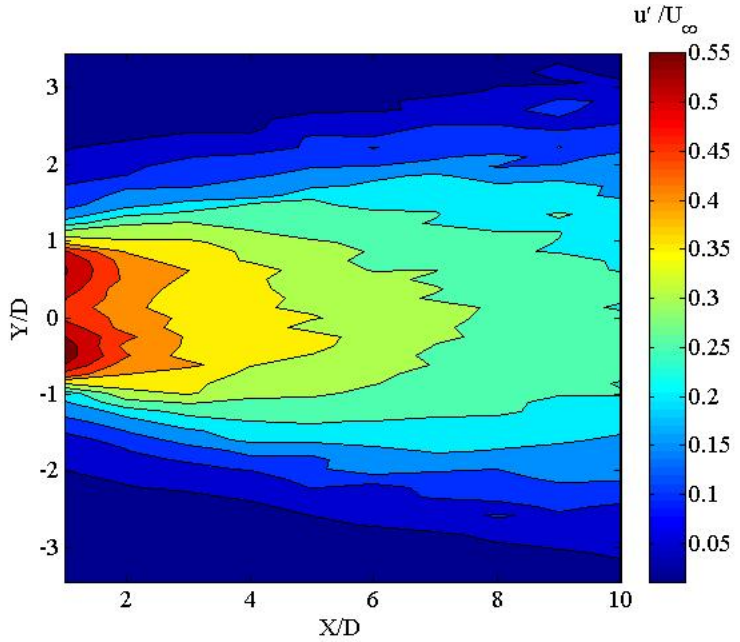


Figure A.11: Turbulence intensity contours, smooth cylinder, single slit forcing, random noise, $\phi$ =70°

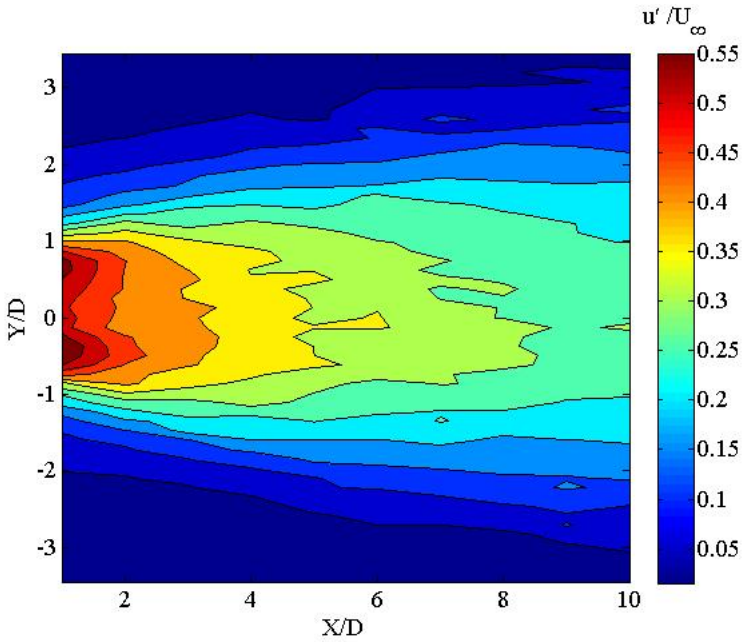


Figure A.12: Turbulence intensity contours, smooth cylinder, single slit forcing, Gausssian noise, $\phi$ =70°

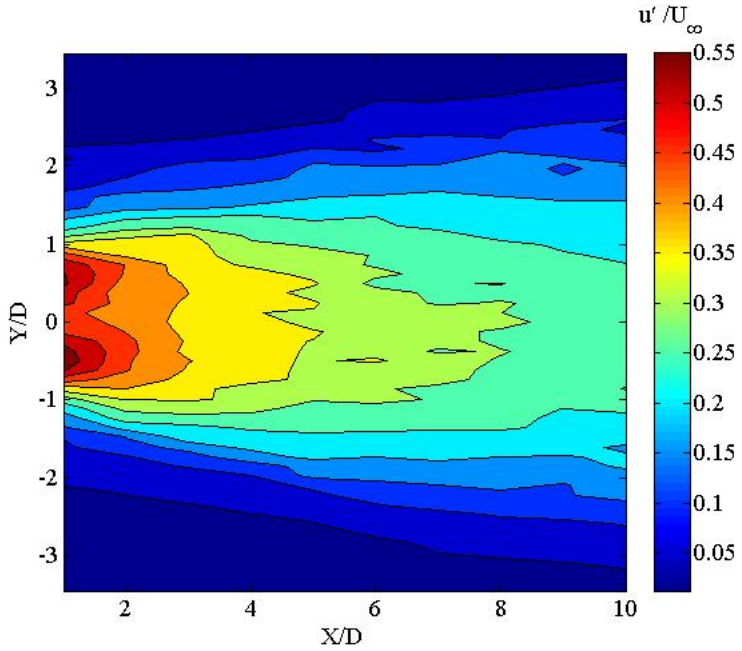


Figure A.13: Turbulence intensity contours, smooth cylinder, single slit forcing, random noise, $\phi$ =75°

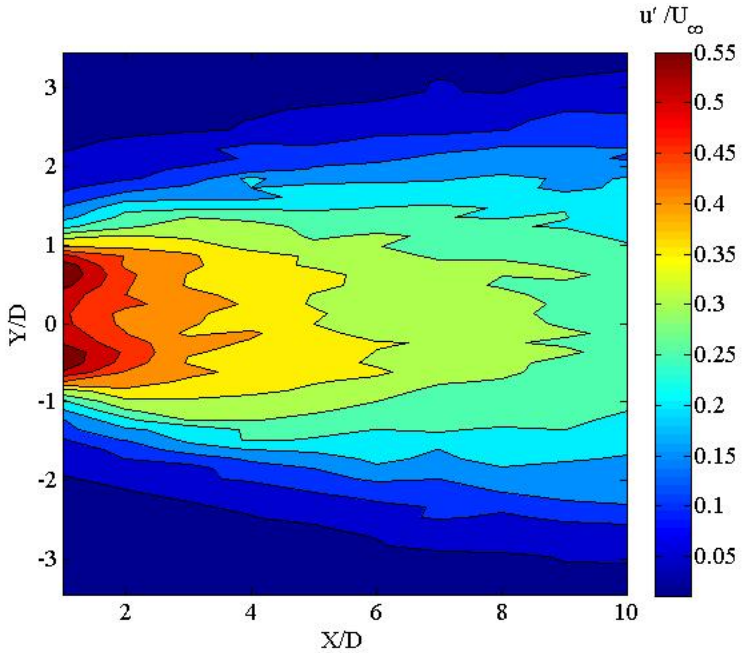


Figure A.14: Turbulence intensity contours, smooth cylinder, single slit forcing, Gaussian noise, $\phi$ =75°

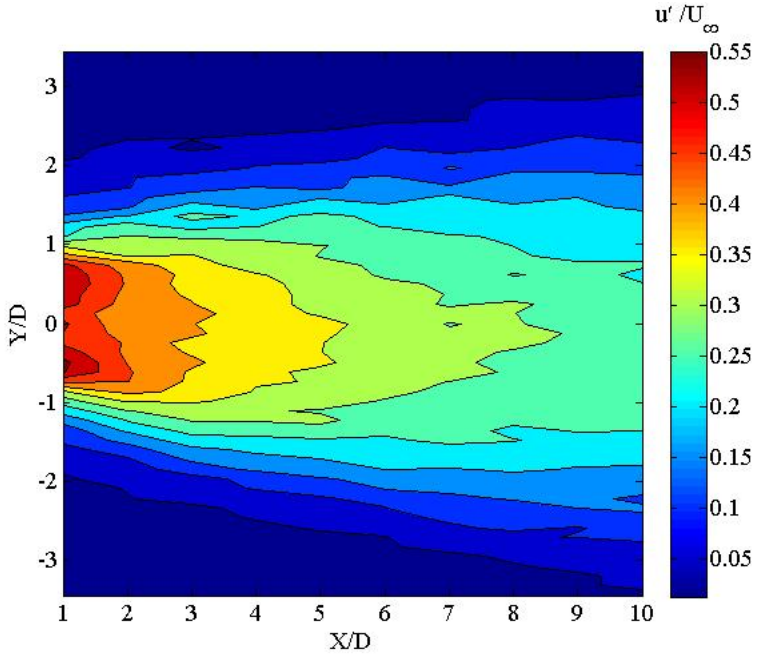


Figure A.15: Turbulence intensity contours, smooth cylinder, single slit forcing, random noise, $\phi$ =80°

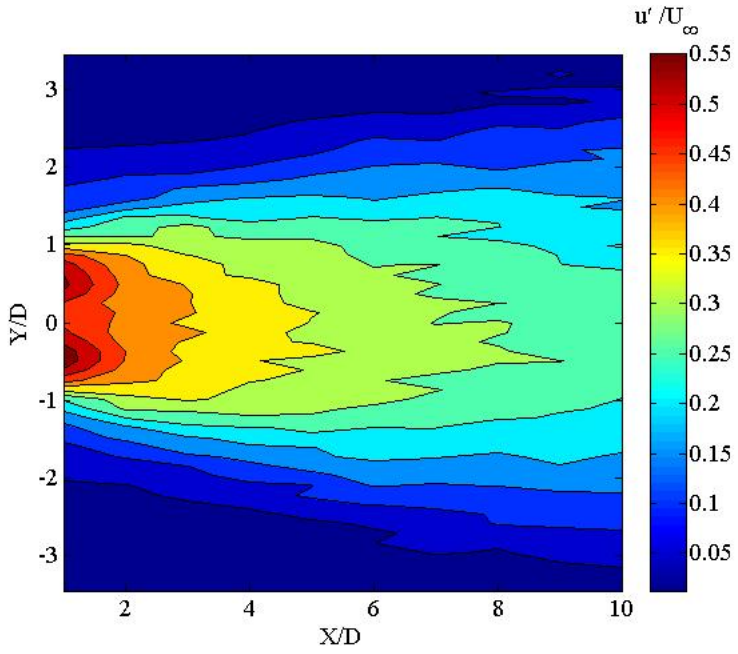


Figure A.16: Turbulence intensity contours, smooth cylinder, single slit forcing, Gaussian noise, $\phi$ =80°

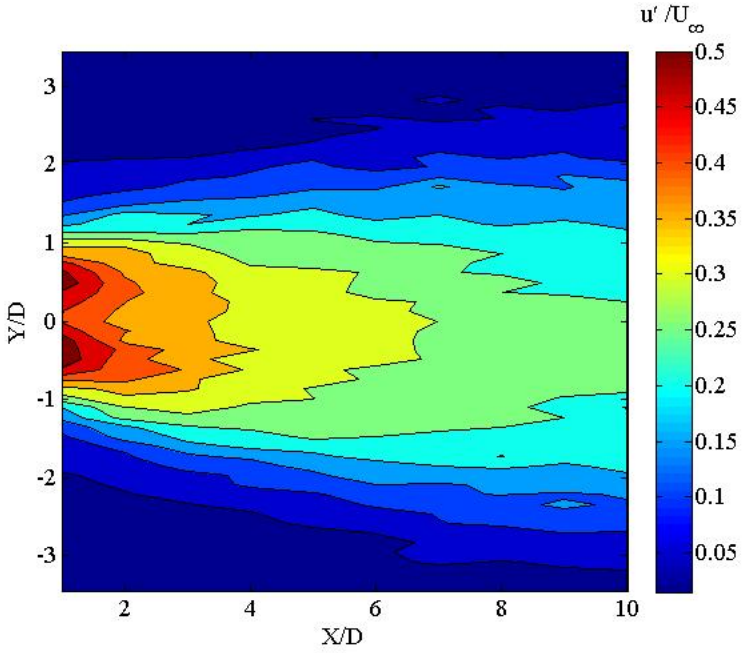


Figure A.17: Turbulence intensity contours, smooth cylinder, single slit forcing, random noise, $\phi$ =85°

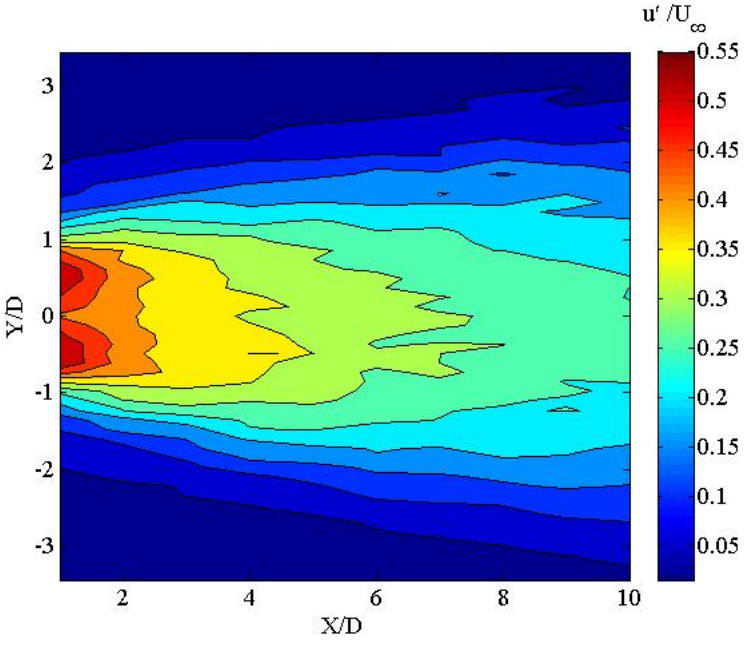


Figure A.18: Turbulence intensity contours, smooth cylinder, single slit forcing, Gaussian noise, $\phi$ =85°

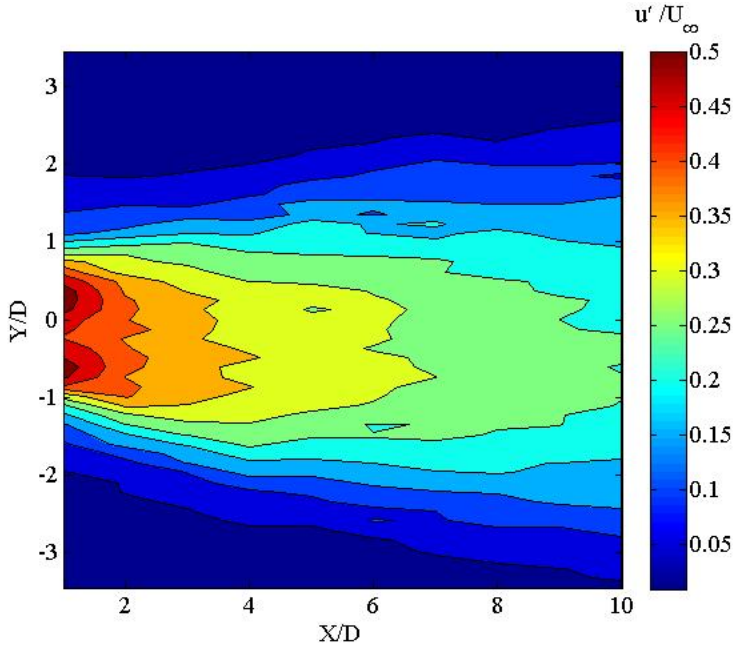


Figure A.19: Turbulence intensity contours, smooth cylinder, single slit forcing, random noise, $\phi$ =90°

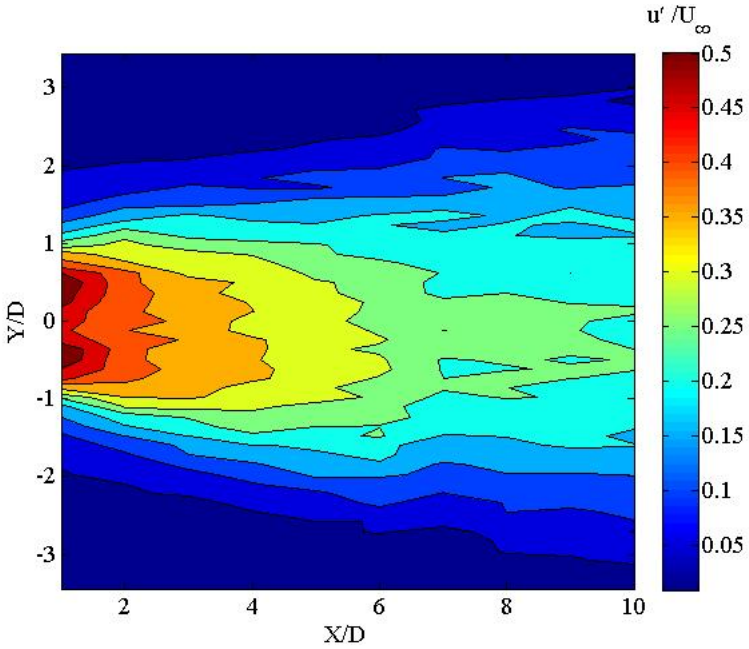


Figure A.20: Turbulence intensity contours, smooth cylinder, single slit forcing, Gaussian noise, $\phi$ =90°

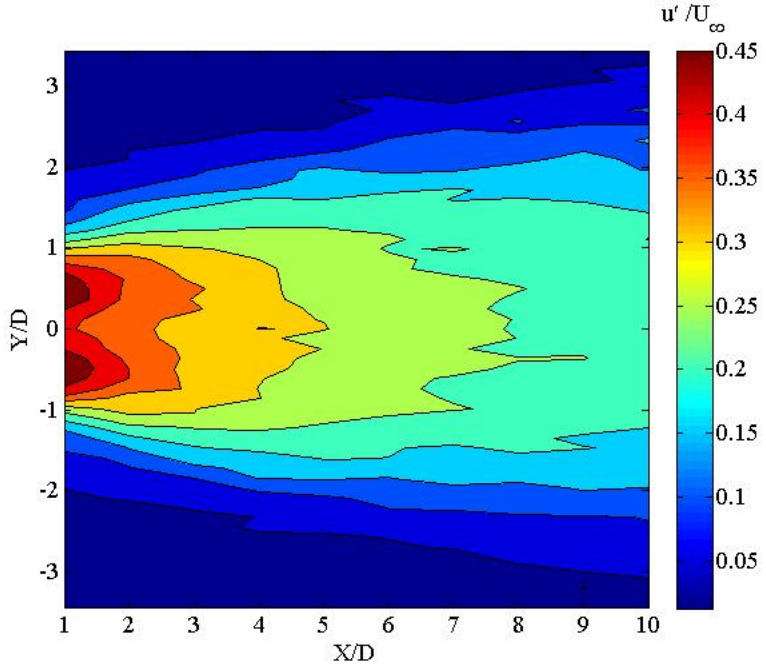


Figure A.21: Turbulence intensity contours, tripped cylinder, two slit forcing, random noise

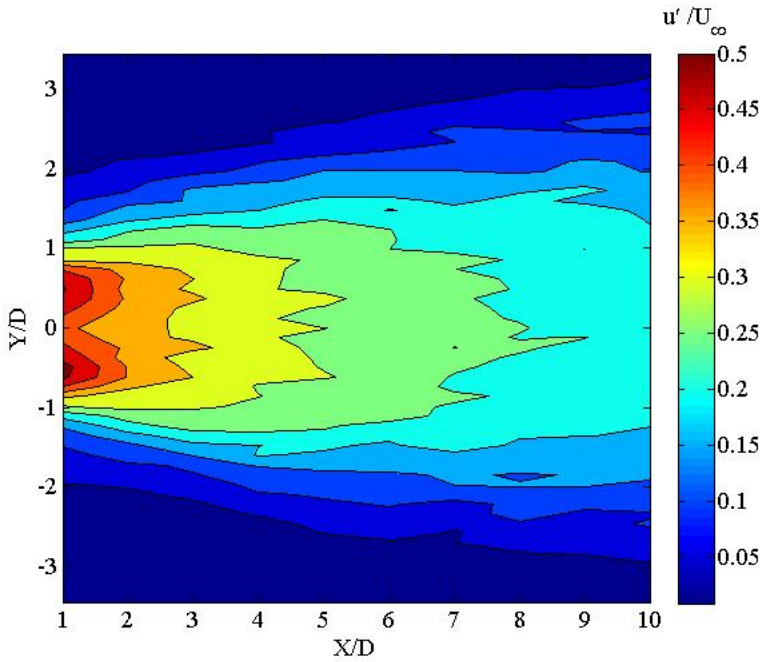


Figure A.22: Turbulence intensity contours, tripped cylinder, two slit forcing, Gaussian noise

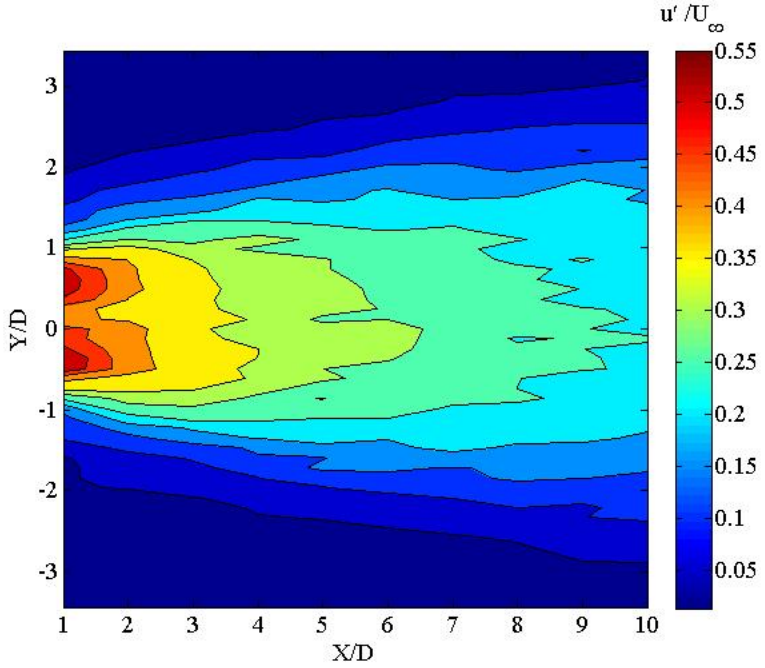


Figure A.23: Turbulence intensity contours, tripped cylinder, single slit forcing, random noise, $\phi$ =90°

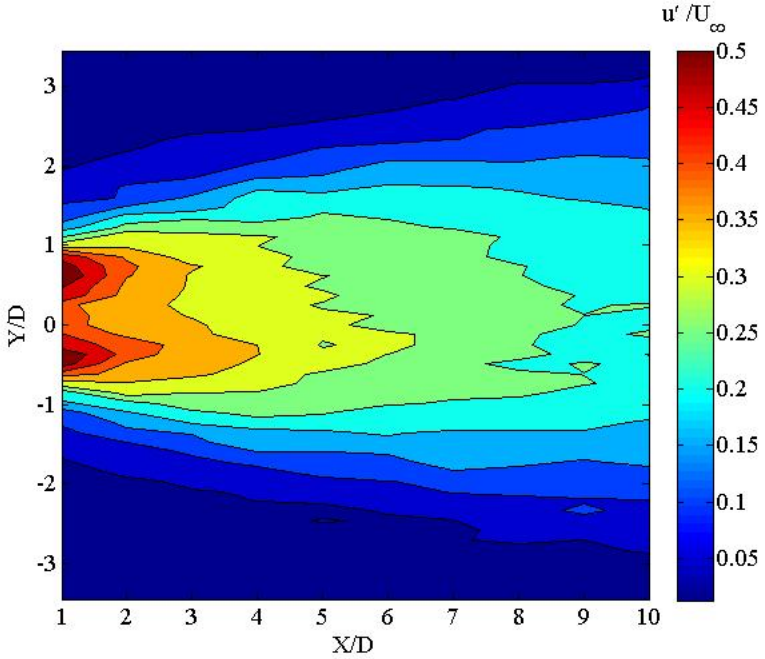


Figure A.24: Turbulence intensity contours, tripped cylinder, single slit forcing, Gaussian noise, $\phi$ =90°

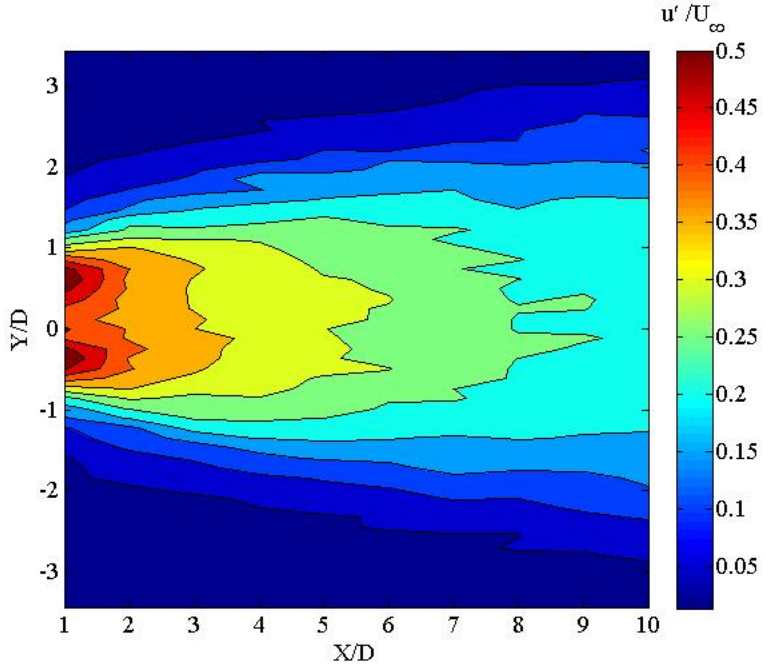


Figure A.25: Turbulence intensity contours, tripped cylinder, single slit forcing, random noise, $\phi$ =95°

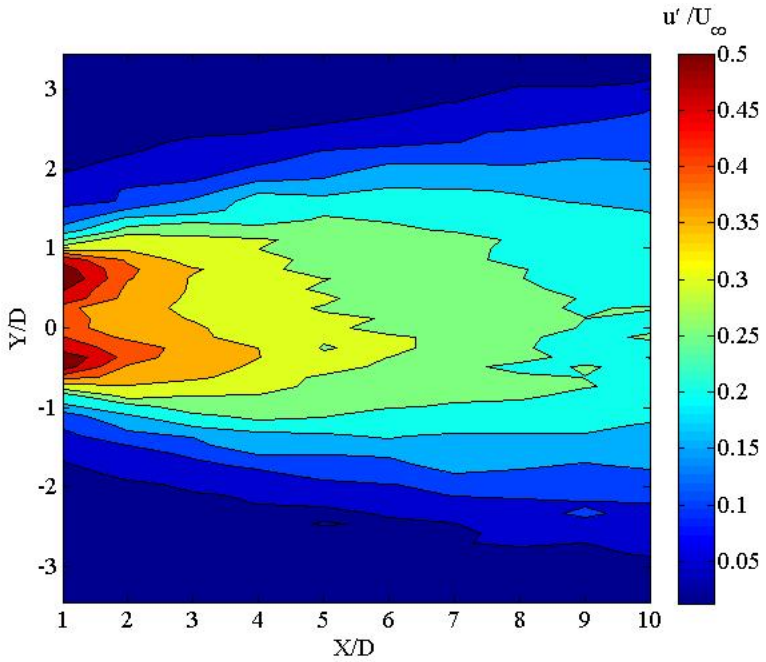


Figure A.26: Turbulence intensity contours, tripped cylinder, single slit forcing, Gaussian noise, $\phi$ =90°

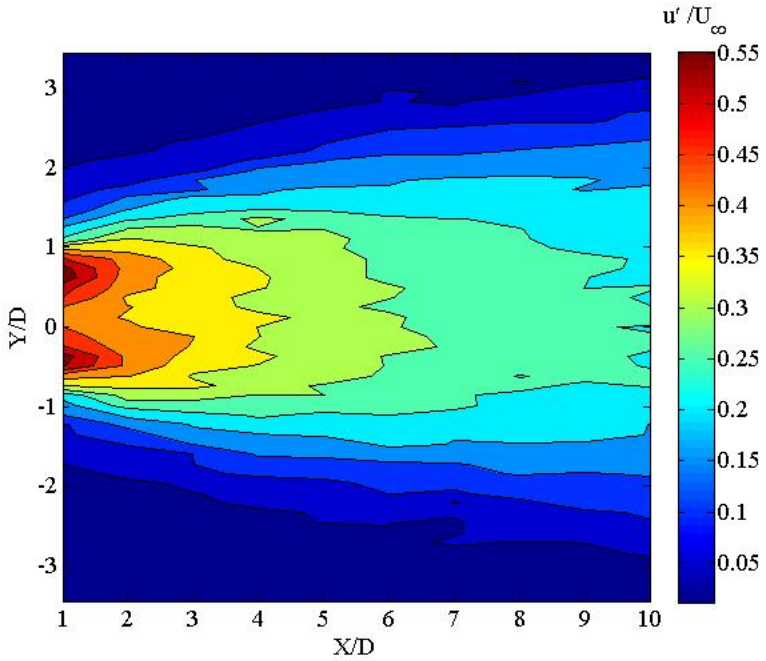


Figure A.27: Turbulence intensity contours, tripped cylinder, single slit forcing, random noise, $\phi$ =100°

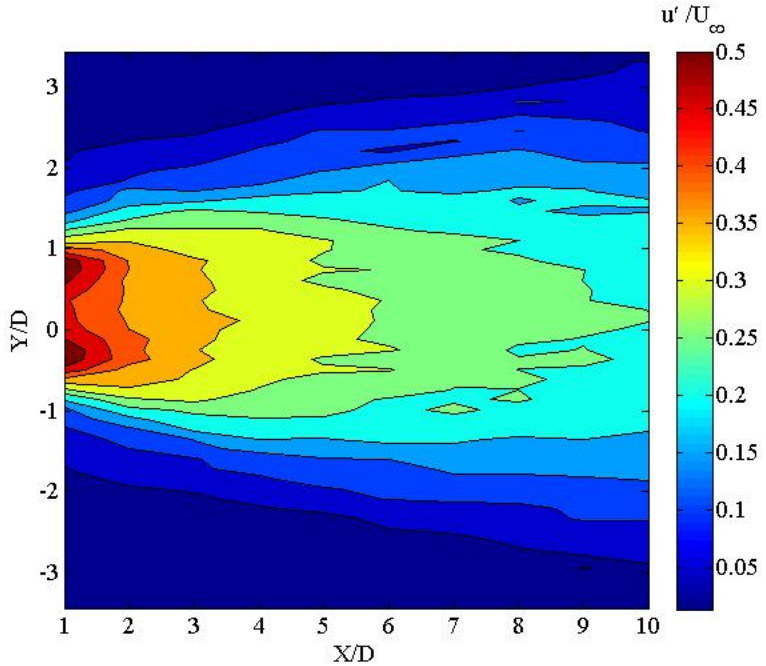


Figure A.28: Turbulence intensity contours, tripped cylinder, single slit forcing, Gaussian noise, $\phi$ =100°

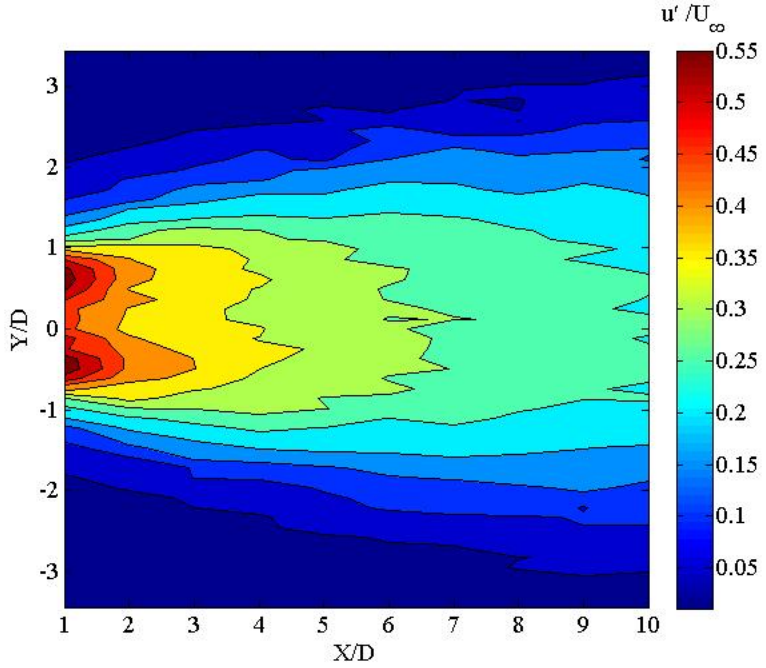


Figure A.29: Turbulence intensity contours, tripped cylinder, single slit forcing, random noise, $\phi$ =105°

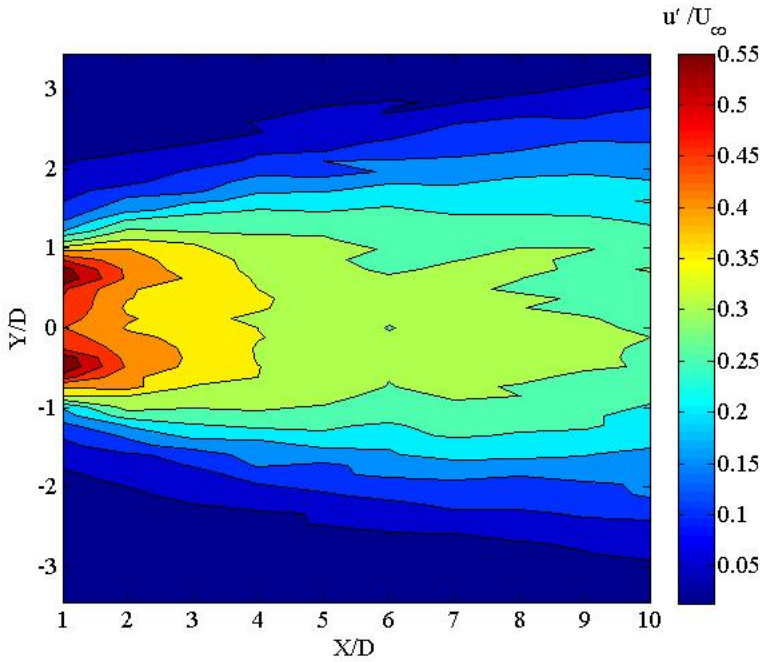


Figure A.30: Turbulence intensity contours, tripped cylinder, single slit forcing, Gaussian noise, $\phi$ =105°

# Appendix B

## Calibration of Equipment and Sensors

The contents of this appendix describes the calibration procedure for the hot wire anemometer and the pressure transducer, which were carried out before conducting each experiment.

### B.1 Calibration of Pressure Transducer

The Validyne DP45 -16 pressure transducer was calibrated against a predetermined pressure from a micro manometer. Water was the fluid used in the manometer. A hand - held piston was used to apply a known amount of pressure. The micro manometer was based on the same working principle as that of a regular manometer, although replacing the indication system with a micrometer and using conduction. As the micrometer needle touches the surface of water column, a micro-ammeter reads the contact by showing deflection of the needle in the dial, which was made feasible by conduction of electricity. The following steps were performed to calibrate the pressure transducer.

1. The Validyne CD - 12 carrier demodulator, which was always connected to the pressure transducer, was switched on.

2. The port marked with a + sign was connected using flexible pressure tubing.

3. A T - pipe joint was used to connect the transducer to the piston and manometer in parallel. Before starting calibration, the water level in the manometer was checked to ensure it was equal in both arms. Also, the position of the piston was to be fully open before beginning calibration.

4. Micrometer needle height was adjusted by 0.1 inches.

5. The hand - held piston was slowly operated until the water column touched the micrometer needle, and the micro - ammeter indicated a deflection.

6. The reading on the digital display of the carrier demodulator was noted down along with the height of water column.

7. Steps 4 through 6 were repeated for every 0.1 inches, upto a water column height of 1 inch.

8. The data was plotted and a straight line fitted to the data. This equation described the transfer function used to convert voltage readouts from the pressure transducer to dynamic pressure in terms of water column height. Table B.1 shows a calibration chart from a typical calibration procedure.

Table B.1: Calibration Chart for Pressure Transducer

| V (volts) | Height (Inches of water) |
|---|---|
| 0.07 | 0 |
| 0.47 | 0.1 |
| 0.875 | 0.2 |
| 1.3 | 0.3 |
| 1.69 | 0.4 |
| 2.105 | 0.5 |
| 2.515 | 0.6 |
| 2.91 | 0.7 |
| 3.315 | 0.8 |
| 3.715 | 0.9 |
| 4.07 | 1.0 |

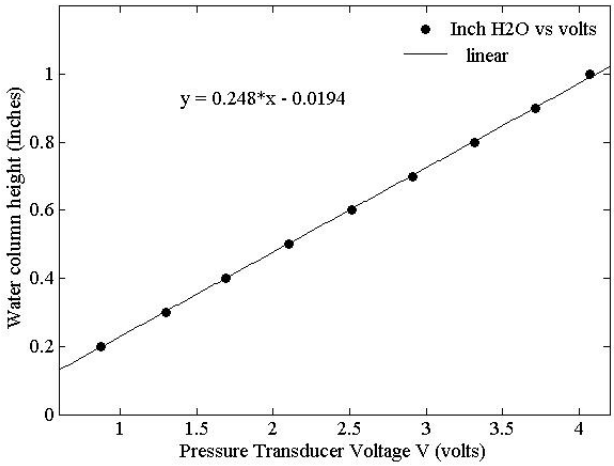


Figure B.1: Calibration curve for Pressure Transducer

## B.2 Calibration of Hot Wire

A single probe Dantec Dynamics Hot Wire probe was used for capturing spectral information and turbulent quantities of the wake. In-situ calibration was performed in order to obtain the calibration curve and transfer function to convert voltage into velocity. The probe was positioned in center of the wind tunnel test section ensuring that there is no influence of the near-wall effects of the wind tunnel. An oscilloscope was used to monitor any fluctuations observed in free stream velocity, and a Spectrum Analyzer to ensure that the sensor probe was not under the influence of extraneous turbulence. Calibration of the hot wire probe in the wind tunnel provided a proper indication of the free stream turbulence in the wind tunnel. The wind tunnel was operated in increasing steps of velocity starting with a minimum velocity until a maximum of 67 ft/s, corresponding to 1 inch of water column pressure. The values of CTA voltage were tabulated using the Dantec MiniCTA software and plotted using MATLAB. A fourth - order polynomial curve fit was then incorporated to obtain the transfer function from which velocities may be obtained as a function of CTA voltage, shown by Table B.2.

Table B.2: Calibration chart for Hot Wire

| CTA Voltage E (volts) | Velocity ($ft/s$) |
|---|---|
| 1.628 | 2.111 |
| 1.64 | 4.221 |
| 1.648 | 5.170 |
| 1.657 | 5.969 |
| 1.665 | 6.674 |
| 1.672 | 7.897 |
| 1.682 | 8.442 |
| 1.685 | 8.954 |
| 1.694 | 9.438 |
| 1.716 | 11.560 |
| 1.733 | 13.348 |
| 1.75 | 14.924 |
| 1.765 | 16.348 |
| 1.778 | 17.658 |
| 1.79 | 18.877 |
| 1.802 | 20.022 |
| 1.811 | 21.105 |
| 1.822 | 22.135 |
| 1.829 | 23.119 |
| 1.839 | 24.063 |
| 1.846 | 24.972 |
| 1.854 | 25.848 |
| 1.862 | 26.696 |
| 1.868 | 27.518 |
| 1.875 | 28.315 |
| 1.881 | 29.091 |
| 1.889 | 29.847 |
| 1.938 | 36.555 |
| 1.975 | 42.210 |
| 2.006 | 47.192 |
| 2.031 | 51.697 |
| 2.054 | 55.839 |
| 2.073 | 59.694 |
| 2.091 | 63.315 |
| 2.107 | 66.740 |

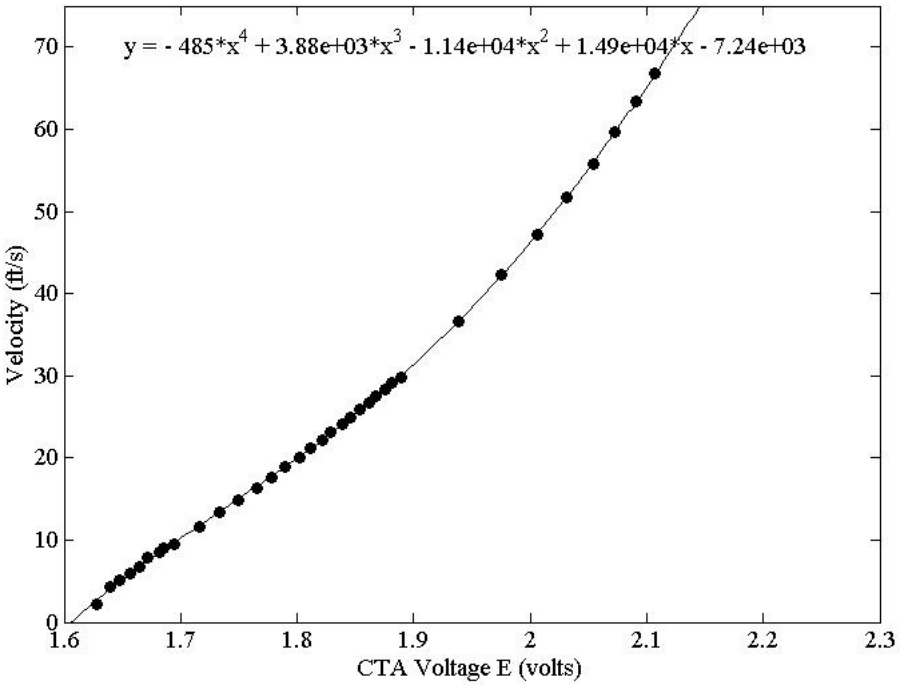


Figure B.2: Calibration curve for Hot Wire

# Appendix C

## Uncertainty Analysis

Quantification of experimental uncertainties involved with pressure transducer and hot wire data were carried out in accordance with the procedure and formulae suggested by Jorgensen [48]. The reference case selected for evaluation of uncertainty was that of Reynolds number 12,000, corresponding to 15 ft/s or 4.4 m/s. Uncertainties involved in the calculation of mean velocity profiles was considered for this exercise. The following sources for error were considered for uncertainty calculation. Errors caused due to temperature and pressure variation were ignored.

Error from pressure transducer was determined from the data sheet provided by the manufacturer. The error was found to be 0.5% of the full scale input, giving a relative standard uncertainty of 0.01.

The error caused from pressure transducer was related to curve fitting errors. A straight line was fitted to the data provided in Table B.1. Residuals at each data point were found by using the Curve Fitting Toolbox in MATLAB. The residuals denote the error present in each data point. The relative standard uncertainty was calculated using the formula

$$relative\ standard\ uncertainty = 2 * \frac{1}{100}\ standard\ deviation\ (error, \%)$$

The standard deviation from pressure transducer calibration was found out to be 0.05%, giving a relative standard uncertainty of 0.001.

Error was also associated with hot wire calibration. A fourth order polynomial was fitted to the data which was provided in Table B.2. Calculation of relative standard uncertainty for the residuals acquired at each data point were measured in the same manner as with

pressure transducer error. The standard deviation of hot wire calibration was found to be 0.98%, giving a relative standard uncertainty of 0.019.

The A/D board was also considered as a source for error. The calculation of relative standard uncertainty for A/D board resolution was by using the formula

$$relative\ standard\ uncertainty\ = \frac{1}{\sqrt{3}}\ \frac{1}{U}\ \frac{E_{AD}}{2^n}\ \frac{\partial U}{\partial E}$$

where $E_{AD}$ is the A/D board input range, $n$ is the board resolution in bits, $U$ is the velocity and $\frac{\partial U}{\partial E}$ is the sensitivity factor (slope) of the hot wire calibration curve. For the A/D board used in these experiments (NI - PCI 6035E), $E_{AD} = 20\ V$, $n = 16$, $U = 15$ ft/s, $\frac{\partial U}{\partial E} = 127.81$. This gives a relative standard uncertainty of 0.0015.

Table C.1: Uncertainities of a single velocity sample acquired by hot wire for calculation of mean velocity profile

| *Error source* | *Value* | *Coverage factor(k)* | *Relative Standard Uncertainty* |
|---|---|---|---|
| Calibrator | 0.02 | 2 | 0.01 |
| Pressure Transducer Calibration | 0.001 | 2 | 0.0005 |
| Hot Wire Calibration | 0.019 | 2 | 0.00095 |
| A/D board resolution | 0.0015 | $\sqrt{3}$ | 0.000867 |

The total uncertainty involved in the calculation of velocitiy sample is calculated from the expression $2\sqrt{0.01^2\ +\ 0.0005^2\ +\ 0.00095^2\ +\ 0.000867^2}\ =\ 0.0202\ =\ 2.02\%$ .